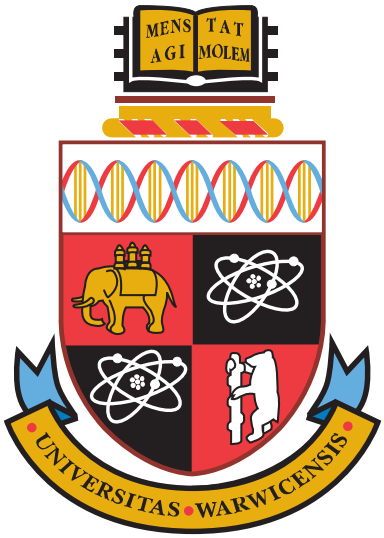

Turbulence and Scaling Phenomena in Solar System Plasmas

by

Ruth Mary Nicol

Thesis

Submitted to the University of Warwick

for the degree of

Doctor of Philosophy

Department of Physics

September 2009

THE UNIVERSITY OF WARWICK

Contents

List of Tables

List of Figures

Acknowledgments

I would like to thank my supervisors, Professor Sandra Chapman and Professor Richard Dendy, for their help and guidance throughout my PhD. I would also like to aknowledge all my colleagues in the CFSA and in particular Khurom for many helpful discussions and support when I was tearing my hair out at Matlab. Many thanks also to my friends, Stephanie, Lieke, Jon - you always had shoulders to cry and/or chocolate! In particular Stephanie, who has been my long-suffering housemate for the past five years. Thanks also to my family, in particular my mother and my sisters, Lucy and Katy, who have always been there at the end of a phone when I needed them.

I wish to thank the ACE and Ulysses data teams for data provision and finally both the STFC and UKAEA CASE for the financial support they have provided throughout my PhD.

Declaration and published work

I declare that the work presented in this thesis is my own except where stated otherwise, and was carried out entirely at the University of Warwick, during the period of September 2006 to September 2009, under the supervision of Prof. S. C. Chapman and Prof. R. O. Dendy. The research reported here has not been submitted, either wholly or in part, in this or any other academic institution for admission to a higher degree.

Some parts of the work reported and other work not reported in this thesis have been published, as listed below:

Published papers

1. K. Kiyani, S. C. Chapman, B. Hnat and R. M. Nicol, Phys. Rev. Lett. **98**, 211101 (2007)
2. R. M. Nicol, S. C. Chapman and R. O. Dendy, The Astrophysical Journal, Volume 679, Issue 1, pp. 862-870 (2008)
3. S. C. Chapman, R. M. Nicol, E. Leonardis, K. Kiyani and V. Carbone, The Astrophysical Journal Letters, **695**, No 2, L185-L188 (2009)
4. R. M. Nicol, S. C. Chapman and R. O. Dendy, The Astrophysical Journal, Volume 703, pp. 2138-2151 (2009)
5. S. C. Chapman and R. M. Nicol, Phys. Rev. Lett., Volume 703, *in press* (2009)

Conference presentations

1. E. Leonardis, R. M. Nicol, S. C. Chapman and R. O. Dendy, *Evolving Magnetohydrodynamic Turbulence in the Quiet Fast Solar Wind*, IOP Plasma Physics Conference, Warwick University, Coventry, UK, poster presentation (2009)

2. R. M. Nicol, S. C. Chapman and R. O. Dendy, *Quantifying the Anisotropy and Solar Cycle Dependence of the "1/f" Energy Range of Solar Wind Fluctuations Observed by ACE*, American Geosciences Union (AGU) General Assembly, San Francisco, USA, poster presentation (2008)
3. E. Leonardis, R. M. Nicol, S. C. Chapman and R. O. Dendy, *ULYSSES at High Solar Latitudes: The Signature of Evolving Turbulence in Quiet Fast Solar Wind*, American Geosciences Union (AGU) General Assembly, San Francisco, USA, poster presentation (2008)
4. R. M. Nicol, S. C. Chapman and R. O. Dendy, *Quantifying the anisotropy of the 1/f energy range of solar wind fluctuations observed by ACE*, Magnetosphere Ionosphere and Solar-Terrestrial (MIST) Autumn Meeting, London, UK, poster presentation (2008)
5. R. M. Nicol, S. C. Chapman and R. O. Dendy, *The signature of evolving turbulence in quiet solar wind as seen by ULYSSES*, Royal Astronomical Society (RAS) NAM/UKSP-MIST Spring Meeting, Belfast, Northern Ireland, poster presentation (2008)
6. R. M. Nicol, S. C. Chapman and R. O. Dendy, *The scaling properties of inertial range turbulence and coronal "1/f" fluctuations as seen by ULYSSES*, Magnetosphere Ionosphere and Solar-Terrestrial (MIST) Autumn Meeting, London, UK, oral presentation (2007)
7. R. M. Nicol, S. C. Chapman and R. O. Dendy, *Quantifying the Turbulent Scaling Properties of the Polar Solar Wind seen by ULYSSES at Solar Minimum*, European Geosciences Union (EGU) General Assembly, Vienna, Austria, poster presentation (2007)

R. M. Nicol

September 2009

Abstract

In this thesis we use techniques associated with the statistical properties of large stochastic datasets to probe the scaling properties of solar wind timeseries. In particular, we consider single-point spacecraft measurements of interplanetary vector quantities such as velocity and magnetic field. These techniques are first applied to well-known distributions such as the normal distribution in order to demonstrate the scaling properties associated with different types of timeseries. For example, a normal distribution can be thought of as the steps of a Brownian walk and is a fractal process or in other words there is a power-law relation between stepsize and the length of the walk. This simple behaviour is complicated when intermittency (similar to large jumps in a random walk) and multifractality are introduced. We also show other model distributions exhibiting these effects and the consequences on the statistical analysis results.

These methods are then applied to *in situ* solar wind observations by monitors such as the ACE and Ulysses spacecraft. ACE occupies a privileged position at the Lagrangian point between the Sun and the Earth, whereas Ulysses was the first spacecraft to explore the Sun's polar regions. We are thus able to show the scaling behaviour of velocity and magnetic field fluctuations for a wide range of different solar wind conditions (such as fast and slow solar wind speeds) and between periods of maximum and minimum solar activity and to examine both ecliptic and polar solar wind behaviour. The large datasets available mean we can probe fluctuations over a wide range of scales from the inertial range to the larger energy containing scales. We find that the polar inertial range (small-scale) behaviour for fast solar wind can be summarised for the magnetic field by a single function, which holds for all components and for different successive solar minima.

We further use ACE measurements to examine the velocity and magnetic field large-scale fluctuations normal and parallel to the local background magnetic field and propose that the parallel velocity component carries the signature of coronal processes convected outwards into the solar wind. The scaling exponents obtained constrain the models for these processes.

Chapter 1

Introduction

1.1 Overview of the Thesis

We first introduce the solar wind and its characteristics, together with the spacecraft which gather the data that we subsequently analyse. We further discuss structures in the solar wind plasma and magnetic field; their presence over a wide variety of scales - from minutes to days and from 10^4 to 10^7 km; and the difficulty in distinguishing between phenomena such as *in situ* generated turbulence and signatures of coronal origin, which have been convected outwards from the Sun by the expanding solar wind. The different scaling models applied to solar wind turbulence are also described, as well as the similarities and differences between magnetohydrodynamic turbulence (MHD) and hydrodynamic turbulence.

We begin in Chapter 2 by describing the statistical methods used and their application to the identification of the known scaling properties of model distributions. This enables us to test the methods and the computational C++ and Matlab codes developed to extract the scaling information. We then apply these techniques to single-point spacecraft measurements of solar wind fluctuations in vector quantities such as velocity and magnetic field. This is of particular interest because there are many different conditions in the solar wind, which can affect the observed scaling. For example, the solar wind has a variable speed depending on local conditions at its coronal origin and on the overall level of solar activity. Observations also depend on the position of the spacecraft, which can be located above the Sun's poles or in the solar ecliptic plane between the Sun and Earth. We differentiate between these different conditions and the results of these studies have been published in Nicol et al. (2008); Chapman et al. (2009a); Nicol et al. (2009).

We also examine the universality of turbulent fluctuations and finite-size effects

in the solar wind, which is a spatially extended system with a finite Reynolds number.

1.2 The Solar Wind

1.2.1 Introduction

The solar wind is a continuous plasma outflow from the Sun (Parker, 1958) characterised by a wide range of structures and turbulent phenomena on different spatial and temporal scales. It permeates the heliosphere, which extends beyond Pluto's orbit to $\sim$ 100 AU (1 AU$\sim 1.496 \times 10^8$ km (p12 Cox, 2000)), a surface known as the heliopause, which is a shock front between the solar wind and the weakly ionised interstellar medium. The heliosphere also contains the entirety of the Sun's magnetic field.

The existence of the solar wind was hypothesised as early as the 1600s by Kepler. It was observed that comets, whether approaching or moving away from the Sun, had tails always pointing away from the Sun. Kepler proposed that this was due to a pressure exerted by sunlight on the dust particles composing these tails. However, this explanation was unable to account for small variations in the tails' directions and even kinks. In 1943, Cuno Hoffmeister, and subsequently Ludwig Biermann, suggested that the Sun was emitting a steady stream of charged particles, as well as photon radiation, which interacted with the charged ions within comet tails (see Stern, 1989, for a review and references therein). It was only in 1958 that Eugene Parker formulated a possible mechanism for this outflow.

The model proposed by Parker (1958) assumes a hot corona, whose expansion out into empty space is only restricted by gravity. As gravity falls off with increasing radial distance, there comes a critical point where the corona has expanded to a sufficiently large radius to allow the high energy plasma particles to flow freely into space. This plasma, or solar wind, would flow at increasingly fast speeds as it moves further away from the Sun. These predictions were later confirmed by the Mariner II mission to Venus in 1962 (Neugebauer & Snyder, 1962).

The possible heating mechanisms of the corona, which provide the thermal energy necessary to drive and accelerate the solar wind, are still the subject of much de-

bate; see for example Belcher (1971); Barnes (1992); Priest et al. (2000); Ofman (2005). The solar wind constitutes then a collisionless plasma ($\rho \sim 3$ cm^{-3}, where ρ is the total heavy particle number density, i.e. electron, ion and proton, in interplanetary space as opposed to $\sim 1 \times 10^8$ cm^{-3} in the corona (Cox, 2000, p50)) in which locally generated and radially convected turbulent phenomena can be observed.

In general we distinguish three types of solar wind, with different coronal origins and characteristics. First, there is the fast solar wind, which originates deep inside open magnetic field regions or coronal holes (dark regions in UV images of the Sun, where the plasma is slightly colder than in surrounding regions) (Krieger et al., 1973). Phillips et al. (1994) use observations from the Ulysses mission to show that the fast solar wind is fairly uniform in speed $\sim$ 750 km s^{-1} and density $\rho_{proton} \sim 3$ cm^{-3} (normalised to 1 AU by R^2, where R is radial distance from the Sun). Second we have the slow wind, which is far more variable in speed (between 250 and 500 km s^{-1}) and much denser than the fast wind ($\rho_{proton} \sim 8 - 10$ cm^{-3}) (McComas et al., 1998b, 2000). The slow solar wind is associated with the streamer belt at the Sun's equator (Gosling et al., 1981; Habbal et al., 1997). The high spatial and temporal variability of streamers (p3 Benz, 2002), which are wisp-like streams of particles travelling through the Sun's corona, is thought to be linked to the high variability of the slow solar wind. Finally coronal mass ejections (CMEs) are responsible for a third type of solar wind. Some of the first CME observations date from the 1970s (MacQueen et al., 1974). They occur when a coronal structure starts to rise, carrying with it large amounts of coronal mass and magnetic flux. CMEs reach velocities of $\sim$ 470 km s^{-1} (Howard et al., 1985) and can be tracked as they move through the heliosphere. The interaction of these different types of wind, combined with the effect of the Sun's rotation, causes the appearance of rarefactions and compressions (respectively low and high pressure regions). The solar wind is also supersonic and superalfvénic. At 1 AU, the sound speed v_S and the Alfvén speed v_A are $\sim 30 - 50$ km s^{-1}, therefore much smaller than the solar wind speed.

1.3 The Solar Magnetic Field

1.3.1 Introduction

On large scales ($\gtrsim$ 1500 km), the Sun has a complex magnetic field topology with regions of varying polarity and magnetic field strength ($0.02 - 0.4$ T) (p365 Cox, 2000). At 1 AU, the ecliptic solar magnetic field has dropped off to $\sim$ 5 nT (p163 Baumjohann & Treumann, 1996). Sunspots are regions of intense, concentrated magnetic fields (Hale, 1908) of $\sim$ 0.3 T (p368 Cox, 2000), which appear as dark spots on the solar surface. Observations of sunspots date as far back as 2000 years by Chinese astronomers ($\sim$ 165 B.C., Stephenson (1990)) and they are an important indication of the level of the Sun's magnetic activity (p36 Lang, 2000). Sunspots are observed to travel in pairs of opposite polarity (Hale et al., 1919) joined by magnetic loops (magnetic flux tubes), which rise up through the photosphere into the corona. Because of its enhanced magnetic field, the region around a bipolar sunspot group is known as an active region and is also characterised by intense X-ray emission (Reidy et al., 1968; Vaiana et al., 1973). Violent and unpredictable solar phenomena such as solar flares (the first observation of a solar flare was by Carrington (1859) and R. Hodgson), which are brief and powerful energy bursts powered by magnetic energy stored in the upper corona (p156 Lang, 2000), are also known to occur in active regions.

1.3.2 The Solar Cycle

Observations of solar magnetic activity show both temporal and spatial evolution characterised by a period known as the solar cycle. Measurements of sunspot numbers by S. H. Schwabe over 17 years from 1826 (Stern, 1989), showed a periodic variation in the average number of sunspots seen on the solar surface over successive years. These results and others were then compiled by Rudolf Wolf, who managed to reconstruct the cycles to 1755 and thus establish the mean length of the solar cycle as $\sim$ 11 years (Meadows, 1970). However, individual solar cycles have been observed to have lengths ranging from 9 to 14 years. $1755 - 1766$ is known as solar cycle 1 and we are currently approaching the end of cycle 23 (year 2009).

The start of a solar cycle is characterised by sunspots appearing in belts of activity at middle solar latitudes $\sim 30°$. The number of sunspots increases and the belts move towards the equator as the cycle progresses (Carrington, 1858). By the time the number of sunspots reaches a maximum, the solar magnetic field is highly disorganised, with numerous regions of opposite magnetic polarity. Before reaching the equator, the sunspots slowly start to disappear and the solar magnetic field evolves to a simple North-South orientated dipole-like configuration (Babcock, 1961). The Sun therefore goes from periods of maximum solar activity to minimum activity every 4 to 7 years. The sunspot behaviour is summarised in a plot known as a butterfly diagram, shown in Figure 1-1. The Sun is divided into equal area latitude strips and the butterfly plot shows the average percentage of solar surface area occupied by sunspots over individual solar rotations for each strip. The characteristic butterfly shape arises from the initial appearance of the sunspots at higher latitudes before they converge to the equator. A regular update of this plot is kept by the Solar Physics Group at NASA's Marshall Space Flight Center.

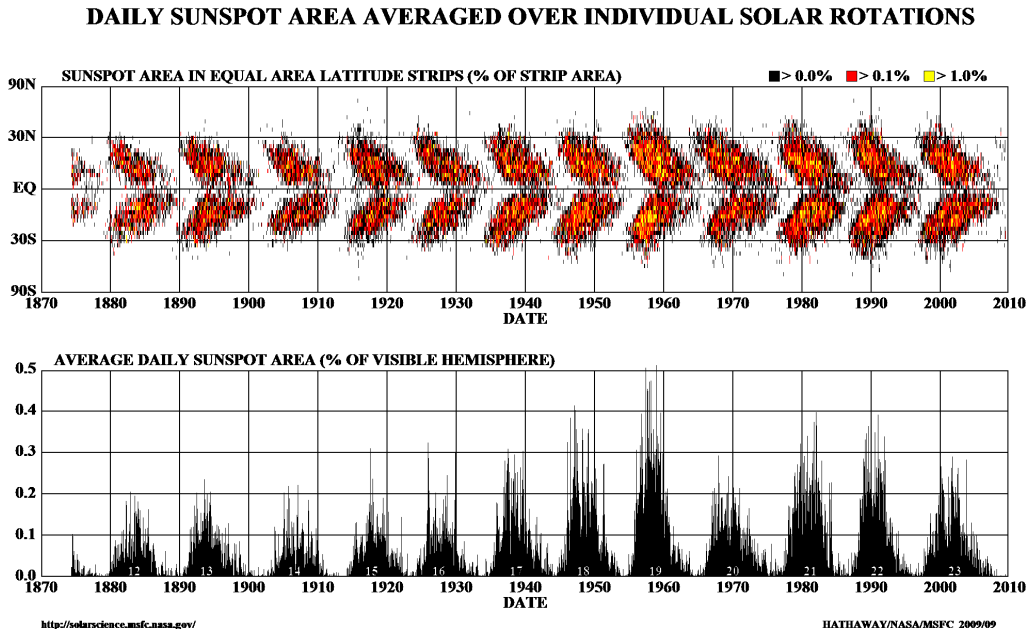

Figure 1-1: These plots show the evolution of the percentage of solar surface area occupied by sunspots as a function of equal area solar latitude strips and time (plot courtesy of NASA online resources, NASA (2009))

1.3.3 The Magnetic Solar Cycle

The Sun also has a magnetic solar cycle, which is approximately twice the sunspot cycle, known as the 22 year Hale cycle after George Ellery Hale ($1868 - 1938$), whose observations on the polarity of sunspots led to its identification. The magnetic polarity of the Sun reverses every solar cycle, meaning the magnetic poles return to the same polarity after two solar cycles. During periods of minimum solar activity, the field is observed to be dipolar with the magnetic dipole axis approximately aligned with the solar rotation axis. A more complex structure is seen at lower latitudes and the equator due to the tilt and warps of the heliospheric current sheet (HCS) (e.g. McComas et al., 2000). The HCS arises from the neutral line at the source solar surface, which divides regions of opposite radial magnetic field polarity (i.e. North and South) (Hoeksema, 1995). This line is swept outwards by the expanding solar wind to form the three dimensional HCS. The twist of the magnetic field lines due to the Sun's rotation causes the HCS to be likened to a ballerina's skirt or a gardener's sprinkler (Figure 1-2).

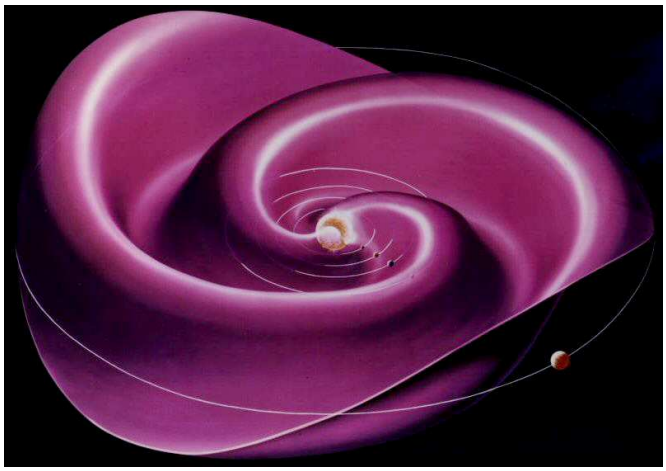

Figure 1-2: Artist's impression of the heliospheric current sheet, which results from the influence of the Sun's rotating magnetic field on the outwardly expanding solar wind. The three dimensional spiral shape has been likened to a ballerina's skirt (Image credit: NASA artist Werner Heil).

Large polar coronal holes are sources of fast uniform solar wind (~ 750 km s^{-1}), carried out on the open magnetic field lines. Slower, denser and more variable solar wind is present at lower latitudes ($< 40^{\circ}$ heliospheric latitude). During times of

maximum solar activity, the magnetic field configuration is far more complex, with a mixture of different flows from active regions, streamers, mid-latitude coronal holes and coronal mass ejections. The dipole configuration is roughly conserved, however the magnetic dipole axis is now approximately normal to the solar rotation axis as it rotates round from pole to pole. All these observations are results from the pioneering Ulysses mission, which was the first spacecraft to leave the solar equatorial plane and explore the Sun's poles. Figure 1-3 was first published on the cover of Geophysical Research Letters, volume 1 in 1998 (McComas et al., 1998a), and shows the change in solar wind velocity and magnetic field polarity though a complete solar latitude scan by Ulysses over $1994 - 1995$, during the first solar minimum of cycle 23.

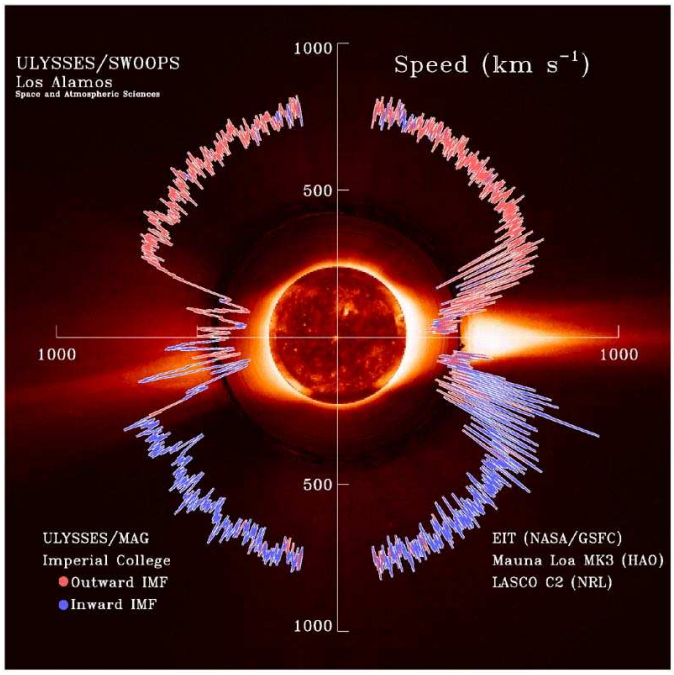

Figure 1-3: Solar wind speed and magnetic polarity measured by Ulysses, as a function of heliolatitude, overlaid with three concentric images taken with the NASA/GSFC EIT instrument (centre), the HAO Mauna Loa coronagraph (inner ring), and the NRL LASCO C2 coronagraph (outer ring). Each 1-hour averaged speed measurement has been color coded to indicate the orientation of the observed interplanetary magnetic field: red for outward pointing and blue for inward (McComas et al., 1998a).

However the mechanisms of the solar magnetic field's origin are still largely unknown, although it is thought the solar dynamo (for a recent review, see Charbonneau,

2005, and references therein) is at least partially responsible.

1.3.4 The Magnetic Carpet

On smaller spatio-temporal scales ($\sim 200 - 300$ km (p365 Cox, 2000)), the photospheric magnetic field forms highly structured areas of magnetic and non-magnetic regions. It is also a dynamic field, threaded by the emerging magnetic flux tubes, whose interaction with the magnetic field already present produces bright points on the solar surface. The magnetic regions are observed to have a granulation different to that of the non-magnetic regions; the granules and lanes between then appearing much smaller (Tarbell et al., 1990). The cellular structures formed by these regions occur on a variety of different scales and do not appear to have a characteristic length scale. A fractal approach is used to model the distribution of these fields.

A fractal (Mandelbrot, 1982) can be loosely thought of as an object, whose structure looks the same at all levels of magnification. In other words, it displays the property of self-similarity. Mandelbrot strictly defines a fractal as *a set for which the Hausdorff Besicovitch dimension strictly exceeds the topological dimension* (p15 Mandelbrot, 1982). The topological dimension d_T is always an integer unlike the Hausdorff Besicovitch dimension or fractal dimension d_f. The fractal (capacity) dimension d_f of the "mass" M of an object measured within a sphere of radius R (Sornette, 2004, p27) embedded in a space of d dimensions with a resolution ϵ is

$$M \propto \epsilon^d \left(\frac{R}{\epsilon}\right)^{d_f} \tag{1-1}$$

This reflects the fact that as the resolution increases (i.e $\epsilon \rightarrow 0$), the "observable mass" of a fixed object of macroscopic size R will decrease, i.e. the fractal object becomes more tenuous. In a Euclidean span $\Re^d$, we have $0 \leq d_T,\ d_f \leq d$ and the two dimensions also satisfy the Szpilrajn inequality $d_f \geq d_T$ (p15 Mandelbrot, 1982). Physically, we can think of d_T as the well known spatial dimensions. In other words, it is the number of independent directions for a point moving in a space of dimension d. For well behaved systems, equation 1-1 can be more simply

expressed as the scaling of the number of elements $N \rightarrow \frac{M}{\epsilon^d}$ at scale $l \rightarrow \frac{\epsilon}{R}$ with l

$$N(l) \propto l^{-d_f} \tag{1-2}$$

For the magnetic carpet, d_f is obtained from the scaling of the area $A(L)$ of solar plages (areas of emerging or reconnecting magnetic field lines) with lengthscale L via the relationship $A(L) \sim L^{d_f}$ (Schrijver et al., 1992). The magnetic carpet fractal dimension was estimated to be $\sim 1.45 - 1.60$ by Schrijver et al. (1992). Power law distributions and fractal behaviour are further observed for solar and stellar flare parameters such as temperature, volume and duration (Aschwanden et al., 2008) for example.

1.3.5 Parker Spiral

The solar magnetic field is carried out with the solar wind, and the magnetic field lines remain anchored in the solar surface, which is an excellent conductor. For ideal magnetohydrodynamics (low resistivity), the frozen-flux condition means that the charged particles leaving the solar surface convect with the field lines, or equivalently the particles "drag" the field lines. If we start from Maxwell's differential equations for Faraday's law of induction and Ampère circuital law (ignoring the displacement current) (p7 Lang, 1999)

$$\boldsymbol{\nabla} \times \boldsymbol{E} = -\frac{\partial \boldsymbol{B}}{\partial t} \, (Faraday) \tag{1-3}$$

$$\boldsymbol{\nabla} \times \boldsymbol{B} = \mu_0 \boldsymbol{J} \, (Circuital \; law) \tag{1-4}$$

here $\boldsymbol{E}$ is the electric field, $\boldsymbol{B}$ is the magnetic field, $\boldsymbol{J}$ is the current density and $\mu_0 = 4\pi \cdot 10^{-7}$ N A^{-2} is the permeability of free space. The electic field $\boldsymbol{E}$ can also be expressed as

$$\boldsymbol{E} = -\boldsymbol{\upsilon} \times \boldsymbol{B} + \boldsymbol{J}/\sigma \tag{1-5}$$

here υ is the flow velocity and σ is the electrical conductivity. Combining these definitions we obtain the induction equation for the magnetic field

$$\frac{\partial \boldsymbol{B}}{\partial t} = \boldsymbol{\nabla} \times (\boldsymbol{\upsilon} \times \boldsymbol{B}) + \frac{1}{\mu_0 \sigma} \boldsymbol{\nabla}^2 \boldsymbol{B} \tag{1-6}$$

The first term on the right-hand side of equation 1-6 represents convection, while the second term represents diffusion. In the perfectly conducting limit, the induc-

tion equation reduces to:

$$\frac{\partial \boldsymbol{B}}{\partial t} = \boldsymbol{\nabla} \times (\boldsymbol{v} \times \boldsymbol{B}) \tag{1-7}$$

This holds when the diffusion of the magnetic field through the plasma is negligible next to the transport of the field along the plasma. This condition is met in solar system plasmas, because of the low collisionality and large spatial scales involved. Due to the Sun's rotation, the field lines then adopt an Archimedean spiral pattern, show in Figure 1-4.

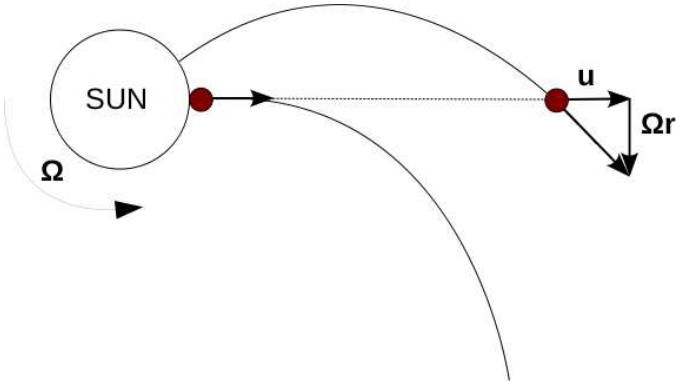

Figure 1-4: The frozen-in field lines result in the Parker spiral interplanetary magnetic field lines geometry. The position of a fluid element is shown as it leaves the Sun's surface and then at a later time, during which the Sun has rotated. The field line's origin is frozen in at the Sun, giving rise to a spiral shape.

This result was first derived by Parker (1958), who assumed a steady state expansion of the solar wind into interplanetary space. If we adopt a reference frame co-rotating with the Sun at angular frequency $\boldsymbol{\Omega}$ and assume a purely radial flow (passive magnetic field), the velocity of a fluid particle leaving the Sun is given by (p193 Priest, 1985)

$$\boldsymbol{v} = u\hat{\boldsymbol{r}} - \Omega r\hat{\boldsymbol{\theta}} \tag{1-8}$$

where $\hat{\boldsymbol{r}}$ and $\hat{\boldsymbol{\theta}}$ correspond to spherical coordinates and $\boldsymbol{r}$ is the radial distance from the solar surface. The frozen-flux assumption means that the flow and the field lines are parallel to each other, i.e. $\boldsymbol{v} \times \boldsymbol{B} = 0$. This means that the field components are in the ratio

$$\frac{B_\theta}{B_r} = -\frac{u_\theta}{v_r} = -\frac{u}{\Omega r} \tag{1-9}$$

From Maxwell's equations, $\nabla \cdot \boldsymbol{B} = 0$ or equivalently the magnetic flux though a closed surface is zero, so that $\boldsymbol{B_r} \propto 1/r^2$. If we further assume $\boldsymbol{u}$ to be constant, which is a reasonable approximation throughout most of the heliosphere, we then obtain the magnetic field lines following their characteristic spiral shape. At 1 AU, the tangential and radial velocity components are comparable in magnitude. To summarise, solar wind elements, which originate from the same place on the solar surface, are connected by spiral magnetic field lines.

1.3.6 Structures and Scaling in the Solar Wind

The solar wind carries signatures of coronal dynamics as well as locally generated turbulent phenomena, which span a broad range of scales. Generalizing somewhat, the solar wind spectral power density is observed to scale approximately as f^{-1} (Ruzmaikin et al., 1995a; Goldstein et al., 1995b) at lower frequencies ($\leq$ 1 mHz); and as $f^{-5/3}$ (Ruzmaikin et al., 1993; Horbury et al., 1995a), reminiscent of the inertial range of Kolmogorov (1991a), at higher frequencies ($\sim$ 10 mHz-100 mHz). The frequency at which the transition occurs ($\sim$ 1 mHz-10 mHz) between these two power laws is observed to decline with increasing distance from the sun in the plane of the ecliptic (see Feynman et al., 1995; Horbury et al., 1996a). This extension of the $f^{-5/3}$ range to lower frequencies at greater distances can be interpreted as evidence for an active turbulent cascade (Goldstein et al., 1995b; Horbury & Balogh, 1997) that evolves a growing inertial range as time passes in the outward propagating plasma. The f^{-1} component is taken to reflect embedded coronal turbulence, convected with the solar wind plasma (Matthaeus & Goldstein, 1986). It is ubiquitous in the solar wind and is seen at all latitudes and radial distances. It is not yet certain whether, in addition, this coronal turbulence acts as the low frequency large-scale driver of the inertial range turbulence. The $f^{-5/3}$ fluctuations are often predominantly shear Alfvénic in character, that is incompressible and displaying correlation or anticorrelation between perturbations of the magnetic field and of fluid velocity (Smith et al., 1995). Figure 1-5 is taken from (Bruno & Carbone, 2005) and shows the power density spectra of magnetic field fluctuations observed by Helios 2 between 0.3 and 1 AU.

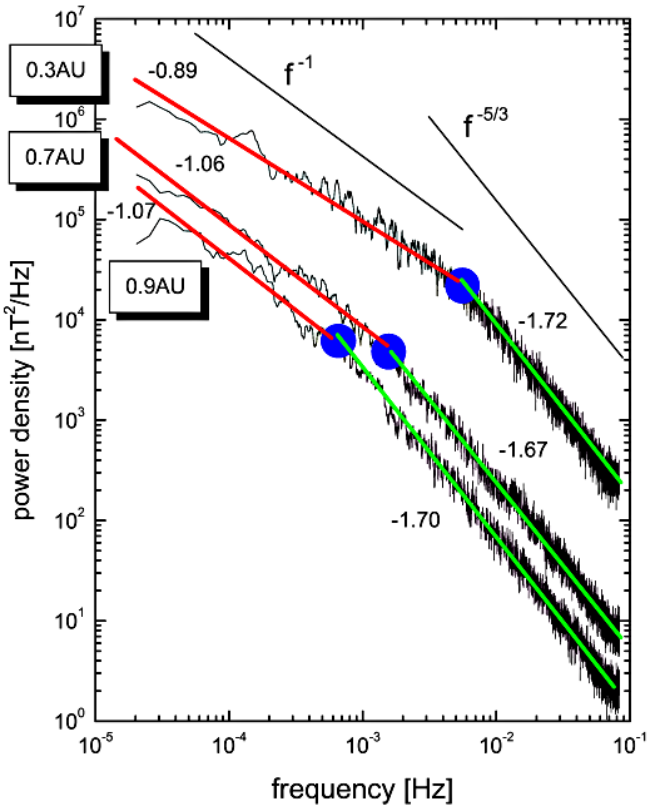

Figure 1-5: From (Bruno & Carbone, 2005), the power density spectra of magnetic field fluctuations observed by Helios 2 between 0.3 and 1 AU during its first mission to the Sun in 1976. The spectral break (blue dot) shown by each spectrum, moves to lower frequencies as the heliocentric distance increases.

The first observations initiated a debate as to whether the fluctuations are of solar coronal origin, simply passively advecting with the flow, or whether they are dominated by locally evolving turbulence (Goldstein, 2001). The inertial range fluctuations, and the crossover to f^{-1} behaviour, show secular variation with heliocentric distance (Horbury et al., 1996a). This is consistent with evolving, rather than fully evolved, turbulence. Helios data, in conjunction with Ulysses, has been used by Goldstein et al. (1995a), to show that the f^{-1} region contains scales, which are too large to be produced *in situ* and are progressively eaten away by the smaller scale turbulence, which must therefore be active. The large scale magnetic structure of the corona also varies with both heliospheric latitude and solar cycle, and this is clearly manifested in the coherent structures and variation of wind speed that are observed (Phillips et al., 1995). A key question, and the fo-

cus of this thesis, is the interplay between the large scale coronal driver and the evolving inertial range turbulence. This is studied by examining their dynamics over a wide range of scales.

1.4 Turbulence in the Solar Wind

The solar wind is a low-density ionised gas dominated by collective effects. Insofar as turbulent and non-linear phenomena occur in the solar wind similarly to turbulence in hydrodynamic flows in the limit of infinite Reynolds number; we anticipate that the methods and equations used in hydrodynamics can be extended to magnetohydrodynamics. The motion of an unmagnetised nonconducting fluid is governed by the Navier-Stokes equations, and turbulence arises from the non-linear terms contained in these equations. For an incompressible fluid, these have the form (p1 Frisch, 1995)

$$\frac{\partial \boldsymbol{v}}{\partial t} + \boldsymbol{v} \cdot \boldsymbol{\nabla} \boldsymbol{v} = -\nabla p + \nu \boldsymbol{\nabla^2} \boldsymbol{v}, \tag{1-10}$$

$$\boldsymbol{\nabla} \cdot \boldsymbol{v} = 0 \tag{1-11}$$

where $\boldsymbol{v}$ is velocity, p is pressure and ν is kinematic viscosity.

The equations are then supplemented with initial and boundary conditions, which arise from the nature of the problem considered. In (1-10), if we take U and L to be respectively a characteristic velocity and length scale of the the flow, we can form a control parameter known as the Reynolds number, R_E (p31 Acheson, 1990).

$$\begin{aligned} inertia\ term\ &:\ |(\boldsymbol{v} \cdot \boldsymbol{\nabla})\boldsymbol{v}| = O(U^2/L) \\ viscous\ term\ &:\ |\nu \boldsymbol{\nabla^2} \boldsymbol{v}| = O(\nu U/L^2) \\ R_E = \frac{|inertia\ term|}{|viscous\ term|} &= O\frac{U^2/L}{\nu U/L^2} = \frac{UL}{\nu} \end{aligned} \tag{1-12}$$

From this definition, it is easy to see that a high Reynolds number implies either a low viscosity of the fluid or that $L/\nu \to \infty$ (e.g. Chapman et al., 2009b), i.e. L is very large. In the second case, an extended inertial range would be observed with many excited modes. Phenomenological studies of the flow past a cylinder (p3-11 Frisch, 1995), also show that as the Reynolds number is slowly increased,

symmetry breaking and instabilities arise in the fluid, leading to fully developed turbulence at very high Reynolds numbers. The formation of eddies in the fluid on a wide variety of different spatial scales is observed, which implies the presence of some form of statistical self-similarity or scale-invariance.

The analogous control parameter in plasma turbulence is the magnetic Reynolds number $R_m = 4\pi UL/\eta$ (p212 Lang, 1999), where U is again a typical velocity, L is a typical length scale and η is the electric resistivity. For $R_m > 1$, transport dominates over diffusion, i.e. the magnetic lines of force move with the fluid. A method of estimating the effective magnetic Reynolds number in solar wind flows at $\sim$ 1 AU using the Cluster spacecraft is detailed in (Matthaeus et al., 2005). Matthaeus et al. (2005) use the fact that the R_m can also be expressed as a ratio of the outerscale of the turbulence L_0 to the Taylor microscale L_T (p61 Frisch, 1995) by $R_m = (L_0/L_T)^2$ (p107 Frisch, 1995), they find $R_m = 2.3 \times 10^5$.

The simplest set of equations to describe the solar wind are given by incompressible magnetohydrodynamics (MHD). This assumption is often justified by observations of a high (anti)correlation between magnetic and velocity fields, which indicates the presence of shear Alfvén waves. The incompressible MHD equations are given below (see for example Biskamp (chap.2 1993)) and are similar to equations 1-10 and 1-11, however with the added complication of a background magnetic field, introducing anisotropy:

$$\frac{\partial \rho}{\partial t} + \boldsymbol{\nabla} \cdot \rho \boldsymbol{v} = 0 \, (\textit{continuity}) \tag{1-13}$$

$$\rho \left[\frac{\partial \boldsymbol{v}}{\partial t} + (\boldsymbol{v} \cdot \boldsymbol{\nabla}) \boldsymbol{v} \right] = -\nabla p - \frac{1}{\mu_0} \boldsymbol{B} \times (\boldsymbol{\nabla} \times \boldsymbol{B}) \, (\textit{momentum}) \tag{1-14}$$

$$\frac{\partial \boldsymbol{B}}{\partial t} = \boldsymbol{\nabla} \times (\boldsymbol{v} \times \boldsymbol{B}) \, (\textit{induction}) \tag{1-15}$$

$$\boldsymbol{\nabla} \cdot \boldsymbol{v} = 0 \, (\textit{incompressibility}) \tag{1-16}$$

Here $\boldsymbol{B}$ is the magnetic field, p is the thermodynamic (or kinetic) pressure and μ_0 is the permeability of free space.

A qualitative picture of solar wind turbulence is given by Richardson's energy cascade model (1922), a nonlinear transfer of energies via smaller and smaller scale eddies from the energy injection-scale, l_0, to the viscous dissipation scale, l_{vis}, which is known as the inertial range. Sahraoui et al. (2009) use Cluster data to show that the dissipation range has two breakpoints at 0.4 and 35 Hz, which cor-

respond respectively to the Doppler-shifted proton and electron gyroscales. This picture is further complicated by the anisotropic (background $\boldsymbol{B}$) and intermittent (i.e. non-space filling) nature of the solar wind. Various models attempt to describe the global statistical behaviour of turbulence and have been applied with varying levels of success to this system, starting with Kolmogorov's famous 1941 theorem for hydrodynamic turbulence.

1.4.1 Kolmogorov Turbulence (K41)

Kolmogorov's 1941 paper (Kolmogorov, 1991b) makes the assumption of locally isotropic time-steady homogeneous fluid turbulence. These restrictions are imposed on the velocity differences' probability density laws, not on the velocities themselves. The important step here is that although the mean flow and large scale fluctuations are generally inhomogeneous and anisotropic, it is assumed that on sufficiently small scales the statistical regime may be taken as homogeneous and isotropic (p14 Monin & Yaglom, 1971). This assumption only holds for very large Reynolds numbers and arises from considering the highly chaotic nature of the energy transfer. This causes any orientating effect of the mean flow to be lost as smaller and smaller scales are reached.

The time-steady condition implies that the energy injection rate into the system, the energy transfer rate and the energy dissipation rate must all be equal on average, i.e. there is no build-up of energy at any scale. The energy cascade can then be thought of in the following way: the averaged flow has first-order fluctuations arising from the displacements of different fluid volumes of average diameter, l_0. We can further characterise their movement by defining an associated velocity, υ_0. For very large R_E, these fluctuations will in turn generate their own diameter and velocity fluctuations, respectively l_1 and υ_1. This process will continue down to a scale n, with $R_{E,n} = l_n \upsilon_n / \nu$, where the effect of viscosity will be strong enough to prevent the formation of any further orders of fluctuations. If we now consider the energy transfers, this is equivalent to the first-order fluctuations absorbing the motion's energy and passing it on to the second order fluctuations, and so on until the energy is dissipated as heat by viscous processes. The fluctuations (or eddies) are also considered to be space-filling at all scales.

Kolmogorov considered the second moment of the velocity increments, defined as

$$S_{m=2} = \langle \boldsymbol{\delta v}(\boldsymbol{l})^{m=2} \rangle \tag{1-17}$$

where:

$$\boldsymbol{\delta v}(\boldsymbol{r}, \boldsymbol{l}) = \boldsymbol{v}(\boldsymbol{r} + \boldsymbol{l}) - \boldsymbol{v}(\boldsymbol{r}) \tag{1-18}$$

and $\boldsymbol{v}(\boldsymbol{r})$ is the velocity at position $\boldsymbol{r}$, $\boldsymbol{v}(\boldsymbol{r} + \boldsymbol{l})$ is the velocity at a position $(\boldsymbol{r} + \boldsymbol{l})$, m is the order of the moment considered and the angular brackets denote spatial averaging. S_m is also known as the structure function (p220 Biskamp, 1993) (p19 Bohr et al., 1998).

Under the further hypothesis that the probability density functions of $\boldsymbol{\delta v}(\boldsymbol{l})$ depend only on ε, defined as the average dissipation of energy per unit mass and time, and on the viscosity ν and that for the inertial range, where $l >> l_{vis}$, this reduces to a single dependence on ε, Kolmogorov derived the well known $2/3^{rds}$ law

$$S_2 = C\varepsilon^{2/3} l^{2/3} \tag{1-19}$$

Here C is some universal dimensionless constant, which can be measured. However Landau pointed out in 1942 that there is no reason to suppose C is universal, because the averaging process depends on the variation of ε over the turn-over times of the large eddies ($\simeq l_0$). This variation is different for different flows, implying that the averaging does not have a universal behaviour (Landau & Lifshitz, 1987). A further argument is also presented by Frisch (1991).

Under the assumption that the turbulent flow is self-similar at small scales, the velocity increments can also be expressed in terms of a unique scaling exponent, $h \in \Re$ (Frisch, 1995, p75):

$$\boldsymbol{\delta v}(\boldsymbol{r}, \lambda \boldsymbol{l}) = \lambda^h \boldsymbol{\delta v}(\boldsymbol{r}, \boldsymbol{l}), \quad \forall \lambda \in \Re_+ \tag{1-20}$$

for all $\boldsymbol{r}$, and where the increments $\boldsymbol{l}$ and $\lambda \boldsymbol{l}$ are smaller than l_0, the integral or energy-injection scale. Upon comparison of (1-19) and (1-20), it can be seen that the only consistent value of h is $h = 1/3$. This gives the following generalization of (1-19) for moment m, taking into account the non-universal nature of C:

$$S_m = \langle \boldsymbol{\delta v}(\boldsymbol{l})^m \rangle = C_m \varepsilon^{m/3} l^{m/3} \tag{1-21}$$

It can be noted that the scaling exponent for l, i.e. $S_m(l) \sim l^{\zeta(m)}$, then has the general form $\zeta(m) = mh$, with $\zeta(3) = 1$ in this case.

In 1941, Obukhov proposed another form of this assertion (p14 Monin & Yaglom, 1971) known as the $5/3^{rds}$ law. This states that the spectral density of the kinetic energy of turbulence over the spectrum of wavenumbers k in the inertial range has the form:

$$E(k) = C_k \varepsilon^{2/3} k^{-5/3} \tag{1-22}$$

where C_k is again a dimensionless constant known as the Kolmogorov constant. Fits to experimental data imply $C_k = 1.7 \pm 0.2$ (p32 Bohr et al., 1998). The power spectral index, α, defined by $E(f) \propto f^{-\alpha}$ where $E(f)$ is the power spectrum, is then related to $\zeta(2)$ by:

$$\alpha = 1 + \zeta(2) \tag{1-23}$$

A more mathematically detailed derivation of this is given in Chapter 2. For the moment, we see that this holds for Kolmogorov by recalling that $\langle v^2(l) \rangle \propto \langle E(l) \rangle \propto l^{2/3}$, that $k \propto 1/l$ and that the power spectrum is given by a Fourier transform of $E(l)$.

It is interesting to note that (1-22) can also be obtained by dimensional analysis upon application of the Buckingham-Pi theorem (e.g. chap.8 Longair, 2003).

Finally Kolmogorov (1991a) derived one of the few exact results in turbulence, namely the $4/5^{ths}$ law. Starting from the Navier-Stokes equations and under the assumptions of isotropy, homogeneity and finite density of energy dissipation, it can be shown that (chap.6 Frisch, 1995)

$$\langle \delta v_{||}^3(l) \rangle = -\frac{4}{5} \varepsilon l \tag{1-24}$$

where $\delta v_{||}^3(l)$ denotes the third order longitudinal velocity increments. This result is only valid for the inertial range when $\nu \to 0$ and $R_E \to \infty$; finite viscosity would necessitate the inclusion of an extra ν-dependent term. Politano and Pouquet (Politano & Pouquet, 1998b,a) use Elsässer variables (linear combinations of magnetic field fluctuations in velocity/Alfvén units and velocity fluctuations) to extend the $4/5^{ths}$ law to MHD. Instead of third order longitudinal velocity fluctuations, the scaling of mixed longitudinal third order structure functions formed from Elsässer variables is now considered. At high frequences (small scales) the

Hall effect also becomes important and Galtier (2008) uses Hall MHD to derive exact scaling laws for the third order correlation tensors for the velocity, magnetic and current density fields. In (Galtier, 2009), axisymmetric MHD is also considered for which Galtier derives an exact vectorial law. This has a form close to the isotropic case considered by Politano et al. (1998).

Studies of the magnetic field and velocity increments in the fast solar wind do indeed show, over certain temporal ranges, power spectra with a $-5/3^{rds}$ trend (Horbury et al., 2005) (Bruno & Carbone, 2005, p72), i.e. Kolmogorov-like behaviour. However power spectra are often noisy and this result is often subject to large errors. Other behaviours are also present and phenomena such as Alfvén waves need to be considered.

1.4.2 Kraichnan-Irishnikov Turbulence (IK)

Shear perturbations in the magnetic field travel at the Alfvén speed ($V_A = B/\sqrt{\mu_0 \rho}$) along the background field as Alfvén waves, which are therefore transverse and electromagnetic (Cravens, 1997, p 131). In 1965, Kraichnan (Kraichnan, 1965) suggested that Kolmogorov's inertial range law only applies to hydrodynamic theory and needs to be modified for the hydromagnetic case. Independently, Iroshnikov developed a similar theory in 1964 (Iroshnikov, 1964).

The effect of including shear Alfvén waves, which propagate either parallel or anti-parallel to the background magnetic field B_0, is to decrease the energy transfer rate. Effectively the eddy decay time in the energy cascade model is taken to be longer than the Alfvén decorrelation time, $\tau_A(l) = l/\upsilon_A$ where l is the fluctuation scale and υ_A the Alfvén speed. Decorrelation now occurs before the full eddy decay or energy transfer to the next scale, has happened. The energy transfer time is thus increased by a factor of τ_E/τ_A, where τ_E is the eddy turnover time. This leads to a different spectral density dependence over the inertial range:

$$E(k) = C_k(\varepsilon B_0)^{1/2} k^{-3/2} \tag{1-25}$$

and a structure function scaling exponent $\zeta(m) = m/4$, smaller than the $m/3$ expected from K41. We also note that if the energy transfer rate is constant, in this model $\zeta(4) = 1$ is an intermittency free parameter. In contrast to $\zeta(3) = 1$

obtained from K41. However this is again a linear model, which takes no account of the intermittent (or inhomogeneous) nature of the solar wind, which we define next.

1.4.3 The β Model and Intermittency

Intermittency occurs when the statistics of a process are dominated by large occasional events, structures and dissipation processes. The intermittent nature of a flow can be determined by calculating the flatness, also known as the kurtosis. The flatness is the normalised fourth central moment of a distribution and estimates the importance of the distribution's tails. A random function $v(t)$ in the temporal domain is then said to be statistically intermittent if at small sampling scales τ (high frequency) the flatness (Frisch, 1995, p122):

$$F(\tau) = \frac{\left\langle (v_\tau(t))^4 \right\rangle}{\left\langle (v_\tau(t))^2 \right\rangle^2} \tag{1-26}$$

grows without bounds as τ goes to smaller and smaller scales, or equivalently as the frequency increases to higher sampling rates. For a Gaussian distribution, the kurtosis can be shown to be $F_G = 3$. A quantify often examined in then the compensated kurtosis, $F(\tau) - F_G$, which is a measure of the extent of the considered distribution's deviation from Gaussianity.

The β model was first developed by Frisch *et al.* (1978) in an attempt to incorporate intermittency into the description of the turbulent cascade using a fractal approach. An example of a simple fractal structure is the well known Cantor set or "middle-third deletion". With each scale, the number of "gaps" in the structure increases. Figure 1-6 shows the first four iterations of a Cantor set.

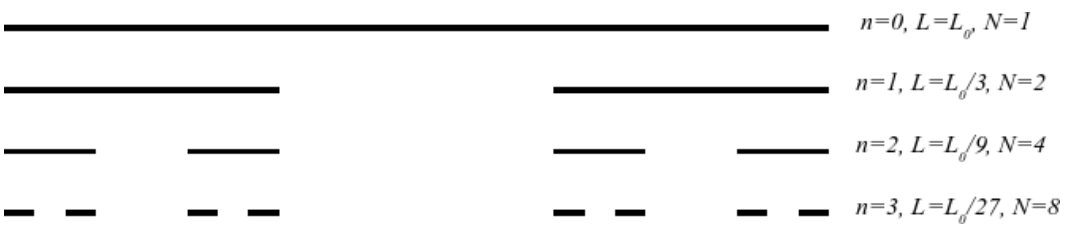

Figure 1-6: The first four iterations of a Cantor set: as the number of iterations increases, so does the number of "gaps" in the structure. The length of an element at iteration n is given by $L = L_O/3^n$ and the number of elements at iteration n is then $N = 2^n$. The fractal dimension is given by $d_f = log(2)/log(3) \sim 0.631$.

Applying these ideas to turbulence, the eddy decay process still happens as described previously, except not all possible daughter eddies are produced. In other words, there are "gaps" in the fluctuations on every scale. The parameter μ is introduced as a measure of the intermittency. If β $(0 < \beta < 1)$ is defined as the fraction of daughter eddies of size $l = r^n/L_0$ produced then:

$$\beta = r^{\mu} \tag{1-27}$$

Generally $r = 2$ is chosen for simplicity. μ is also known as the codimension and $\mu = 3 - D$ where D is the fractal dimension. From equation 1-27 we can see that μ ranges from $\mu \to 0$ for $\beta \to 1$ (non-intermittent case) to $\mu \to -\infty$ for $\beta \to 0$ (most intermittent case).

The scaling of the velocity fluctuations is also modified by this non space-filling behaviour. At increasingly small scales, the eddies occupy less and less space, which causes the velocity fluctuations in active eddies to decrease less rapidly with scale than for the Kolmogorov model. By again considering the simple process of energy transfer by eddy decay it can be shown that the m^{th} moment of the velocity fluctuations varies with scale as follows:

$$\delta v^m(l) \sim l^{\zeta(m)} \tag{1-28}$$

The scaling exponent, $\zeta(m)$, now has a μ dependence:

$$\zeta(m) = (1 - \mu)(m/3) \tag{1-29}$$

A measure of the intermittency and deviation from Kolmogorov is often given by considering the difference between the measured value of the exponent for the

sixth order velocity structure function and its K41 value of 2 (Frisch, 1995, p130), which is similar to μ in (1-29) for $m = 6$. However, this does mean that we need to go to $m = 6$ for K41 and $m = 8$ for IK, which makes intermittency difficult to study experimentally.

Previously, the structure functions, S_m, were seen to scale as the velocity fluctuations, $|\delta v|^m$, (1-21). This is because, when the eddies are space-filling, there is no difference between the average velocity fluctuation, $\langle|\delta v|^m\rangle$ over a scale l within the inertial range and a single velocity perturbation over eddies on that scale. However this is no longer the case for the β model, where the average velocity is maller than the corresponding fluctuation over an active eddy. This can be shown by noticing that the fraction of space, which is active, decreases as a power of l. Consider the following energy cascade:

$$l_n = r^{-n} l_0 \tag{1-30}$$

The fraction of active space on the scale l_n is therefore given by β^n. The average velocity fluctuations can then be expressed as:

$$\langle|\delta v(l_n)|^m\rangle = \beta^n \delta v^m(l_n) \tag{1-31}$$

now recalling the definition of β from (1-27) and using (1-30) to express r^{-n} as a function of l_n we obtain:

$$\langle|\delta v(l_n)|^m\rangle \propto l_n^{\mu} \delta v^m(l_n) \tag{1-32}$$

We then obtain the following scaling relationship for the structure functions:

$$S_m(l) \propto l^{\mu} l^{\varsigma_m} \propto l^{\zeta(m)} \tag{1-33}$$

where the exponent is given by:

$$\zeta(m) = \mu + \varsigma_m = m/3 + \mu(1 - m/3) \tag{1-34}$$

See also (Chapman et al., 2005b) for a general topological discussion. The β model was extended to MHD turbulence, i.e the Kraichnan-Iroshnikov theory, by Ruzmaikin *et al.* (1995). The MHD β model yields the following expression for the structure function scaling exponent:

$$\zeta(m) = m/4 + \mu(1 - m/4) \tag{1-35}$$

This model still yields a linear dependence of the scaling exponent $\zeta(m)$ on m, even with the inclusion of an adjustable parameter. Experimental evidence does not confirm this behaviour (e.g. Borgas, 1992) and non-linear scaling of the $\zeta(m)$ must be considered.

1.4.4 The p-Model and Multifractality

The previous models assume a fractal behaviour of the turbulence considered, implying a unique value of the scaling exponent h. If instead a multifractal approach is attempted, any experimentally observed non-linear behaviour of the $\zeta(m)$ exponents of the velocity structure functions can now be included in the system's description as well as intermittency.

To go from a fractal to a multifractal approach, it is necessary to weaken the assumption of global scaling invariance (Frisch, 1995, p144) (Bohr et al., 1998, p34) made by Kolmogorov, to one of local scaling invariance. This now means that a continous range of values of h is permitted, i.e for each h in the allowed range, there is a set $\varphi_h \subset \Re^3$ of fractal dimension $d_f(h)$, such that, as $l \to 0$:

$$\frac{\delta\upsilon(\boldsymbol{r})}{\upsilon_0} \sim \left(\frac{l}{l_0}\right)^h, \quad \boldsymbol{r} \in \varphi_h, \;\; dim\varphi_h = d_f(h) \tag{1-36}$$

The fractal dimension d_f characterises the scaling structure of an object and can coincide with the usual topological dimension of the object (see for example Paladin & Vulpiani, 1987). However the advantage of the fractal approach to turbulence is that intermittency can be included by considering $d_f < 3$. Consider the fractal Cantor set shown previously, a multifractal Cantor set can be constructed by distributing a weight at each iteration such that each segment recieves a fraction p_1 and p_2 and $p_1 + p_2 = 1$. Figure 1-7 shows the first few iterations of this set for $p_1 = 1/3$ and $p_2 = 2/3$ (p351 Lynch, 2007).

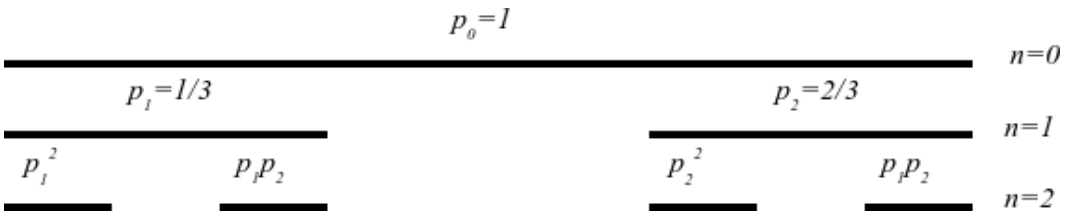

Figure 1-7: The first three iterations of a multifractal Cantor set: at each iteration the two segments recieve different weights $p_1 = 1/3$ and $p_2 = 2/3$.

Real-world examples of multifractals include galaxy distributions (see for example Borgani et al., 1993, and references therein) and even phytoplankton distributions in turbulent coastal waters (Seuront et al., 1999).

The β model detailed previously was extended and developed as the random β model by Paladin & Vulpiani (1987). Here, intermittency and a multifractal approach are incorporated by considering eddies of different shapes and dimensions, and instead of a single value of β, a probability density is used. This means that different structures, like eddies or sheets, are generated with different occurrence probabilities. Burlaga (1991) studied intermittent turbulence in the solar wind at ~ 8.5 AU and showed that these observations are consistent with a random β model prediction, which assumes that the turbulence is a mixture of sheets and space-filling eddies.

Meneveau & Sreenivasan (1987) presented another multifractal model, known as the p-model, for fully developed turbulence. A simple example of this is to consider an eddy decaying into two smaller ones. The parent transfers a fraction p of its energy to one of them and a fraction $(1-p)$ to the other one. By convention $p \geq 1/2$ and values of $\zeta(m)$ are given by:

$$\zeta(m) = 1 - log_2\left(p^{m/3} + (1-p)^{m/3}\right) \tag{1-37}$$

This reduces to Kolmogorov for $p = 1/2$. If we wished to consider Kraichnan-like turbulence the $\zeta(m)$ equation becomes:

$$\zeta(m) = 1 - log_2\left(p^{m/4} + (1-p)^{m/4}\right) \tag{1-38}$$

Various studies such as Horbury *et al.* (Horbury & Balogh, 1997), have shown good agreement between this model and experimentally observed high solar latitude magnetic field fluctuations from the Ulysses mission for $p \sim 0.7$.

1.4.5 The She-Leveque Model

One of the more recent intermittent turbulence models to be developed is the She-Leveque model (She & Leveque, 1994). The inertial range turbulent energy dissipation field is coarse-grained and the most intermittent structures thus obtained are postulated to be filament-like. At each inertial range scale l, where $l_{vis} << l << l_0$, the fluctuations are assumed to be in statistically steady-state and a continuous energy cascade from the largest to the smallest scale is hypothesised. This again allows the scaling behaviour of the velocity increments, δv, and the energy dissipation rate, ε on a scale l to be expressed as:

$$\langle \delta v^m(l) \rangle \sim l^{\zeta(m)}, \quad \langle \varepsilon^m(l) \rangle \sim l^{\tau(m)} \tag{1-39}$$

By using the relationship between δv and ε given by the $4/5^{ths}$ law (1-24), the following relationship can be derived between the structure function exponent, $\zeta(m)$, and the energy dissipation exponent, $\tau(m)$:

$$\zeta(m) = m/3 + \tau(m/3) \tag{1-40}$$

For Kolmogorov turbulence this results in $\tau(m/3) = 0$, which is expected because the Kolmogorov theory assumes a constant energy dissipation rate, independent of the scale l. However as previously discussed, experimental results diverge strongly from this behaviour. The She-Leveque model proposes expressions for $\zeta(m)$ and $\tau(m)$ without having recourse to any adjustable parameters such as p in the p-model or β in the random β model. The main assumptions are that anomalous scaling laws arise from a divergent scaling dependence of $\varepsilon^{m=\infty}(l)$ as $l \to 0$. The presence of intermittent structures is postulated to be the origin of this divergence. $\varepsilon^{m=\infty}(l)$ can then be thought of as the coarse-grained intensity of the most intermittent structures, which are modelled as filaments or 1D objects, embedded in neutral fluid turbulence. The following expression for $\varepsilon^{m=\infty}(l)$ is then derived:

$$\varepsilon^{\infty}(l) \sim l^{-2/3} \tag{1-41}$$

By then postulating a universal scaling relation between scalings of successive structures and a K41 energy transfer scaling, She and Leveque obtain:

$$\zeta(m) = \frac{m}{9} + 2\left[1 - \left(\frac{2}{3}\right)^{m/3}\right] \tag{1-42}$$

$$\tau(m) = -\frac{2}{3}m + 2\left[1 - \left(\frac{2}{3}\right)^{m}\right] \tag{1-43}$$

This model was extended by Politano & Pouquet (1995) to include MHD turbulence, within the framework of Iroshnikov-Kraichnan theory. Instead of the Kolmogorov $5/3^{rds}$ energy transfer scaling, the 3/2 law defined in (1-25) is used. The new results for the scaling exponents are:

$$\zeta(m) = m/9 + 1 - (1/3)^{m/3} \tag{1-44}$$

$$\tau(m) = \frac{2m}{3} + 1 - (1/3)^{m} \tag{1-45}$$

There is another school of thought which argues that the anisotropy present in the solar wind, due to the Alfvénic perturbations, cannot be adequately modelled by the Kraichnan-Iroshnikov scaling. Goldreich & Sridhar (1995) formulated these ideas quantatively in the context of a strong turbulence MHD theory, i.e. the turbulence that develops when an incompressible, magnetized fluid is strongly perturbed. By contrast, in weak turbulence the perturbations are small.

1.4.6 Goldreich-Sridhar Energy Cascade

The strong background magnetic field with respect to small-scale magnetic field fluctuations present in the solar wind means that simulations and observations show anisotropy, in direct contradiction to the isotropy often assumed when calculating the MHD spectrum (e.g. Biskamp & Müller, 2000). Goldreich & Sridhar (1995) present a model of anisotropic MHD turbulence, whose main features are an anisotropic spectrum with $k_{\parallel} \sim k_{\perp}^{2/3} L^{-1/3}$ with respect to a background magnetic field (L is the outer or energy injection scale) and a 1D energy spectrum $\propto k_{\perp}^{-5/3}$ or in other words the Kolmogorov spectrum. If we consider the energy cascade picture, with energy cascading through eddies on smaller and smaller scales, then the scaling relationship between $k_{\parallel}$ and $k_{\perp}$ means that the sizes of the parallel and perpendicular eddies are also correlated. As we move to higher $k_{\perp}$,

the eddies become elongated along the direction of the magnetic field, also only shear Alfvén waves are considered, therefore magnetic (δb_A) and velocity (δv_A) field perturbations only occur perpendicular to the background field. If we take λ as the transverse eddy size and l as the parallel eddy length, then a critical balance is achieved when $V_A/l \sim \delta v_A/\lambda$: during the time l/V_A it takes for two eddies travelling in opposite directions along the magnetic field to cross each other, the magnetic field lines are displaced in the perpendicular direction by $\delta v_A \cdot l/V_A$. This distance is equated to the transverse eddy size λ. The energy transfer time for all scales is then

$$\tau_{transfer}(\lambda) \sim l/V_A \sim \lambda/\delta v_A \tag{1-46}$$

If we assume the energy tranfer rate to be constant, i.e. $\varepsilon \sim \delta v_A^2/\tau_{transfer}(\lambda) = constant$, then we find simply $\delta v_A \propto \lambda^{1/3} \propto k_\perp^{-1/3}$. This leads to an energy spectrum in the perpendicular direction of the Kolmogorov form

$$E(k_\perp) = |\delta v_A|^2 k_\perp^{-1} \propto k_\perp^{-5/3} \tag{1-47}$$

In Fig. 1-8 we summarise the different behaviour of the structure function scaling exponent, $\zeta(m)$, as a function of m for the various models described previously.

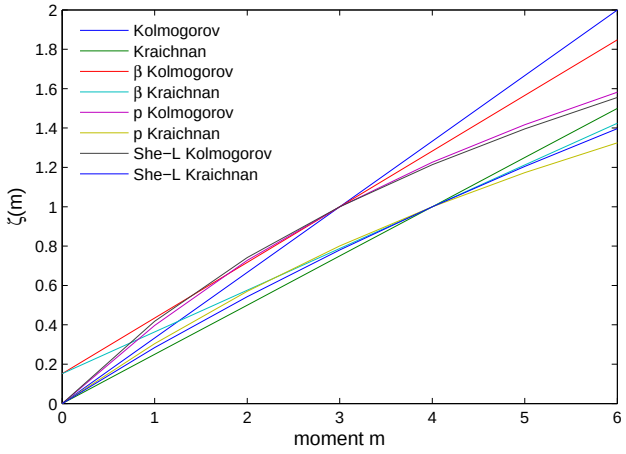

Figure 1-8: Dependence of $\zeta(m)$ on m for different turbulence models. The p model was computed using $p = 0.79$ and the β model with $\beta = 0.9$. These values were obtained by Horbury *et al.* (Horbury & Balogh, 1997), for Ulysses solar minimum polar data, however they are by no means universal. The values $\zeta(3) = 1$ for Kolmogorov-like models and $\zeta(4) = 1$ for Kraichnan-like models are clear, as is the divergence of the different models at higher m. However, experimentally the different models are difficult to distinguish.

1.4.7 Further Models and Simulations

For completeness, we briefly consider another important area of research, namely direct numerical simulations of MHD turbulence. These directly solve the time dependent incompressible and compressible MHD equations and enable investigation of the small scale phenomenology of turbulent fluctuations as well as the effects of eddy viscosity and resistivity (Biskamp & Müller, 2000). The principal drawback is that simulations are severely limited in the number of Fourier modes which they can encompass. This means that the Reynolds numbers reached are quite low and although periodic boundary conditions are used, finite size effects can also be a problem. It is therefore difficult to resolve and probe the inertial range of turbulence using MHD simulations.

Biskamp & Müller (2000) simulate freely decaying $3D$ turbulence and show that the inertial range scaling exponents are consistent with a modified She-Leveque model, with $\zeta(3) \sim 1$. Because of the limited inertial range available, analyses of simulations make extensive use of extended self-similarity (Benzi et al., 1993), which involves considering ratios of structure functions. This method has been shown to extend the inertial range, although the exact physical basis is unknown. The results of Biskamp & Müller (2000) were further developed by Merrifield et al. (2005).

Boldyrev (2005) also proposes a phenomenological model for the turbulent MHD cascade, which includes the effects of anisotropy. In the limit of a strong background field, their results show an IK like spectrum, whereas weaker anisotropy leads to a Goldreich-Sridhar type result. There is an extensive body of work on this model, see for example (Boldyrev, 2006; Mason et al., 2008). However in this thesis we are concerned only with data obtained from *in situ* spacecraft measurements rather than simulations. We note that the observed scaling behaviour provides empirical constraints for numerical models.

1.5 Spacecraft observations

1.5.1 The Ulysses Mission

The Ulysses spacecraft was a joint NASA/ESA mission (Marsden et al., 1996), launched in October 1990. Its primary mission was to study the heliosphere in three dimensions by journeying out of the ecliptic plane and over the solar poles. Ulysses is the first spacecraft to provide *in situ* measurements of solar particles and fields at essentially all solar latitudes (maximum latitude, $\sim 80°$). After its launch in 1990, a gravity-assist manoeuvre at Jupiter in 1992 sent Ulysses into the Sun-centered out of ecliptic orbit shown in Figure 1-9.

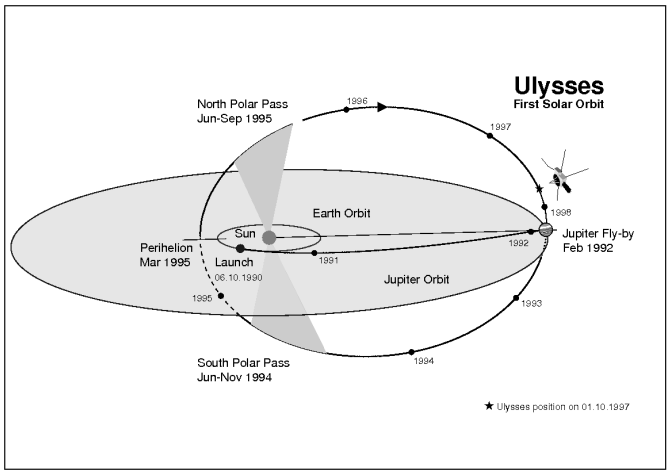

Figure 1-9: Ulysses orbit (plot courtesy of Ulysses online resources): $1990 - 1995$. South polar pass: from days 210 to 269, 1994. Ulysses moved from 2.6141 AU to 2.2014 AU and from an heliographic latitude of $-75.17°$ to $-79.60°$. North polar pass: from days 180 to 239, 1995. Ulysses moved from 1.7926 AU to 2.2043 AU and from an heliographic latitude of 73.76° to 77.03°.

At its closest approach to the Sun, during its fast latitude scan, Ulysses' perihelion distance is 1.3 AU. The aphelion of its orbit is at Jupiter at ~ 5.4 AU. Ulysses has a total orbital period of 6.2 years and has outlived its projected lifetime of 5 years by successfully completing two full orbits and three solar passes. Failing power supplies however meant that the final communication with Ulysses occurred on 30th June, 2009 after which its transmitter was shut down.
Ulysses has therefore made observations of the solar wind at periods of both maximum and minimum solar activity through a variety of different instruments, in-

cluding in particular the VHM/FGM magnetic field experiment (Balogh et al., 1992). The background magnetic fields at the locations of the Vector Helium Magnetometer (VHM) and the Fluxgate Magnetometer (FGM) onboard Ulysses were measured prior to lauch as 30 pT and 50 pT respectively, making Ulysses one of the magnetically cleanest space probes. The magnetometers themselves were shown to be intercalibrated to better than 0.1nT. In table 1-1, a summary of the magnetic field ranges and corresponding precision of these instruments is provided (data from Balogh et al. (1992)).

Table 1-1: Characteristics of the magnetic field experiment onboard Ulysses, comprising the VHM and FGM magnetometers. Data is from Table 2 in (Balogh et al., 1992)

Instrument	Ranges ($\pm$)	Resolution
VHM	8.192 nT	4.0 pT
	65.52 nT	32.0 pT
FGM	8.00 nT	3.9 pT
	64.0 nT	31.2 pT
	-2.048 μT	1.0 nT
	44.0 μT	21.5 nT

The analysis is this thesis will focus on the 60 second ($\sim$ lengthscale of 4.5×10^4 km) vector heliospheric magnetic field measurements, during intervals when Ulysses was above the Sun's North and South poles at heliospheric distances of $\sim 1.8 - 2.6$ AU and heliographic latitudes of $\sim 72 - 80°$. 1 second averaged ($\sim$ lengthscale of 750 km) Ulysses magnetic field data is also available, however we choose to use the 1 minute averaged data in order to remove any possible effects from Ulysses' spin, which has a period of 12 seconds.

1.5.2 The ACE Mission

The Advanced Composition Explorer or ACE (Stone et al., 1998), was launched in August 1998 and is in a Lissajous orbit around the L1 Lagrangian point between the Earth and the Sun. Its mission is to monitor the interplanetary medium and

its composition. ACE therefore provides continuous observations of solar wind particles and fields in the solar ecliptic plane at a fixed heliospheric distance ~ 1 AU. A plot of ACE's orbit is shown in Figure 1-10.

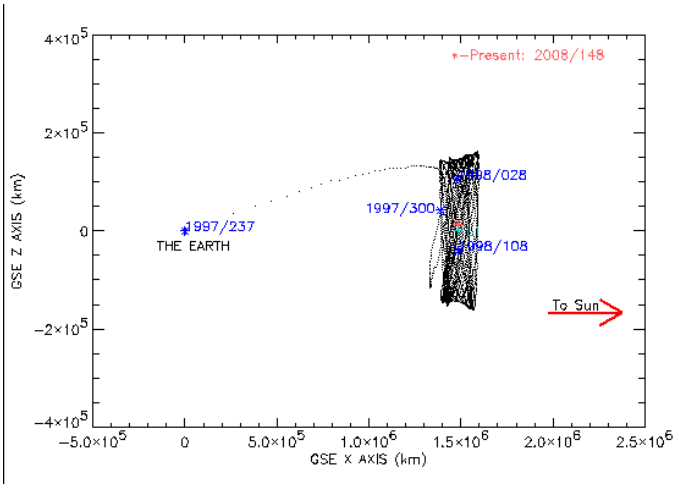

Figure 1-10: ACE orbit (plot courtesy of ACE online resources) from launch in 1998 to 2008. The Geocentric Solar Ecliptic (GSE) coordinate system is used (Hapgood, 1992), where X is the Earth-Sun line and Z is the ecliptic North pole.

In this thesis, the solar wind velocity field and density data from the Solar Wind Electron Proton Alpha Monitor (SWEPAM, (McComas et al., 1998a)) and the magnetic field data from the ACE Magnetic Field Experiment (MAG, (Smith et al., 1998)) are used. The data has a resolution of 64 seconds, which corresponds to lengthscales $\sim 4.8 \times 10^4$ km in the fast solar wind and $\sim 2.2 \times 10^4$ km in the slow solar wind. SWEPAM measures particle energies separately for ions (here protons and alphas) and electrons. The ion SWEPAM sensor can measure energies in the range $0.26 - 36$ keV/q (q is the ion charge), with a resolution of 5%, whereas the electron sensor measures energies in the range $1.6 - 1350$ keV with a resolution of 12%. The MAG experiment comprises 2 fluxgate magnetometers, which provide 3 component vector magnetic field measurements over 8 different dynamical ranges, described in Table 1-2 (data from (Smith et al., 1998)).

Table 1-2: Characteristics of the magnetic field experiment onboard ACE. Data is from Table 1 in (Smith et al., 1998)

Range number	Ranges (±)	Resolution
(0)	4 nT	0.001 nT
(1)	16 nT	0.004 nT
(2)	64 nT	0.016 nT
(3)	256 nT	0.0625 nT
(4)	1024 nT	0.25 nT
(5)	4096 nT	1.0 nT
(6)	16,384 nT	4.0 nT
(7)	65,536 nT	16.0 nT

1.5.3 Coordinates

The coordinate system used as the initial basis for the work in this thesis is the solar-ordered RTN system: R is the sun-spacecraft axis, T is the cross product of R with the solar rotation axis, and N is the cross product of R and T, completing the right-handed system. The Ulysses observations considered are taken when the spacecraft is sitting in fast uniform solar wind above the polar coronal holes with expanding open magnetic fieldlines. The RTN coordinate system is therefore appropriate, because we wish to consider turbulent fluctuations along and normal to the bulk flow direction, in this case the radial direction. In the ecliptic at ACE's orbit, the situation is different as the background magnetic field is twisted in the Parker spiral, and forms an angle of about $\sim 45^\circ$ with the Earth-Sun axis. The natural frame in which to study these fluctuations is then to project the RTN coordinates parallel and perpendicular to the background field. The average solar wind flow direction is however still radial, prompting a comparison of the two coordinate systems in Chapter 6.

1.5.4 The Taylor Hypothesis

The Taylor hypothesis allows us to convert spacecraft frequencies to spatial scales in the solar wind if the solar wind velocity is known. It relies on the solar wind speed being much larger than the local speed of the MHD waves, typically the Alfvén speed ($V_A \sim 51$ km s^{-1} at 1 AU, (Mullan & Smith, 2006)). The fluctuations can therefore be regarded as being "frozen in". As the spacecraft velocity is also considerably smaller than the solar wind velocity, a spacecraft time series can be considered as equivalent to a radial snapshot of the plasma flowing past it. Another way of expressing this is that the fluctuations on a particular scale need to be sampled at a much faster rate than their characteristic period. For example if waves of characteristic scale λ propagate at velocity v with respect to the plasma, which in turn propagates at speed v_{sw} with respect to the spacecraft, then these vary in a time $t_{sc} = \lambda/v_{sw}$ in the spacecraft frame (Horbury et al., 1996b). Now in the solar wind frame they vary in $t_p = \lambda/v$. It follows that $t_{sc} << t_p$ or equivalently $v_{sw} << v$ corresponds to our "frozen-in" assumption condition. If this is true we can now use the dispersion relation to relate the spacecraft frequency ω_{sc} to a solar wind plasma frame wavenumber k_p by $\omega_{sc} = v_{sw}k_p$ (valid only for Alfvén waves).

In practice the Taylor hypothesis is valid for most timelags in the solar wind (Bruno & Carbone, 2005; Osman & Horbury, 2009). Small *in situ* generated turbulent fluctuations are sampled at faster rates, whereas larger scale "frozen-in" structures ("$1/f$" region) are convected outwards from the Sun and do not evolve locally.

1.5.5 Stationarity

Another important consideration is the concept of statistical stationarity, since most timeseries analysis methods rely on some assumption of data stationarity. Strictly this means that, for a timeseries $y(t)$, none of the probability distributions or ensemble averaged properties of $y(t)$ depend on the origin in time (Matthaeus & Goldstein, 1982). In practice this is not always possible, instead the assumption of weak stationarity is used, where stationarity of the 2 point cor-

relation function is ensured if the mean and variance (i.e. the first two moments) of the data are themselves time-stationary.

Turbulent processes are stochastic, therefore their behaviour can therefore only be predicted with a degree of probability, and it is necessary then to consider ensemble averages of all possible realisations (Bruno & Carbone, 2005). A fully developed turbulent flow is very sensitive to small perturbations, however its average properties are not. Ideally, this would mean taking averages over an ensemble of turbulent flows (or realizations) prepared in near-identical conditions. This is however not possible in the solar wind, where instead the most common method used is time-averaging. For single point spacecraft data, we therefore consider the average behaviour of fluctuations $y(t+\tau)-y(t)$ over a timescale τ, which is linked to the lengthscale via the Taylor hypothesis. For this analysis to be valid, the timeseries must be weakly stationary: the overall pattern of fluctuations occuring at different times is not affected by the time evolution of the system, or in other words the turbulence is statistically stationary over time scales much larger than the time scale of the fluctuations. Matthaeus & Goldstein (1982) used short and long intervals of interplanetary magnetic field data to show that this assumption is satisfied for the interplanetary magnetic field. This is highly relevant to this thesis, where we will be dealing with both short $\sim$ 10 days and long $\geq$ 50 time periods. We have investigated the ACE and Ulysses datasets considered in Chapters 3 to 6 using the methods outlined in Matthaeus & Goldstein (1982) and we have found they can be considered weakly stationary.

1.5.6 Correlation

The solar wind also shows evidence of correlated structures and to briefly illustrate this, Figure 1-11 shows the autocorrelation functions $R(\tau) = \langle \delta B_i(t_1) \delta B_i(t_2) \rangle$, where $t_2 - t_1 = \tau$, $\delta B_i(t) = B_i(t) - \langle B_i(t) \rangle$ and i denotes the RTN magnetic field components. Fast uniform solar wind magnetic field measurements from the Ulysses spacecraft from a 10 day period, when Ulysses was at a heliospheric distance $\sim$ 2.4 AU, are used. We consider time lags τ up to $\sim$ 2500 minutes or about 1.7 days.

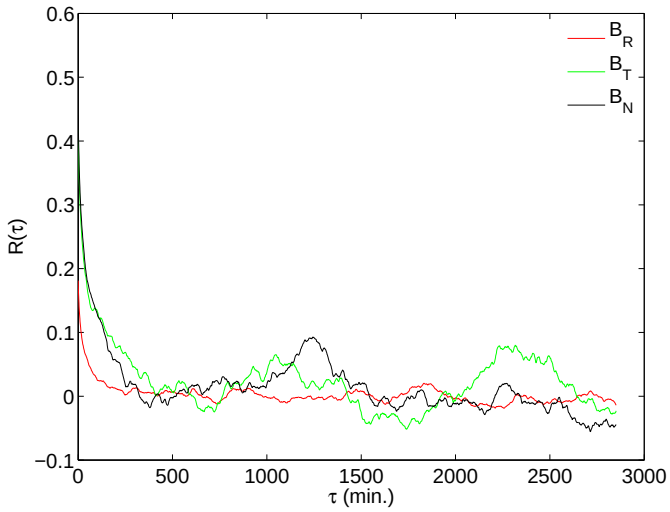

Figure 1-11: Autocorrelation functions $R(\tau)$ for the RTN magnetic field components for a representative 10 day interval of Ulysses data, days $210 - 220$ of the 1994 South polar pass.

We can estimate the correlation times for the different components from Figure 1-11, by fitting an exponential of the form $R(0)e^{(-\tau/\tau_c)}$ where τ_c is the correlation time and $R(0)$ is simply the variance of the process, to R_τ. We find $\tau_{c,R} = 44 \pm 2$ minutes, $\tau_{c,T} = 89.6 \pm 3.2$ minutes and $\tau_{c,N} = 74.3 \pm 2.3$ minutes, with 95% confidence bounds. We perform the same analysis in Figure 1-12 for similar length datasets of fast and slow solar wind magnetic field observations from the ACE spacecraft, positioned in the ecliptic plane at ~ 1 AU.

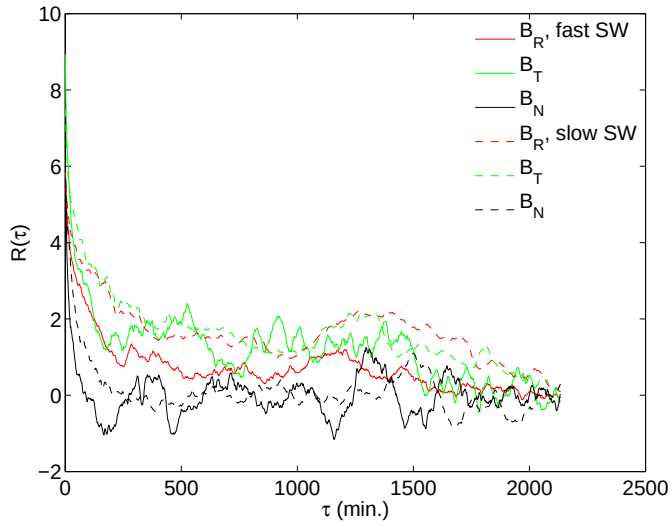

Figure 1-12: Autocorrelation functions $R(\tau)$ for the RTN magnetic field components for fast and slow intervals of ACE data at ~ 1 AU.

Figure 1-12 shows that the fast wind correlation function decreases much faster than the slow solar wind correlation, as also observed by (Bruno & Carbone, 2005). This is believed to be due to the fact that the fast solar wind has a bigger population of Alfvénic fluctuations, which are highly stochastic fluctuations, so that decorrelation occurs faster than in the slow solar wind. In all cases, the smallest timescales within the inertial range of solar wind turbulence are shorter than the correlation times, reflecting highly correlated structures at these scales.

1.5.7 Finite Size Considerations

Theoretical turbulence models (e.g. Kolmogorov) are constructed in the limit of infinite Reynolds number R_E and for spatially extended fully developed turbulence. However, physical timeseries are often bounded in space or in R_E. The solar wind has a large scale structure and therefore a finite R_E, which although $\gg 1$ ($\sim 10^5$ Matthaeus et al. (2005)), may still create finite size effects, which in turn will affect the observed scaling.

Grossmann et al. (1994) show numerically and analytically that deviations from Kolmogorov scaling of velocity moments decrease with increasing R_E for flows with $1.05 \times 10^4 \leq R_E \leq 1.4 \times 10^7$. They also point out that higher order moments are more sensitive to the finite size corrections than lower ones. This is further

corroborated by Arenas & Chorin (2006), who argue that higher order moments ($m > 3$) of non-Gaussian fields show scaling with a strong R_E dependence.
Another way of correcting for finite R_E effects is suggested in (Sreenivasan & Bershadskii, 2006, and references therein), and involves using logarithmic expansions. Structure function formed quantities such as flatness are shown to have a dependence on lnR_E rather than R_E.
Finally, in practice, both in numerical simulations (Merrifield et al., 2007) and in the laboratory (Dudson et al., 2005; Dendy & Chapman, 2006) the scaling of the moments $S_m \sim l^{\zeta(m)}$ is not always found or is not observed over a significantly large range. This may reflect the finite spatial domain, or in the case of a turbulent system and fluctutations, that the turbulence is not fully evolved. A weaker form of scaling, known as extended self-similarity (ESS) first observed by Benzi et al. (1993) may be applicable to such datasets. ESS proceeds by replacing l by an initially unknown generalized lengthscale $g(l)$, such that formally

$$S_m(l) \sim [g(l)]^{\zeta(m)} \tag{1-48}$$

It follows from equation 1-48 that

$$S_m(l) = [S_{m'}(l)]^{\zeta(m)/\zeta(m')} \tag{1-49}$$

(see for example Grossmann et al., 1997; Pagel & Balogh, 2001). This process has been seen to extend the range over which scaling is observed. The reason why this occurs is however still an open question in turbulence.

1.6 Experimental Applications

This thesis now presents a study of statistical methods to investigate non-linear phenomena in the solar wind over a range of different spatio-temporal scales and for different solar wind conditions.
In Chapter 2, the analysis techniques such as power spectral density (PSD), probability density functions (PDF), generalised structure functions (GSF) and extended self-similarity (ESS) are presented along with their application to three different model timeseries. The timeseries are chosen such that the expected scaling is known, however they also demonstrate different aspects of the solar wind

such as Gaussianity (Brownian walk), finite-size effects (Lévy flight) and intermittency (p-model). These methods are then applied to solar wind data in Chapters 3, 4, 5 and 6.

Chapters 3 and 4 explore inertial range turbulence using magnetic field measurements from the Ulysses spacecraft, which spent many months in the quiet fast solar wind above the Sun's polar coronal holes in a very simple coronal magnetic topology where both field and flow were highly ordered. It is known that solar wind acceleration and heating occurs over coronal holes. Ulysses is therefore ideally placed to sample the fast solar wind emanating from these holes. We quantify the scaling of the moments of the probability distribution function (PDF) of fluctuations of the well known inertial (high frequency) and $1/f$ (low frequency) ranges. GSF are used to show power law scaling in the "$1/f$" range of the form $\langle|y(t+\tau)-y(t)|^m\rangle \sim \tau^{\zeta(m)}$, but ESS was required to reveal scaling of the form $\langle|y(t+\tau)-y(t)|^m\rangle \sim [g(\tau)]^{\zeta(m)}$ over the inertial range. We find that $g(\tau)$ is independent of spacecraft position, which suggests that $g(\tau)$ is telling us about the macroscopic structure confining the turbulence. The scaling of the "$1/f$" region fluctuates with increasing radial range, consistent with a possible coronal origin. A good fit to the inertial range is $g(\tau) \sim \tau^{-log_{10}(\lambda_{log}\tau)}$. The exponents found here by ESS for the inertial range are fitted by a p-model and we find a higher degree of intermittency in the normal (N) and tangential (T) components of the magnetic field than in the radial (R) component. This provides quantitative constraints on models for fluctuations within the solar wind. This study is extended in Chapter 4, by constraining the form of the function $g(\tau)$ and by comparing the results from all of the Ulysses polar passes, in order to demonstrate universality. This is strong support for an *in situ* process independent of the solar driver in the inertial range.

In Chapters 5 and 6, we use ACE solar ecliptic measurements to explore the lower frequency temporal scales. The "$1/f$" energy range is of more direct coronal origin than the inertial range, and carries signatures of the complex magnetic field structure of the solar corona, and of footpoint stirring in the solar photosphere. We again quantify the scaling properties, focusing on solar cycle dependence and on anisotropy with respect to the background magnetic field. We present structure function analysis of magnetic and velocity field fluctuations, using a novel tech-

nique to decompose the fluctuations into directions parallel and perpendicular to the mean local background magnetic field. Whilst the magnetic field is close to "$1/f$", we show that the velocity field is "$1/f^{\alpha}$" with $\alpha \neq 1$. For the velocity, the value of α varies between parallel and perpendicular fluctuations and with the solar cycle. There is also variation in α with solar wind speed. We have examined the PDFs in the fast, quiet solar wind and intriguingly, whilst parallel and perpendicular are distinct, both the $\boldsymbol{B}$ field and velocity show the same PDF of their perpendicular fluctuations, which is close to gamma or inverse Gumbel. These results point to distinct physical processes in the corona, and to their mapping out into the solar wind. We compare our solar wind velocity and magnetic field fluctuations analysis in a frame ordered with respect to the background magnetic field to the same analysis in a frame ordered with the bulk velocity flow.

Chapter 2

Model results

2.1 Introduction

In order to demonstrate the statistical analysis methods, which we will apply to the solar wind parameters in Chapters 3 and 4, we first apply them to three model timeseries.

The first two processes, which we will examine, are the Brownian walk and a stable Lévy process. These are both examples of critical phenomena, or processes, which are defined by structures on many scales and power law behaviour of characteristic quantities (p40 Sornette, 2004). Renormalisation Group (RG) analysis explores mathematically the concept that the macroscopic behaviour of an observable is the result of the sum of arbitrary processes at a microscopic level. A timeseries can then be decimated on different scales, but the observed probability density functions (PDFs) at each scale will be the same, provided they are correctly rescaled. This approach works well for self-similar systems.

The simplest case is the Brownian walk, which is ubiquitous in nature and is described by Gaussian statistics. Stable Lévy flights, which have heavy-tailed distributions of step length, can be thought of as generalisations of a Brownian walk. A process is stable if, when we sum N *i.i.d.* (independent and identically distributed) random variables x which have the same PDF $P_1(x)$, we obtain a random variable $X = \sum x$ with PDF $P_N(X)$ of the same form as $P_1(x)$. As $N \to \infty$, the central limit theorem (Sornette, 2004) tells us that *the sum, normalised by* $1/\sqrt{N}$*, of* N *random independent and identically distributed variables of zero mean and finite variance* σ^2*, is a random variable with a PDF converging to the Gaussian distribution with variance* σ^2. A generalised version of CLT allows us to define a Lévy distribution of index $\beta < 2$ as the sum of all *i.i.d.* random variables with no finite variance and distributions with power law tails

($\propto \delta x^{-1-\beta},\ \beta \in (0,2]$). This indicates that the Gaussian or Brownian and Lévy distributions ($\beta < 2$) are stable. We can also note that random walks themselves are not stationary, however their increments are statistically stationary.

The third process which we will consider is the p-model, introduced in Chapter 1. This model allows the generation of a multifractal and therefore intermittent timeseries and has been used extensively to model solar wind turbulence (e.g. Horbury & Balogh, 1997). It should be stressed that these models are distinct from phenomenological models, such as She-Leveque and Goldreich-Sridhar theories, which attempt to describe the physics of the solar wind by considering different types of structures (e.g. filamentary and/or sheet-like) or the effects of anisotropy. Nevertheless the analysis methods, which we apply, are universal statistical timeseries tools and it is useful to consider their application to well-known processes, which still display some of the properties observed in the solar wind, such as Gaussian statistics (e.g. Burlaga et al., 1989), non-Gaussian statistics (Marsch & Tu, 1997) and intermittency (see for example Burlaga, 1991; Marsch & Tu, 1997; Bruno et al., 2007).

The analysis methods and tools of power spectral density (PSD), probability density function (PDF) rescaling and generalised structure functions (GSF), and the scaling information which they provide, are described before being applied to the different models. The problem of finite size datasets and the bias this can cause on the systems statistics is also addressed by applying a novel conditioning technique developed by Kiyani et al. (2006). Other sources of error, which we minimise, lie with "noisy" PSD and the problem of fitting to finite range power laws, i.e. over a finite range of scales. We use a windowing and averaging procedure to reduce the PSD errors and we include in our scaling error analysis the variations in scaling values when fitting the GSFs over ranges (of scales) of increasing length. Finally, there are other analysis methods such as rescaled-range analysis (Hurst et al., 1965), which is described in the conclusions.

2.2 Model Timeseries

2.2.1 Brownian Walk

Brownian motion is named after the British botanist and surgeon Robert Brown, who first described the random movements of pollen grains immersed in a fluid observed under a microscope (1827). Generally, it now signifies a mathematical model (Sornette, 2004, p25), used to describe a certain type of continuous (in time) stochastic process. Physical examples include the motion of particles suspended in a fluid (famously studied by Einstein (1905)) and stockmarket fluctuations. Brownian motion is one of the simplest random motion models: if we consider the motion of a particle suspended in a fluid at time t_0 and position $\boldsymbol{x}(t)$, it will make a random displacement $\delta\boldsymbol{x}(t,\tau)$ in time τ to position $\boldsymbol{x}(t+\tau) = \boldsymbol{x}(t) + \delta\boldsymbol{x}(t,\tau)$ at time $t_0 + \tau$. The distribution of the "steps" $\delta\boldsymbol{x}(t,\tau)$ is found to be Gaussian and independent of its position coordinates. Brownian motion can then be summarised by three intrinsic properties

- The steps $\delta\boldsymbol{x}(t,\tau) = \boldsymbol{x}(t+\tau) - \boldsymbol{x}(t)$, $t \geq t_0$ have a Gaussian distribution and are independent identically distributed (*i.i.d.*) variables
- The step $\delta\boldsymbol{x}(t_n,\tau) = \boldsymbol{x}(t_n+\tau) - \boldsymbol{x}(t_n)$ is independent of previous steps $t_0 < t_1 < t_2 < \cdots < t_n$.
- The mean step is zero, $< \delta\boldsymbol{x}(t,\tau) >= 0$

Figure 2-1 shows a one dimensional Brownian walk constructed from 1×10^6 steps taken from a normal distribution.

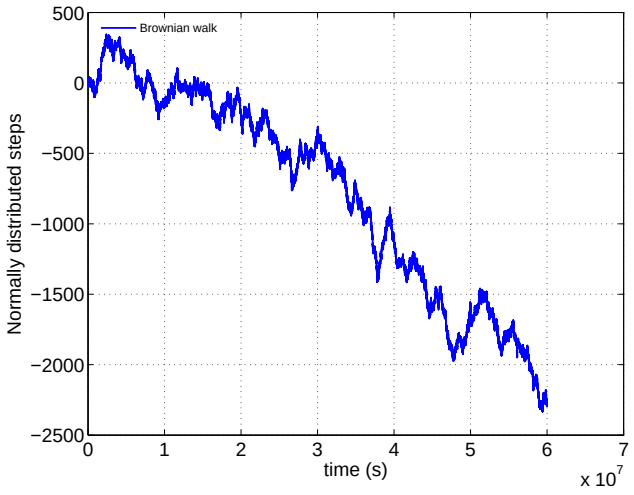

Figure 2-1: Brownian walk constructed from 1×10^6 normally distributed steps over $[-1:1]$.

Consider further the simple random walk shown in Figure 2-1. Taking $t_0 = 0$ and $x(t_0) = 0$, the position at time t_n is given by (Sornette, 2004, p24)

$$x(t_n) = \sum_{i=1}^{i=n} \delta x(t_i, \tau) \tag{2-1}$$

If we take $< x(t_n) >$ as the average position at time t_n over a large assembly of walks, we obtain from equation 2-1

$$< x(t_n) >= \sum_{i=1}^{i=n} < \delta x(t, \tau) >= n < \delta x(\tau) > \tag{2-2}$$

We can now define the velocity of this average total displacement $< x(t_n) >$

$$v = \frac{< x(t_n) >}{t_n} = \frac{n < \delta x >}{n\tau} = \frac{< \delta x >}{\tau} \tag{2-3}$$

The typical extent of the random walk around its mean position vt is therefore given by the variance $< x(t_n)^2 > - < x(t_n) >^2$

$$\begin{aligned} < x(t_n)^2 > - < x(t_n) >^2 &= \sum_{i=1}^{i=n} \sum_{j=1}^{i=n} (< \delta x(t_i)\delta x(t_j) > - < \delta x(t_i) >< \delta x(t_j) >) \\ &= \sum_{i=1}^{i=n} \sum_{j=1}^{i=n} C_{ij} \end{aligned} \tag{2-4}$$

where $C_{ij} =< \delta x(t_i)\delta x(t_j) > - < \delta x(t_i) >< \delta x(t_j) >$ is the correlation function of the steps $\delta x(t_i)$ and $\delta x(t_j)$. One of our assumptions is that these steps are

uncorrelated, therefore we can write C_{ij} as

$$C_{ij} = \left[< \delta x^2 > - < \delta x >^2 \right] \delta_{ij} \tag{2-5}$$

which can be substituted into equation 2-4 to yield

$$< x(t_n)^2 > - < x(t_n) >^2 = n \left[< \delta x^2 > - < \delta x >^2 \right] \equiv n\sigma_{\delta x}^2 \tag{2-6}$$

where $\sigma_{\delta x}^2 = < \delta x^2 > - < \delta x >^2$ is the variance of the probability density function of the δx variables. If we define the diffusion coefficent $D = \frac{\sigma_{\delta x}^2}{2\tau}$ and recall that $n = \frac{t}{\tau}$, we obtain the diffusion law relating the variance of the sum of n *i.i.d.* variables to the individual step variance:

$$< x(t_n)^2 > - < x(t_n) >^2 = 2Dt \tag{2-7}$$

Equation 2-7 can be generalised to d dimensions by applying the rule of additivity of the variance of each projection of the random walk position over each direction. Finally, the Brownian walk exhibits the property of self-affinity or fractality, which means sub-sections of the system are statistically similar to the whole system under a suitable mathematical transformation (see definition of fractal dimension in Chapter 1). For our $d_T = 1$ Brownian walk in Figure 2-1, where d_T is the topological dimension, we can estimate the total length L of the walk unfolded as approximately

$$L \sim \sqrt{\sigma_x^2 + t^2} \sim t\sqrt{1 + \left(\frac{\sigma_x}{t}\right)^2} \tag{2-8}$$

For small τ scales, $(\sigma_x/t)^2$ is much larger than one, as we know from equation 2-6 that as $n = t/\tau$, $\sigma_x \propto 1/\tau$. Therefore equation 2-8 becomes

$$L \sim t\sqrt{\left(\frac{\sigma_x}{t}\right)^2} \sim t^{\frac{1}{2}} \tag{2-9}$$

We can think of t as the resolution ϵ in equation 1-1, which leads to

$$d_f = d - \frac{1}{2} = \frac{3}{2} \tag{2-10}$$

A large scales however, the converse is true and we find $L \sim t$ and therefore $d_f = 1$. If we generalise our Brownian walk to d, $d_t \geq 2$ dimensions, $\sqrt{\sigma_x}$ is a representative diameter estimate and $\sqrt{\sigma_{\delta x}}$ is a natural resolution scale, we have

$$n = \left(\frac{\sigma_x}{\sigma_{\delta x}}\right)^{d_f} \tag{2-11}$$

From 2-6 the fractal dimension d_f of a Brownian walk in $d \geq 2$ is 2.
Another quantity of interest, often used in fractal analysis, is the Hurst exponent H. For walks based on *i.i.d.* steps in a space of embedding dimension d, H is directly related to the fractal dimension d_f such that

$$d_f = d - H \tag{2-12}$$

The Hurst exponent helps to quantify the predictability of a time series and is generally used in the analysis of financial timeseries, to identify trends (see for example Sánchez Granero et al., 2008, and references therein). It measures the relative tendency of a time series to either regress to a longer term mean value or "cluster" in a given direction. From equation 2-12, a Hurst exponent close to 0.5 implies Brownian walk behaviour, whereas $0 < H < 0.5$ is a sign of anti-persistent behaviour and $0.5 < H < 1$ of persistent (data shows trends) behaviour. There are different methods of estimating the Hurst parameter, such as generalised structure functions, which will be examined later.
Although many natural systems exhibit Brownian walk characteristics, there are other types of stochastic processes. We will introduce two further types of time-series, the Lévy flight and the p-model which respectively demonstrate the effects of extreme events and multifractality (a single fractal dimension is no longer sufficient to describe the system's dynamics).

2.2.2 Lévy Flight

Lévy flights are named after the french mathematician Paul Lévy $(1886 - 1971)$ and are a class of random walks where the step size δx is taken from a probability distribution $P(\delta x)$, which has power law tails

$$P(\delta x) \propto \delta x^{-1-\beta} \tag{2-13}$$

We see from equation 2-13 that a process with such scaling has no variance (the integral $\int_0^\infty \delta x^2 P(\delta x) d(\delta x)$ does not converge/exist) for $0 < \beta < 2$ and when $0 < \beta \leq 1$ it has no mean $(= \int_0^\infty \delta x P(\delta x) d(\delta x))$ defined either. For $\beta \geq 2$, we recover processes with finite variance and mean such as the Brownian walk. The following algorithm (Siegert & Friedrich, 2001) is used here to generate the Lévy

flight steps or increments:

$$\delta x = \frac{sin(\beta r)}{(cos(r))^{\frac{1}{\beta}}} \left(\frac{cos[(1-\beta)r]}{\gamma} \right)^{\frac{(1-\beta)}{\beta}} \tag{2-14}$$

where r is a uniformly distributed random variable in the range $[-\pi/2, \pi/2]$ and γ is an exponentially distributed random variable with mean 1, which is independent of r. β is set equal to 1. Figure 2-2 shows a 1×10^6 step Lévy flight generated using 2-14.

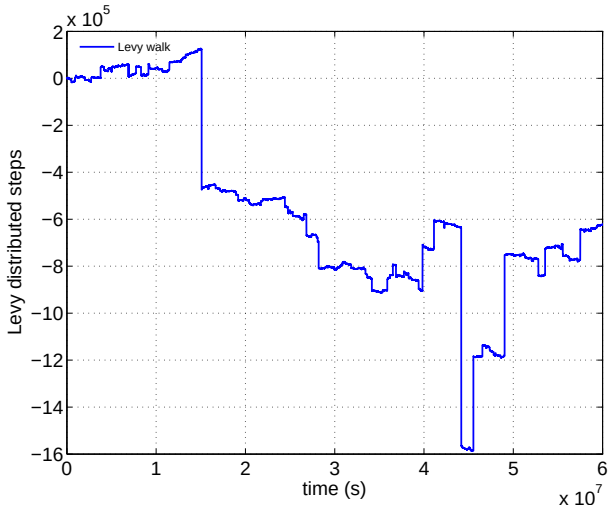

Figure 2-2: Lévy walk with $\beta = 1$ constructed from 1×10^6 Lévy distributed steps

As we can see in Figure 2-2, a Lévy walk is dominated by occasional large jumps, this type of behaviour is observed in many real-life systems such as some financial markets (p162 Wolfgang & Baschnagel, 1999), photon diffusion in hot atomic vapours (Mercadier et al., 2009) and more generally anything dominated by extreme events at large times. These large events or outliers can lead to anomalous behaviour when calculating the system's statistics as in practice we are dealing with finite length timeseries with a defined mean and variance, and therefore a finite sample size saturation is observed. A method of addressing this problem, while still preserving the underlying statistics of the system, is introduced later. Finally we can note that the β exponent, characteristic of the Lévy flight, is related to the Hurst exponent via $H = \frac{1}{\beta}$. This will also be dicussed later when we show the functional form of the Lévy flight probability density function.

2.2.3 p-Model

We now introduce a multifractal timeseries, namely the p-model, already described in Chapter 1, section 1.4.4. In Figure 2-3 we show a p-model for $p = 0.6$ (data courtesy of K. Kiyani).

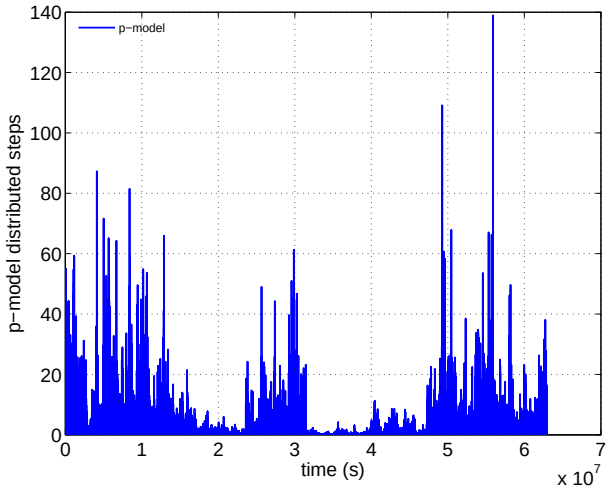

Figure 2-3: p-model constructed from 1.05×10^6 p-model generated steps

As we can see from Figure 2-3, the p-model is indeed highly intermittent or "bursty", which is what makes it an attractive model for anisotropic MHD turbulence in the solar wind. Recall also that the p-model is multifractal, i.e. a single fractal dimension is not sufficient to quantify the system's dynamics at every point (Bohr et al., 1998, p34 and references therein).
We now consider different practical methods of extracting the scaling information from these timeseries.

2.3 Power Spectral Density

2.3.1 Introduction

The power spectral density of a process is a positive real function dependent on frequency and associated with a stationary stochastic signal or deterministic function of time. The spectral density is often used to identify periodicities in a signal. If $f(t)$ is a finite-energy signal (or square integrable, which means that

the integral of the square of its absolute value, over the interval considered, is finite), the spectral density $F(w)$ of the signal is the square of the magnitude of the continuous Fourier transform of the signal

$$F(w) = |\frac{1}{\sqrt{2\pi}} \int_{-\infty}^{\infty} f(t) e^{-i\omega t} dt|^2 \tag{2-15}$$

where ω is the angular frequency ($\omega = 2\pi f$). It is also possible to define a discrete Fourier transform for the case when the signal is discrete with values f_n over an infinite number of elements:

$$F(\omega) = |\frac{1}{\sqrt{2\pi}} \sum_{n=-\infty}^{\infty} f_n e^{-i\omega n}|^2 \tag{2-16}$$

In order to build a meaningful spectral representation for a stochastic process, we need to consider the spectral representation theorem (p127 Percival, 1993). Stationary processes have constant variance over time and unless we are dealing with a harmonic process, they are also generally not periodic, which means we cannot define their spectral properties over a subrange of frequencies. We quote here the spectral representation theorem for a stationary, continuous parameter, continuously stochastic and real-valued process $X(t)$ with zero mean (p134 Percival, 1993)

$$X(t) = \int_{-\infty}^{\infty} e^{i2\pi ft} dZ(f) \tag{2-17}$$

where $Z(f)$ has specific properties defined in (p135 Percival, 1993). For weakly stationary random processes the following relationship can be derived between the spectral density function $F(w)$ and the autocorrelation function $R(\tau)$:

$$F(w) = \int_{-\infty}^{\infty} R(\tau) e^{-i\omega\tau} d\tau \tag{2-18}$$

Equation 2-18 is also known as the Wiener-Kinchin formula and states that the power spectral density is the Fourier transform of the corresponding autocorrelation function. The power spectral scaling exponent α can be expressed as $\alpha = \zeta(2) + 1$ for the power spectrum $F(\omega) \sim \omega^{-\alpha}$ of a non-stationary function comprised of stationary *i.i.d.* increments, see for example Frisch (p54 1995). For a fractal process we have the result that $\alpha = 2H + 1$. We now consider the power spectra of our model timeseries defined previously.

2.3.2 FFT Method

A fast Fourier transform (FFT) technique is applied to the data, where each timeseries is split up into windows of $2^{12} = 4096$ points with a 50% overlap on the previous window. A Hanning window is applied to each of these sub-intervals and the FFT is computed. An average is then taken of these FFTs to obtain the power spectrum for each dataset.

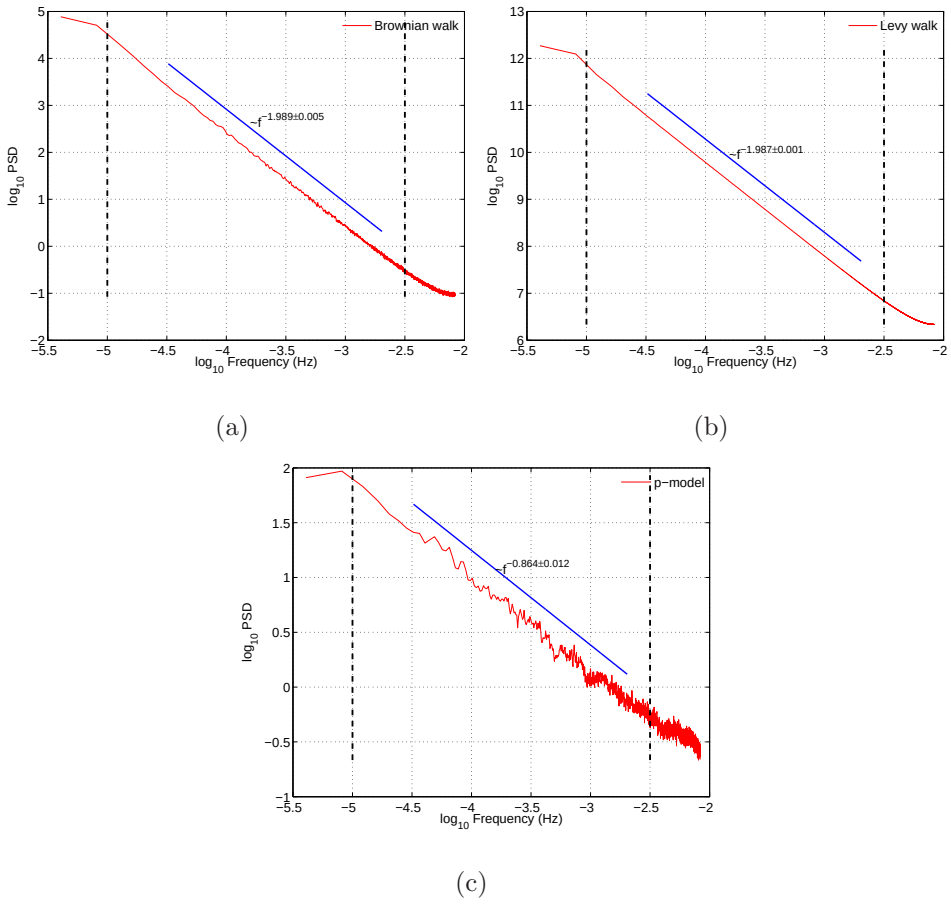

Figure 2-4: The PSDs for the Brownian walk, Lévy flight and p-model timeseries defined previously. The PSD have an $f^{-\alpha}$ power law behaviour where α is the power spectral exponent. The PSDs are all fitted using linear regression between the frequencies 3.255×10^{-5} Hz to 2×10^{-3} Hz and the following values of α obtained: Brownian walk, $\alpha = 1.989 \pm 0.005$; Lévy flight, $\alpha = 1.987 \pm 0.001$ and p-model, $\alpha = 0.864 \pm 0.012$.

Using $\alpha = \zeta(2) + 1$, the PSD analysis allows us to estimate H for the Brownian walk and the Lévy flight. We obtain $H = 0.495 \pm 0.003$ for the Brownian walk case and $H = 0.494 \pm 0.001$ for the Lévy flight. The result for the Brownian walk is what we would expect from our previous analysis, however the Lévy flight H

exponent is approximately only half what we would expect, this is due to finite data size effects, which we shall investigate further on. It should also be noted that PSD analysis only gives information on the second order scaling exponent. For information on higher order scaling exponents, other analysis methods are necessary.

2.4 Probability Density Function

2.4.1 PDF Collapse

As mentioned previously the fluctuations in a stochastic process $x(t)$ can be characterised on different time scales τ by considering differences $\delta x(t, \tau)$ over a timescale τ (e.g. Chapman et al., 2005a). The probability density functions or PDFs, $P(y, \tau)$, of these increments for the different τ can be displayed and tested for self-similar behaviour.

First it will be assumed that the $\delta x(n, \tau)$ satisfy the following general scaling relationship:

$$\delta x(b\tau) \equiv f(b)\delta x(\tau) \tag{2-19}$$

where b is some scaling factor, $\equiv$ denotes an equality in the statistical or distribution sense and f is some scaling function. Statistical stationarity in the δx increments is also assumed. As is that b and $f(b)$ are both positive and that (2-19) can be interpreted as a generalised form of self-affinity. From (2-19) the following scaling transformations can be derived:

$$\tau' = b\tau, \quad \delta x' = f(b)\delta x, \tag{2-20}$$

where the primed variables are scaled quantities. The conservation of probability under change of variables relates the PDFs of δx and $\delta x'$ by:

$$P(\delta x, \tau) = P'(\delta x', \tau')\frac{|d(\delta x')|}{|d(\delta x)|} \tag{2-21}$$

where $P(\delta x, \tau)$ is the PDF associated to δx and $P'(\delta x', \tau')$, the one associated to $\delta x'$. Using the transformations defined in (2-20), (2-21) can then be expressed as:

$$P(\delta x, \tau) = f(b)P'(f(b)\delta x, \tau') \tag{2-22}$$

This implies that the given stochastic process, here $\delta x(t)$, is statistically self-similar. In other words a process on scale τ' (and $\delta x'$) can be mapped onto another process on a different scale τ (and δx) via the scaling transformations given by (2-20) Kiyani et al. (2006). The PDFs of both these processes are then related by (2-22).

As b is an arbitrary variable, we can thereby simplify things further by choosing $b = \tau^{-1}$, which gives us:

$$P(\delta x, \tau) = f(\tau^{-1})P'(f(\tau^{-1})\delta x, 1) = f(\tau^{-1})P_s(f(\tau^{-1})\delta x) \tag{2-23}$$

This is equivalent to saying that any PDF P of increments δx characterised by an interval τ can be collapsed onto a single unique PDF P_s of rescaled increments $f(\tau^{-1}\delta x)$ and interval $\tau = 1$ by the above scaling relation. For self-affine scaling, the scaling function f takes the form of a power law, $f(b) = b^h = \tau^{-H}$. H is again the Hurst exponent. Equation (2-23) now becomes:

$$P(\delta x, \tau) = \tau^{-H} P_s(\tau^{-H}\delta x) \tag{2-24}$$

This method of PDF collapse requires knowledge of the Hurst exponent, as we have seen PSDs are not always a reliable method of estimating H, we will investigate another method to obtain H, namely generalised structure functions in the next section.

However another equivalent method of renormalization is possible using the mean and standard deviation of the data. We will attempt a scaling collapse on the different models' fluctuations PDFs using this method initially. The PDFs are renormalized using (e. g. Greenhough et al., 2002a)

$$P[(x - < x >)] = \sigma^{-1} P[\sigma^{-1}(x - < x >)] \tag{2-25}$$

where $< \cdots >$ denotes the ensemble mean and σ is the standard deviation of the distribution. For a self-affine process, knowledge of the functional form of the PDF, and of the Hurst exponent H, is sufficient in principle to build a stochastic differential equation model for the process (e. g. Chapman et al., 2005a; Kiyani et al., 2007). Figure 2-5 shows the PDF for the increments of the Brownian walk shown in Figure 2-1, the collapsed PDF using equation 2-25 is also shown. The time-series is differenced over $\tau = 1 + 30n$ for $n = 0$ to $n = 16$, i.e. $\tau = 1$ to $\tau = 481$.

The PDFs of the increments of a Brownian walk theoretically have a Gaussian distribution given by

$$P_B(\delta x, \tau) = \frac{1}{\sigma\sqrt{2\pi}} e^{\frac{-(\delta x-\mu)^2}{2\sigma^2}} \tag{2-26}$$

where μ is the mean of the data and σ is the standard deviation.

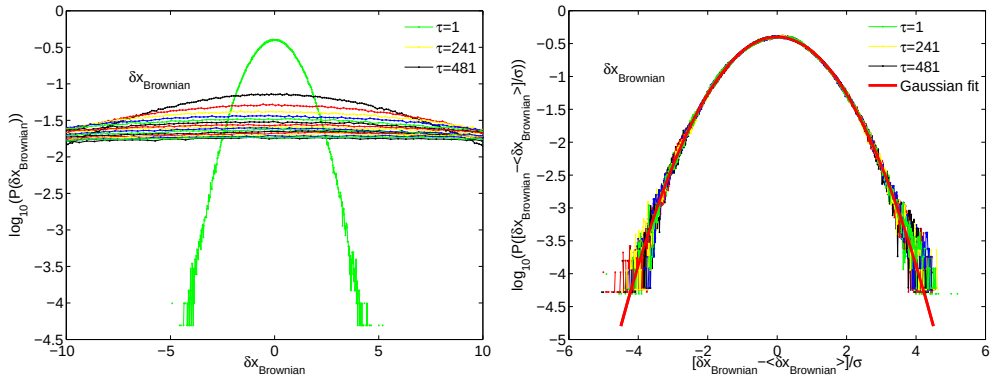

(a) (b)

Figure 2-5: The PDFs for the steps of the Brownian walk (Figure 2-1) for $\tau = 1$ to $\tau = 481$ in steps of 30. The right hand panel shows the PDFs renormalised by their mean and standard deviation. For clarity the legend only shows τ_{min}, τ_{max} and an intermediate τ.

Figure 2-5 clearly shows the Gaussian nature of the Brownian walk increments, the fit parameters for the Gaussian fit (equation 2-26) of the collapsed curves are $\mu = 0$ and $\sigma = 1$, consisent with the renormalisation process. The PDFs collapse onto a single curve confirming the self-similar nature of the process. We can further confirm the normal nature of the statistical flucutuations graphically by using a normal probability plot. On such a plot, shown in 2-6, the empirical probability is plotted versus the data value for each point in the data. The fluctuations will appear as a straight line if they are from a normal distribution, other distributions introduce curvature.

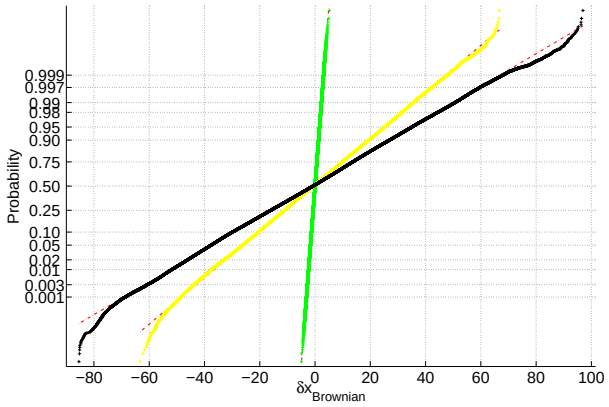

Figure 2-6: Normal probability plot for the steps of the Brownian walk (Figure 2-1) for $\tau_{min} = 1$ (green), $\tau_{min} = 281$ (yellow) and $\tau_{max} = 481$ (black). Between the 25th and 75th percentiles, the datapoints are connected and this line is then extended to the full plotted range (dashed red line).

In Figures 2-7 and 2-8 we repeat this procedure for the Lévy walk (Figure 2-2) and the p-model (Figure 2-3).

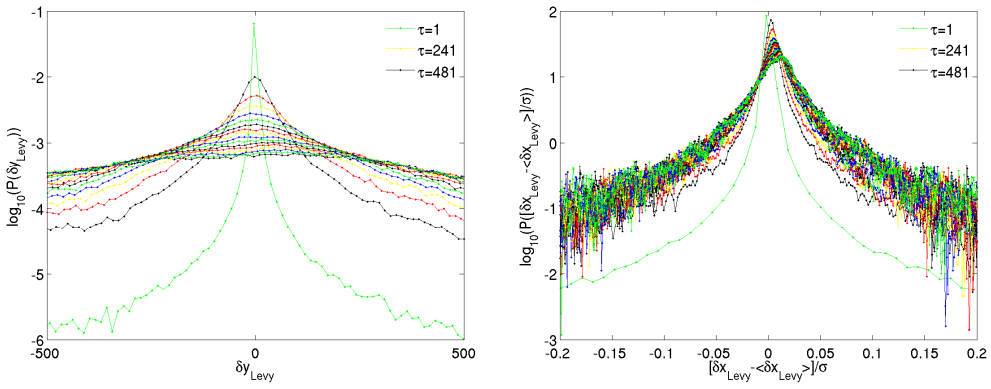

(a) (b)

Figure 2-7: The PDFs for the steps of the Lévy flight (Figure 2-2) for $\tau = 1$ to $\tau = 481$ in steps of 30. The right hand panel shows the PDFs renormalised by their mean and standard deviation. For clarity the legend only shows τ_{min}, τ_{max} and an intermediate τ.

Figure 2-7 shows that this method of rescaling does not work for the Lévy flight, even though it is a mono-fractal process. This is because, as we mentioned previously, a Lévy flight has infinite variance for $0 < \beta < 2$ so the renormalisation using the mean and standard deviation of the data cannot be correct. As we

are dealing with a finite dataset, these quantities exist but will be governed by the large outliers in the PDF and cannot give any meaningful statistical information. Theoretically the Lévy flight PDF is defined by the Fourier transform of its characteristic function

$$P_L(\delta x, \tau) = \frac{1}{2\pi} \int_{-\infty}^{\infty} e^{ik\delta x} e^{-\gamma\tau|k|^\beta} dk \tag{2-27}$$

where $\gamma \geq 0$ and $\tau \geq 0$ are the characteristic scales of the process, for simplicity we consider $\gamma = 1$. From equation 2-27, the scaling properties of $P_L(\delta x, \tau)$ are

$$P_L(\delta x, \tau) = \tau^{-\frac{1}{\beta}} P_L(\tau^{-\frac{1}{\beta}} \delta x, 1) \tag{2-28}$$

By identification with equation 2-24, this gives the previously mentioned result $H = 1/\beta$.

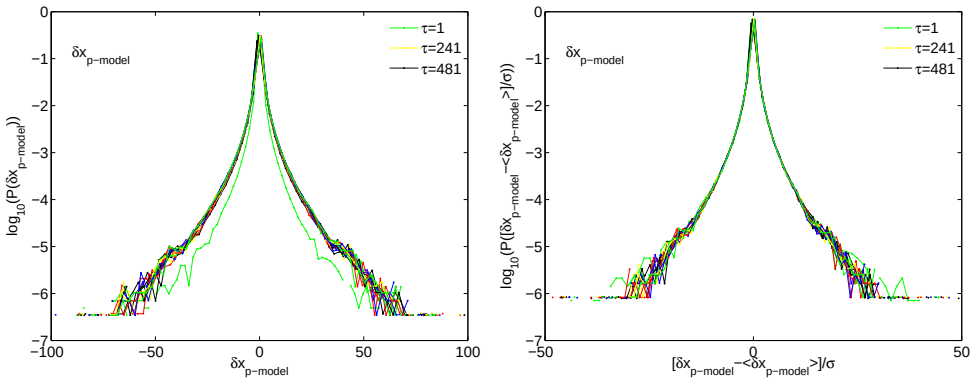

(a) (b)

Figure 2-8: The PDFs for the steps of the p-model (Figure 2-3) for $\tau = 1$ to $\tau = 481$ in steps of 30. The right hand panel shows the PDFs renormalised by their mean and standard deviation. For clarity the legend only shows τ_{min}, τ_{max} and an intermediate τ.

The p-model PDF in Figure 2-8 is again heavy tailed, showing the presence of large steps in the timeseries. However for the peak region of the PDF, the collapsing process works relatively well. We can further extend our PDF analysis by using GSFs to define the Hurst or ζ exponents of these models and retest the PDF collapse defined in equation 2-24.

2.5 Generalised Structure Function

2.5.1 Introduction

Scaling can be quantified by computing the generalized structure functions (GSFs) of the fluctuations, $\langle \mid \delta x \mid^m \rangle$, where $\langle \cdots \rangle$ again denotes ensemble averaging. Assuming weak stationarity, GSFs are related to the scale τ of the fluctuation by a scaling $S_m = \langle \mid \delta x_\tau \mid^m \rangle \sim \tau^{\zeta(m)}$. In principle, the scaling exponents $\zeta(m)$ are obtained from the gradients of the loglog plots of S_m versus τ. In practice, these are affected by the fact that both the length of the dataset, and the range of τ over which we see scaling, are finite. We now outline a method to optimise this process to obtain a good estimate of the exponents. Let us begin by discussing a simple self-affine process, the Brownian walk, where $S_m \sim \tau^{\zeta(m)}$, $\zeta(m) = Hm$. For a robustly self-similar process, any point on the PDF will scale as τ^{-H} (self-affine property), so that in principle one can use any subset of the PDF to obtain H. We seek to choose the most statistically significant subset, and we do this by recomputing H for different regions of the PDF, if the process is fractal, we expect to find the same H. To probe the full range of behaviour in the PDF and the tails we need to test for convergence to a single value of H for a wide dynamic range of the PDF, for example $\sim 20\sigma$. A fractal (self-affine) timeseries will in principle always give the same value of H if computed from any point, or range of values, of the PDF. The largest values explored by the PDF of the data are the least well sampled statistically. It follows that if we successively remove these outliers we should see, for a fractal timeseries, rapid convergence to a constant H value.

We test this for the Brownian walk, Lévy flight and p-model by computing the $\zeta(m)$ from the GSFs and then plotting a representative value $\zeta(2)$ as a function of the percentage of removed points. This is shown in Figure 2-9 for a Brownian walk, see also Kiyani et al. (2007). The errors are obtained by combining the least squares error in the $\zeta(m)$ value fitted across the full range, with the standard deviation of the $\zeta(m)$ values fitted across varying lengths of points, the latter starting with a minimum length of about half the total fitting range length, centered on the middle of the full fitting range. This method is applied for all the exponent statistics throughout this Chapter. This allows us to test the robustness of our

chosen scaling range by examining the variation of the $\zeta(m)$ exponents as a function of the fitting range. This is shown in Figure 2-9 for a Brownian walk, see also Kiyani et al. (2007).

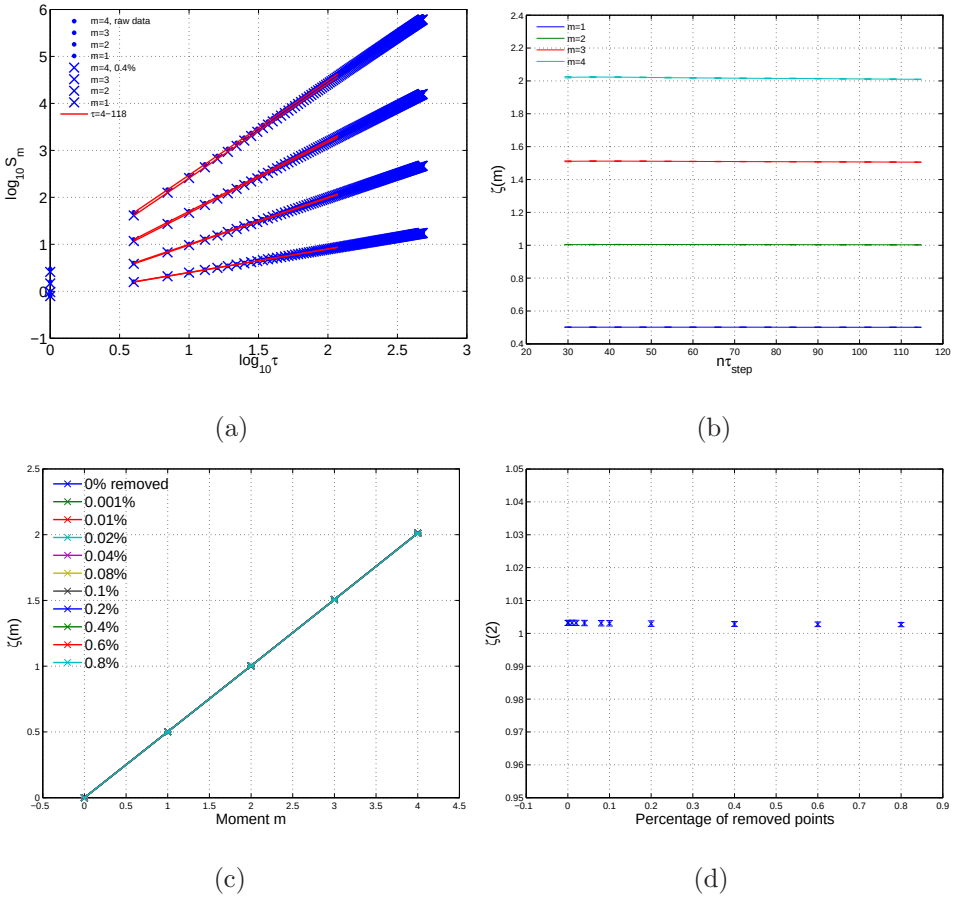

Figure 2-9: The top left panel shows the GSFs for the Brownian walk computed for $\tau = 1$ to $\tau = 481$ in steps of 3 for both raw (".") and 0.4% conditioned data ("×") fitted to $\tau = 4$ to $\tau = 118$ (red lines). The top right panel shows how the fitting range is tested by fitting between $\tau = 46$ to 76 and then increasing the fitting range on either side to the next consecutive τ, up to $\tau = 4$ to $\tau = 118$. The bottom panels show the scaling exponents $\zeta(m)$ plotted as a function of moment $m = 1$ to 6 for different percentages of removed points (left panel) and $\zeta(2)$ plotted against the percentage of removed points (right panel).

The scaling for a Brownian walk with normally distributed steps demonstrates the expected behaviour for a fractal process without heavy tails (2-9). We can quantify the observed scaling by $\zeta(2) = 1.001 \pm 0.001$, which gives a Hurst exponent of 0.501 ± 0.001. Within errors this is the same as the theoretical $H = 0.5$ value. The analysis is repeated for the Lévy flight and the p-model in Figures 2-10 and 2-12.

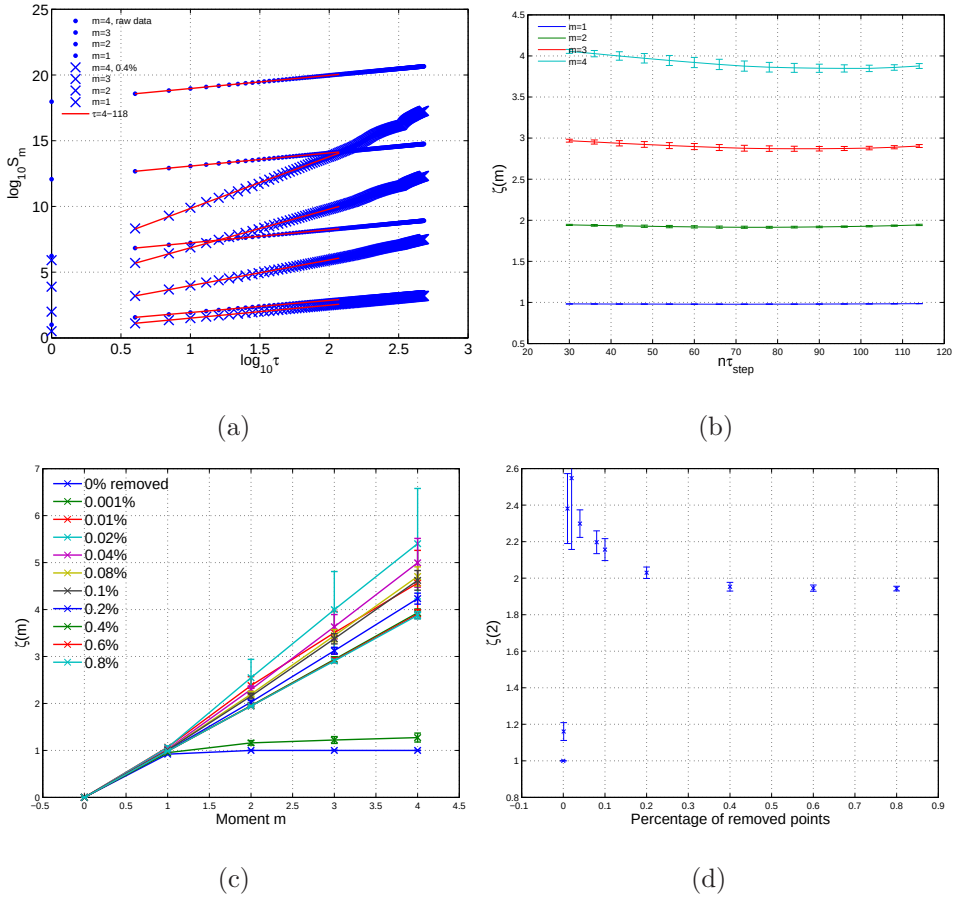

Figure 2-10: The top left panel shows the GSFs for the Lévy flight (β stable with $\beta = 1$) computed for $\tau = 1$ to $\tau = 481$ in steps of 3 for both raw (".") and 0.4% conditioned data ("×") fitted to $\tau = 4$ to $\tau = 118$ (red lines). The top right panel shows how the fitting range is tested by fitting between $\tau = 46$ to 76 and then increasing the fitting range on either side to the next consecutive τ, up to $\tau = 4$ to $\tau = 118$. The bottom panels show the scaling exponents $\zeta(m)$ plotted as a function of moment $m = 1$ to 6 for different percentages of removed points (left panel) and $\zeta(2)$ plotted against the percentage of removed points (right panel).

A Lévy flight has a heavy-tailed distribution, which means that finite-size effects can stongly bias the results. This is manifest in the lower panel of Figure 2-10 by the saturation/roll-over effect in the $\zeta(m)$ plots at $m > \beta$ (references for saturation effect). However upon the successive removal of the most extreme and therefore badly-sampled outliers, we recover the expected scaling behaviour, which is robust beyond the removal of $\sim 0.2\%$ (~ 2000 values) extreme points. Again we can quantitatively estimate H from $\zeta(2) = 2.03 \pm 0.03$, which gives $H = 1.02 \pm 0.02$. This is again similar within errors to the expected value of $H = 1/\beta = 1$. In Figure 2-11, these values of H are used in equation 2-24,

$P(\delta x, \tau) = \tau^{-H} P_s(\tau^{-H}\delta x)$ to test the PDF collapse for the Brownian and Lévy cases.

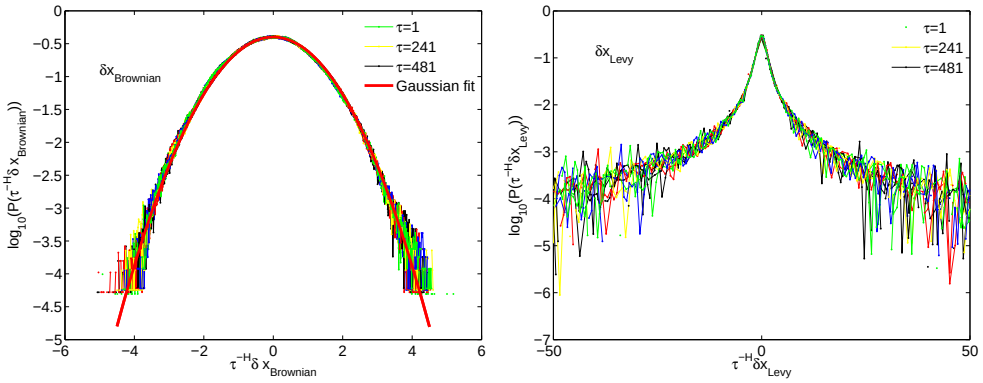

(a) (b)

Figure 2-11: The renormalised PDFs for the steps of the Brownian walk (left panel) and the Lévy flight (right panel) for $\tau = 1$ to $\tau = 481$ in steps of 30. The PDFs are collapsed using the value of H, obtained from the GSF analysis, in equation 2-24. For clarity the legend only shows τ_{min}, τ_{max} and an intermediate τ.

We can see in Figure 2-11, that the collapse process using the Hurst exponent works for both the Lévy flight and the Brownian walk, confirming the monofractal nature of these processes. However, in the heavy tails of the Lévy flight PDF, the collapse doesn't work, hence the need to remove these outliers, when attempting to recover the scaling behaviour. The p-model GSF analysis is now considered.

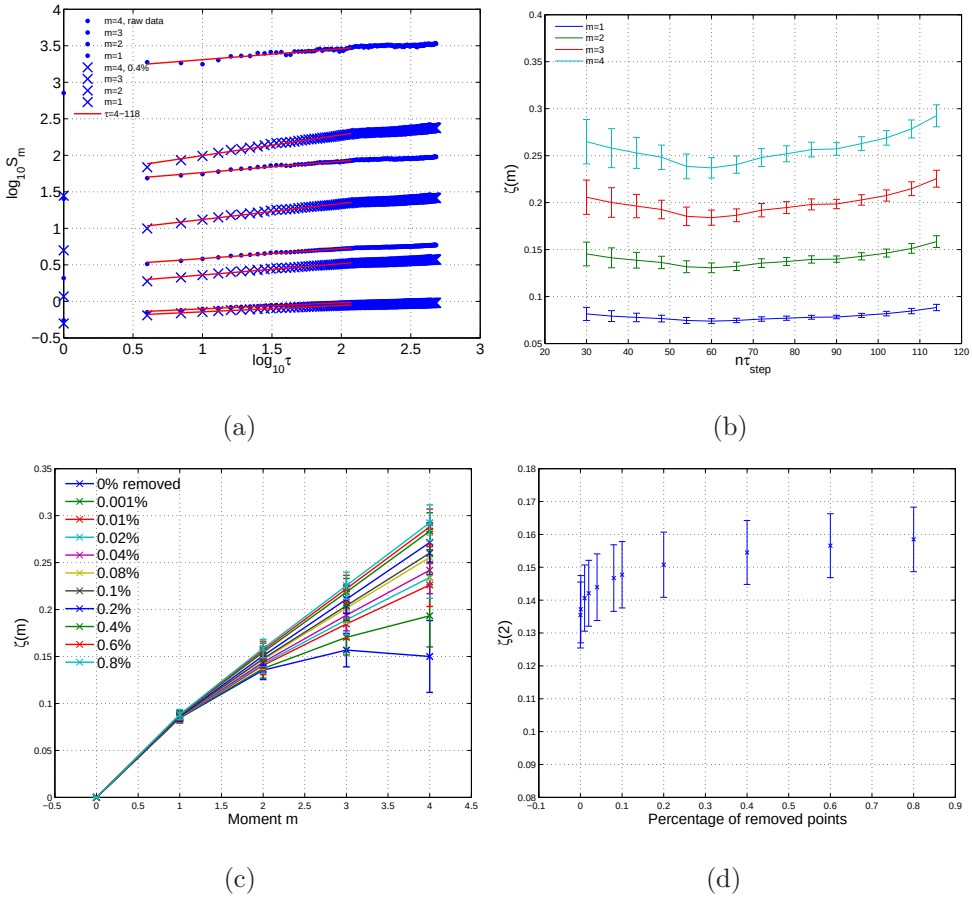

Figure 2-12: The top left panel shows the GSFs for the p-model (generated with $p = 0.6$) computed for $\tau = 1$ to $\tau = 481$ in steps of 3 for both raw (".") and 0.4% conditioned data ("×") fitted to $\tau = 4$ to $\tau = 118$ (red lines). The top right panel shows how the fitting range is tested by fitting between $\tau = 46$ to 76 and then increasing the fitting range on either side to the next consecutive τ, up to $\tau = 4$ to $\tau = 118$. The bottom panels show the scaling exponents $\zeta(m)$ plotted as a function of moment $m = 1$ to 6 for different percentages of removed points (left panel) and $\zeta(2)$ plotted against the percentage of removed points (right panel).

A multifractal can never return a single constant value of H as one changes the range of values over which H is computed; this can be seen for the multifractal p-process (Meneveau & Sreenivasan, 1987) in the lower panels of Figure 2-12.

To conclude, a plot of the value of the exponent (here $\zeta(2)$) as we succesively remove outliers can distinguish fractal and multifractal processes. For processes that are fractal, it also provides a more precise determination of the single exponent H that characterizes the timeseries. Also, each successful computation of a GSF at increasingly high order yields additional information about the nature of the PDF of fluctuations. For practical applications of the GSF analysis

to a broad range of datasets, see for example: MHD turbulence simulations - Merrifield et al. (2005, 2006, 2007); solar wind turbulence - Horbury & Balogh (1997); Hnat et al. (2005); Chapman & Hnat (2007); Nicol et al. (2008); geomagnetic indices Hnat et al. (2003); laboratory plasma turbulence - Budaev et al. (2006) and references therein.

2.6 Extended Self-Similarity

2.6.1 Introduction

We will use our model timeseries to demonstrate extended self-similarity (ESS), already introduced in Chapter 1. Recall that ESS proceeds by replacing τ by an initially unknown generalized timescale $g(\tau)$, such that formally $S_m(\tau) = [S_{m'}(\tau)]^{\zeta(m)/\zeta(m')}$. In Figure 2-13, we show ESS for the Brownian walk, where the S_m are plotted against S_3 on loglog plots. The slopes of the ESS plots, now give us the ratios of the scaling exponents $\zeta(m)/\zeta(3)$. We choose S_3 by convention, as $\zeta(3) = 1$ for ideal Kolmogorov hydrodynamic scaling.

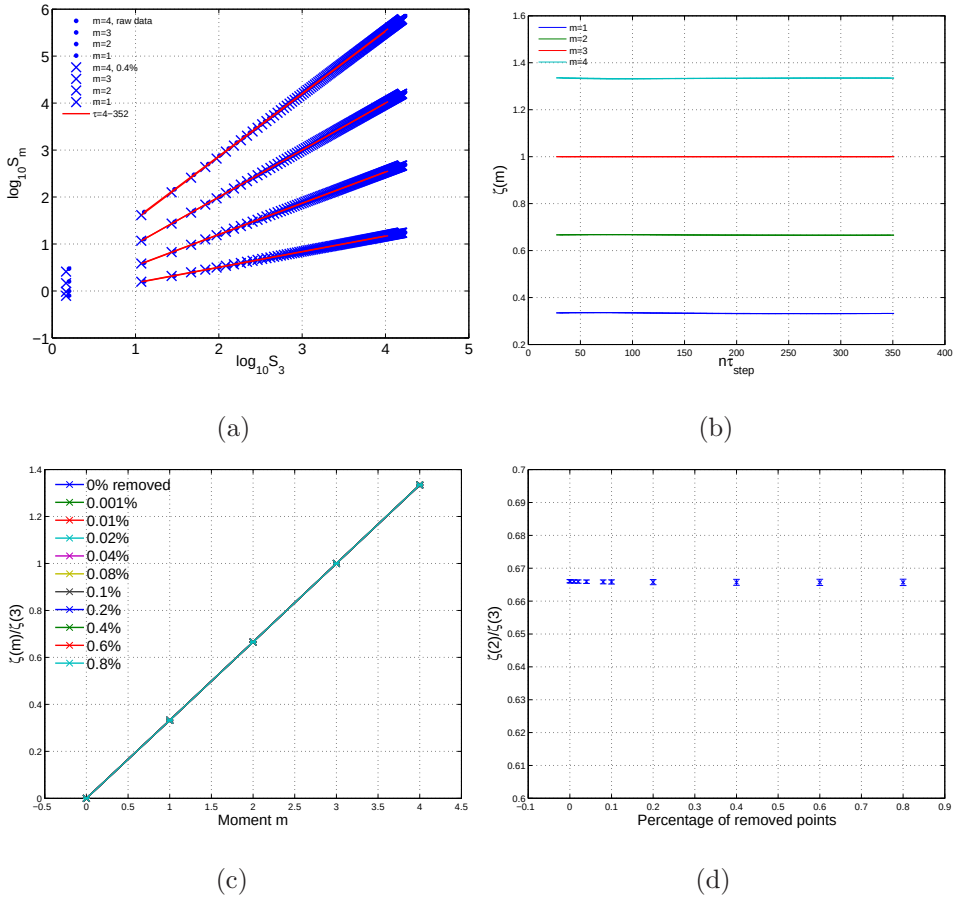

Figure 2-13: The top left panel shows ESS $log_{10}S_m$ versus $log_{10}S_3$ for the Brownian walk computed for $\tau = 1$ to $\tau = 481$ in steps of 3 for both raw (".") and 0.4% conditioned data ("×") fitted to $\tau = 4$ to $\tau = 352$ (red lines). The top right panel shows how the fitting range is tested by fitting between $\tau = 178$ to 193 and then increasing the fitting range on either side to the next consecutive τ, up to $\tau = 4$ to $\tau = 352$. The bottom panels show the scaling exponents $\zeta(m)/\zeta(3)$ plotted as a function of moment $m = 1$ to 6 for different percentages of removed points (left panel) and $\zeta(2)/\zeta(3)$ plotted against the percentage of removed points (right panel).

The Brownian walk is still perfectly behaved and the ratio $\zeta(2)/\zeta(3) \sim 0.67$ as we would expect from our prior knowledge of the fractal scaling behaviour and the Hurst exponent, i.e. $\zeta(2)/\zeta(3) = 2H/3H \sim 0.67$. It is important to stress the ESS cannot give any quantitative information on the scaling exponents, only on their ratios. However it is a useful tool for identifying extended scaling regions and the type of scaling (fractal, multifractal etc.) present. The analysis is repeated for the Lévy Flight (Figure 2-14) and the p-model (2-15).

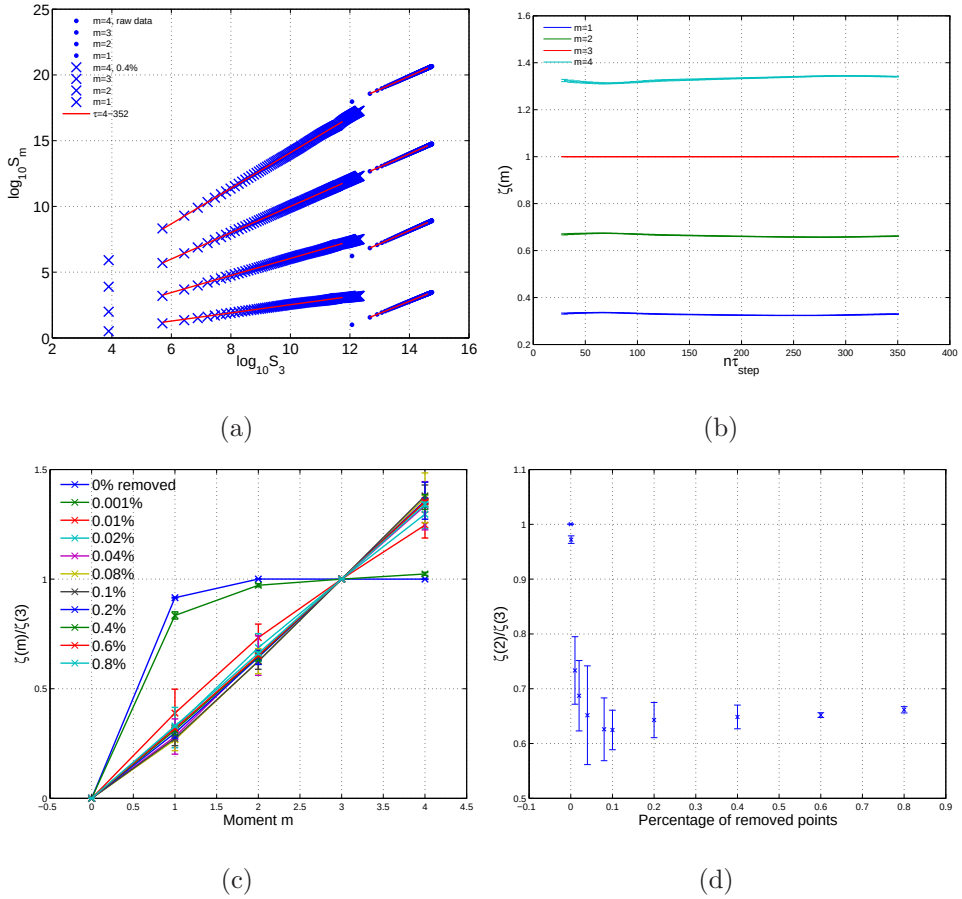

Figure 2-14: The top left panel shows ESS $log_{10}S_m$ versus $log_{10}S_3$ for the Lévy Flight computed for $\tau = 1$ to $\tau = 481$ in steps of 3 for both raw (".") and 0.4% conditioned data ("×") fitted to $\tau = 4$ to $\tau = 352$ (red lines). The top right panel shows how the fitting range is tested by fitting between $\tau = 178$ to 193 and then increasing the fitting range on either side to the next consecutive τ, up to $\tau = 4$ to $\tau = 352$. The bottom panels show the scaling exponents $\zeta(m)/\zeta(3)$ plotted as a function of moment $m = 1$ to 6 for different percentages of removed points (left panel) and $\zeta(2)/\zeta(3)$ plotted against the percentage of removed points (right panel).

Figure 2-14 shows the convergence to fractal behaviour of the Lévy flight, again after removal of $\sim 0.2\%$ of the outliers. The $\zeta(2)/\zeta(3)$ converges to ~ 0.67, which is the result expected for any mono-fractal process under ESS.

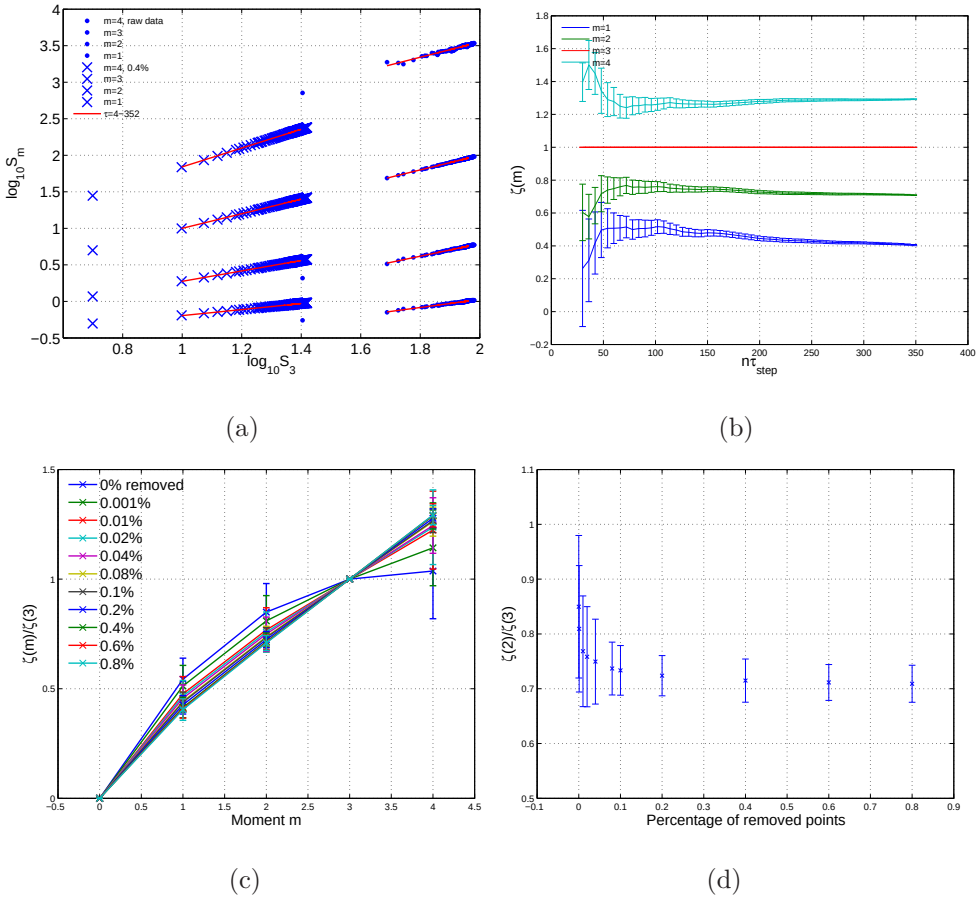

Figure 2-15: The top left panel shows ESS $log_{10}S_m$ versus $log_{10}S_3$ for the p-model computed for $\tau = 1$ to $\tau = 481$ in steps of 3 for both raw (".") and 0.4% conditioned data ("×") fitted to $\tau = 4$ to $\tau = 352$ (red lines). The top right panel shows how the fitting range is tested by fitting between $\tau = 178$ to 193 and then increasing the fitting range on either side to the next consecutive τ, up to $\tau = 4$ to $\tau = 352$. The bottom panels show the scaling exponents $\zeta(m)/\zeta(3)$ plotted as a function of moment $m = 1$ to 6 for different percentages of removed points (left panel) and $\zeta(2)/\zeta(3)$ plotted against the percentage of removed points (right panel).

The behaviour of the $\zeta(m)/\zeta(3)$ exponents for the p-model, shown in the lower panels of Figure 2-15 confirm again the multifractal nature of the p-model process and the impossibility to identify a single characteristic Hurst exponent. Tu et al. (1996) present a derivation for the scaling exponents $\zeta(m)$ of a p-model for fully developed turbulence, assuming that $\zeta(3) = 1$

$$\zeta(m) = 1 - log_2\left(p^{m/3} + (1-p)^{m/3}\right) \tag{2-29}$$

Where p and $(1 - p$ are the fractions of energy transferred from a mother eddy to its daughter eddies. We can see that for p=0.5 this reduces to fractal scaling

and exponents linear in m, whereas $p = 1$ represents the most intermittent case. ESS forces $\zeta_{ESS}(3) = \zeta(3)/\zeta(3) = 1$ we can therefore compare equation 2-29 with our experimental results. In Figure 2-16, the $\zeta_{ESS}(m)$ for 0.4% conditioned data overlaid with the $\zeta(m)$ obtained from equation 2-29 for $p = 0.6$.

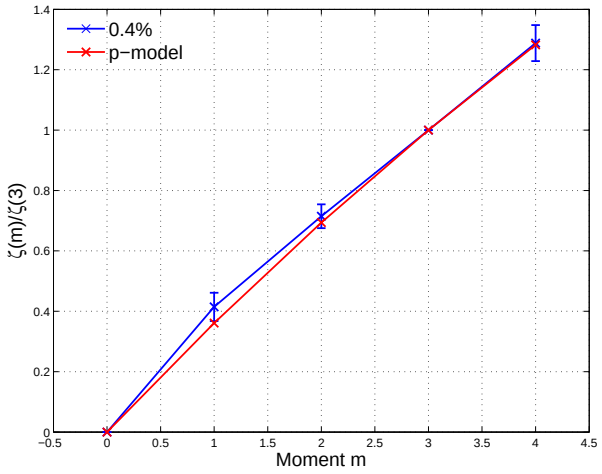

(a)

Figure 2-16: The $\zeta_{ESS}(m)$ for 0.4% conditioned data (blue) are compared to the $\zeta(m)$ exponents obtained from the p-model (red) described in equation 2-29.

From Figure 2-16, it is clear that our experimental results are within errors of the theoretical p-model results. It is therefore possible to extract some quantitative information from the statistical analysis of intermittent or multifractal timeseries, which can give some insight into the nature of the process under consideration

2.7 Conclusions

We have used various spectral and statistical analysis techniques to probe the scaling properties of three very different timeseries.

- For fractal processes such as the Brownian walk, the correct scaling and Hurst exponent ($H = 0.5$) is deduced from the power spectra slope and the generalized structure functions.

- The self-affine nature of a fractal process is shown by the PDF collapse and rescaling using H and the standard deviation and mean. These methods

should indeed be equivalent as the GSF scaling assumption for a fractal process, $S_m =< |\delta x|^m > \sim \tau^{\zeta(m)}$, $\zeta(m) = Hm$, means that both the standard deviation and the mean of the data should be scaling with H.

- Processes, which are still monofractal, but have a more heavy-tailed PDF like the Lévy flight, require more careful analysis due to finite size system effects.

- The correct scaling can be recovered upon application of a data conditioning technique, which removes the poorly sampled outliers from the statistics calculations.

- The p-model is shown to be be multifractal and under ESS, consistent with the expected scaling exponents.

2.8 Further Analysis Methods

These methods are by no means exclusive and other techniques abound to probe the scaling characteristics of timeseries. The original method of determining the Hurst exponent, proposed by Hurst in (Hurst et al., 1965), is known as rescaled range analysis. The ratio of the range (R) of a timeseries $x(t, \tau)$, where R is defined as the difference between the maximum and minimum values of the cumulative sum of $x(t, \tau)$ over a timespan τ, to the scale S, which is taken to be the standard deviation of $x(t)$, has a power-law scaling shown in equation 2-30.

$$\frac{R}{S} = (c\tau)^H \tag{2-30}$$

where the coefficent c was taken to be 0.5 by Hurst and H is the Hurst exponent. R and S are mathematically defined by

$$R = max_{1<t<\tau}(x(t,\tau)) - min_{1<t<\tau}(x(t,\tau)) \tag{2-31}$$

and

$$S = \left[\frac{1}{\tau}\sum_{t=1}^{\tau}(\delta x(t) - < \delta x >_\tau)^2\right]^{\frac{1}{2}} \tag{2-32}$$

where

$$x(t,\tau) = \sum_{t'=1}^{t}(\delta x(t') - < \delta x >_\tau) \tag{2-33}$$

This method gives an indication of the variability of a system over time, and is similar in principle to the way in which we estimated the fractal dimension of a Brownian walk in equation 2-11. The problem often arises in judging over which range of τ to estimate H. If τ is too small, then short time correlations can dominate and the Hurst exponent is no longer a good indication of any long range dependence in the data. At too large scales, there may be insufficent data for good statistics.

Chapter 3

Ulysses results

3.1 Introduction

A key objective of the present work is to relate aspects of the Ulysses solar wind measurements described in the next section: their spectral power density; their intermittency (Bruno et al., 2003); and their spatial location. Recent structure function analysis using WIND and ACE data, taken in the ecliptic plane at 1AU, shows evidence of scaling within the inertial range for $|B|^2$ that is solar cycle dependent (Kiyani et al., 2007). To unravel the interplay between the large scale coronal driver and the evolving inertial range turbulence, we therefore make use of Ulysses polar passes. Ulysses has performed six polar passes and previous studies include Smith & Balogh (1995); Horbury et al. (1996b); Horbury & Balogh (2001) and references therein.

In this Chapter, we seek to characterize the intermittency therefore we remove the minimum of outliers consistent with obtaining good representation of the tails of the probability density functions (PDFs) (Kiyani et al., 2006). This is distinct from, but complimentary to, approaches that seek to eliminate the intermittency by removing significant fractions of the tails of the PDFs, in order to probe the remnant scaling (S. Habbal, private communication, 2007). We perform generalized structure function (GSF) analysis, on intervals of quiet solar wind as seen by Ulysses. We show that while GSF is not sufficient to reveal scaling in the inertial range, extended self-similarity (ESS) successfully recovers self-similar behavior. Furthermore we examine the possible latitudinal and radial dependences of both the inertial and "$1/f^{\alpha}$", $\alpha \rightarrow 1$, ranges, and conclude that the inertial range, unlike the "$1/f^{\alpha}$" regime, shows very little variation with spacecraft position over the 60 days considered. We focus here on magnetic field fluctuations for our analysis rather than Elsässer variables, since these involve velocity measure-

ments at lower cadence; however see Sorriso-Valvo et al. (2007), where local (in time) scaling properties are also considered.

3.2 Quantifying Scaling

As we saw in Chapter 2, a time series $y(t)$ exhibits scaling (Sornette, 2004), if $S_m = \langle |y(t+\tau) - y(t)|^m \rangle \sim \tau^{\zeta(m)}$. Here the angular brackets denote an ensemble average over t, implying an assumption of weak stationarity. In practice, we examine the data over a sufficiently large range of time intervals τ in order to establish the power law dependence; that is, the scaling exponent $\zeta(m)$.

As discussed in Chapter 1, section 5.4, the point of contact between time and length scales is the Taylor hypothesis (Taylor, 1938), where in the high speed flow the time interval τ plays the role of a longitudinal lengthscale. The power law dependence of the S_m expresses a generic scaling property and since the coronal magnetic carpet is known to be fractal and the large scale coronal dynamics as seen in solar flare statistics exhibit scaling, one might anticipate that a propagating signature of coronal origin might also show scaling which could be captured by the $\zeta(m)$ scaling exponents. In practice, we test for scaling by computing the associated generalized structure functions or GSF (Burlaga & Klein, 1986; Ruzmaikin et al., 1993, 1995b; Marsch & Tu, 1996; Horbury & Balogh, 1997, and references therein). As shown previously, for a perfectly self-similar process, such as the Kolmogorov cascade or a random fractal, $\zeta(m)$ depends linearly on m. Turbulent flows are typically intermittent, nevertheless, S_m scaling with τ would be expected in uniform, fully developed turbulence in an infinite domain. In practice, power law scaling is not always found. As detailed in Chapter 1, section 5.6, this may reflect the finite spatial domain, or that the turbulence is not fully evolved. We will see that this is the case for the inertial range in quiet intervals of Ulysses observations. However extended self-similarity (ESS) does turn out to be applicable to our datasets.

The measured vector magnetic field time series, $\mathbf{B}(t)$, is differenced for time lags τ in the range 1 minute to 50 minutes, yielding a series $\delta y_i(t, \tau)$ for its three

components

$$\delta y_i(t,\tau) = B_i(t+\tau) - B_i(t) \tag{3-1}$$

where i denotes the component of $\mathbf{B}$ under consideration. Assuming time-stationarity, the t dependence in $\delta y_i(t,\tau)$ can be dropped:

$$S_m(\tau) = \langle |\delta y_i|^m \rangle = \int_{-\infty}^{\infty} |\delta y_i|^m P(\delta y_i, \tau) d(\delta y_i) \tag{3-2}$$

where $P(\delta y_i, \tau)$ is the probability density function of δy_i, $< \cdot >$ again denotes temporal averaging and m is a positive integer. The effect of outliers becomes increasingly apparent in the higher order structure functions, subject to statistical constraints, which typically limits consideration to $m \leq 6$. We therefore apply the conditioning technique (Kiyani et al., 2006) outlined in Chapter 2.

3.3 The Datasets

In 1995, the Ulysses spacecraft spent three months above the North polar coronal hole, in quiet fast solar wind. As this was close to a period of minimum solar activity, the magnetic topology of the Sun was relatively simple, free from transient events such as solar flares. The Sun's surface magnetic field was actually dipolar during this time, positive or outwards in the Northern hemisphere and negative or inwards in the Southern hemisphere (Forsyth et al., 1996).

Throughout this Chapter, we present results separately for each 10 day contiguous interval from day 180 to 239 of 1995, while Ulysses was above the Northern coronal hole. Each dataset comprises approximately $13,000$ datapoints of one minute averaged measurements. This enables us to explore both the scaling properties of the inertial and "$1/f^{\alpha}$" ranges and to test for radial and latitudinal dependencies. Over these 60 days, Ulysses moved from 1.7926 AU to 2.2043 AU heliospheric distance and through 73.76° to 77.03° heliographic latitude, with a peak at 80.22° on days 212 and 213. The successive time intervals are compared in order to identify any radial or latitudinal trend. The study is restricted to the radial (R), tangential (T) and normal (N) magnetic field components and uses one minute averaged measurements in order to remove any possible sub-spacecraft spin artefacts.

3.4 Ulysses Observations and Scaling

3.4.1 Power Spectra

The magnetic field power spectra are computed using the multitapering spectral analysis method (Percival, 1993).

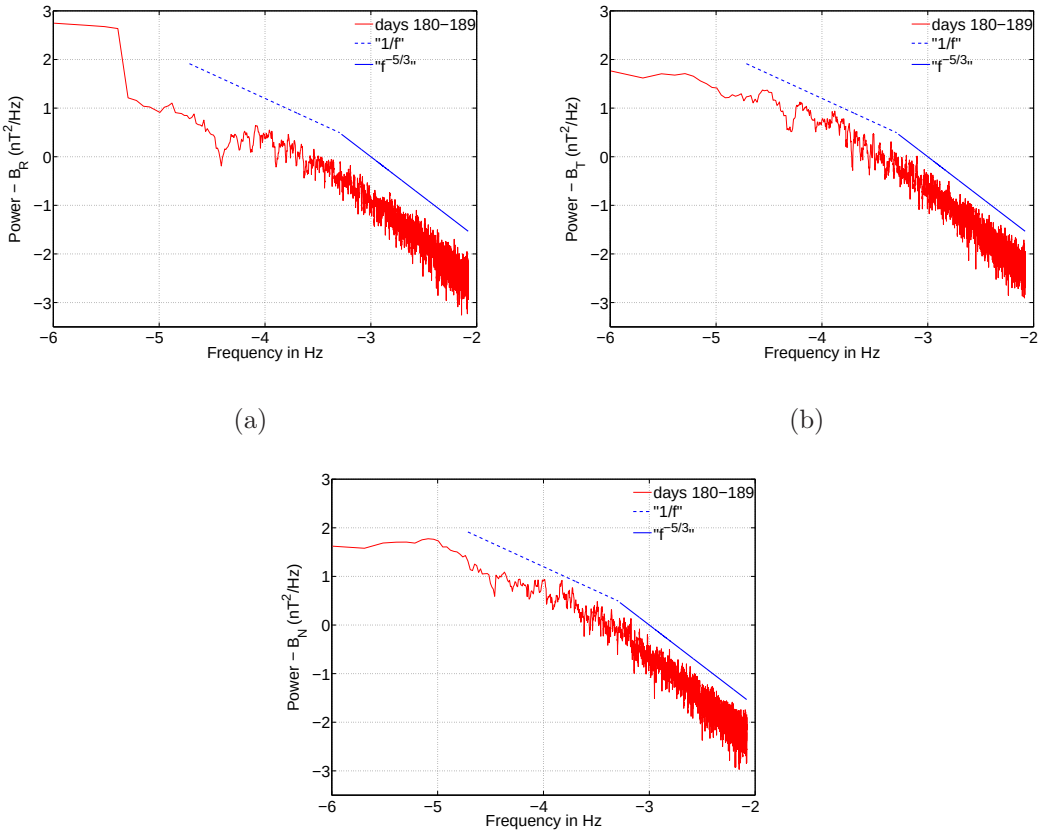

(a) (b)

(c)

Figure 3-1: Log-log plots of the B-field components' power spectra for days $180 - 189$. Two regions with different scaling exponents are distinguishable with a break between frequencies at $10^{-3.5} - 10^{-3}$Hz, consistent with previous results (Horbury et al., 1996a). For comparison purposes, -1 and $-5/3$ power scaling laws are also shown. The power spectra for the other time intervals examined show similar behavior.

In Figure 3-1 we see that the power spectra show an inertial range with a Kolmogorov-like behavior at higher frequencies and a characteristic flattening of the spectra at lower frequencies. The existence of this regime is well-known in many physical processes (Bak et al., 1987), including the interplanetary magnetic

field (Matthaeus et al., 2007). The power spectra reveal power law scaling, but give no information on intermittency or on whether the turbulent cascade is active; for this we turn to the associated GSFs.

3.4.2 Generalized Structure Functions

We first summarise the scaling behavior seen in the different time intervals in Figure 3-2, where we plot S_3 versus τ for the data conditioned by clipping 0.1% outliers following the technique of Kiyani et al. (2006).

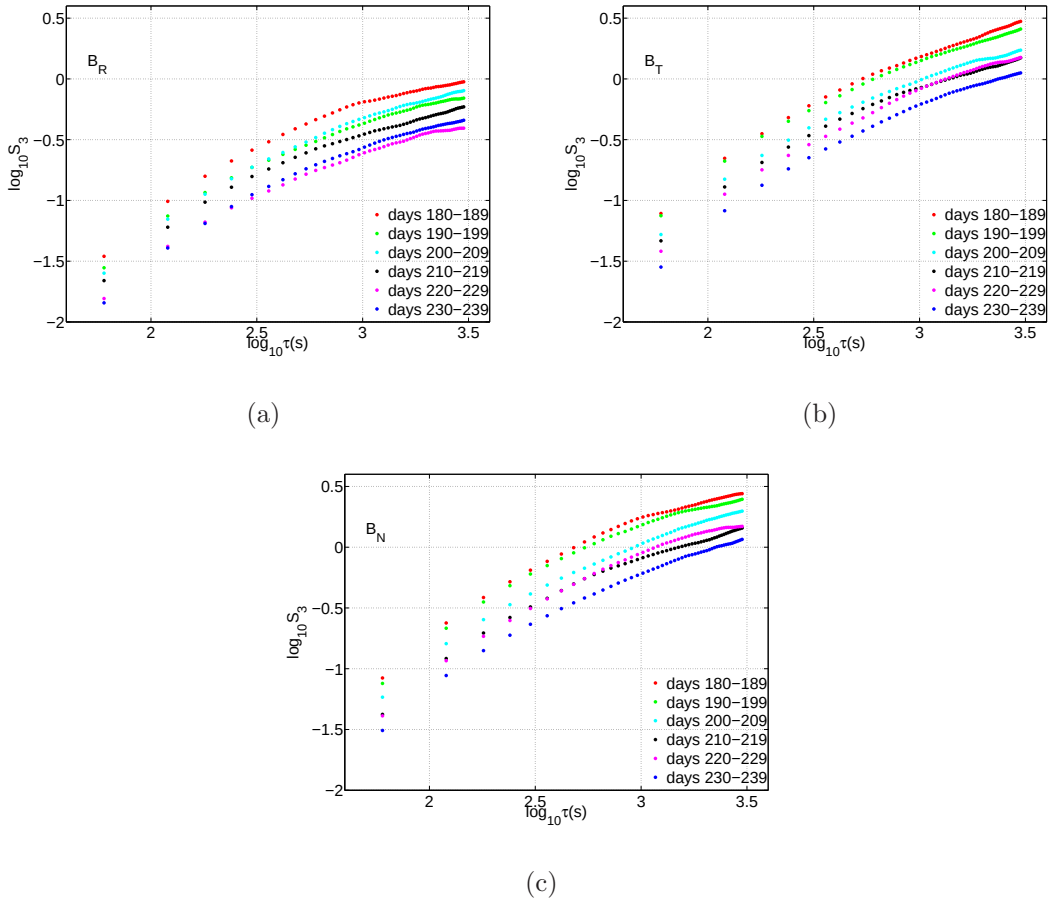

(a) (b)

(c)

Figure 3-2: Log-log plots of third order structure function S_3 versus sampling interval τ for all three components of magnetic field fluctuations in the solar wind measured by the Ulysses spacecraft during contiguous intervals of ten days, which are plotted separately on each panel, from day 180 to day 239 of 1995. Only the 0.1% conditioned data is shown for clarity.

The existence of two distinct scaling regions in Figure 3-2 is clear. For the small τ region we see the inertial range with scaling exponents $\zeta_S(m)$, whereas the large

τ region corresponds to the "$1/f^{\alpha}$" range with scaling exponents $\zeta_L(m)$. Figure 3-3 shows that linear regression applied to the third order structure functions for both raw and conditioned data yields power-law scaling in the "$1/f^{\alpha}$" range. However this does not appear to be the case for the inertial range, where the S_m clearly curve for $\tau \leq 30$ minutes. The ζ exponent numerical values for the raw and conditioned GSF data differ by no more than $\sim 6\%$ on average, with the higher order moments showing stronger variations, as expected.

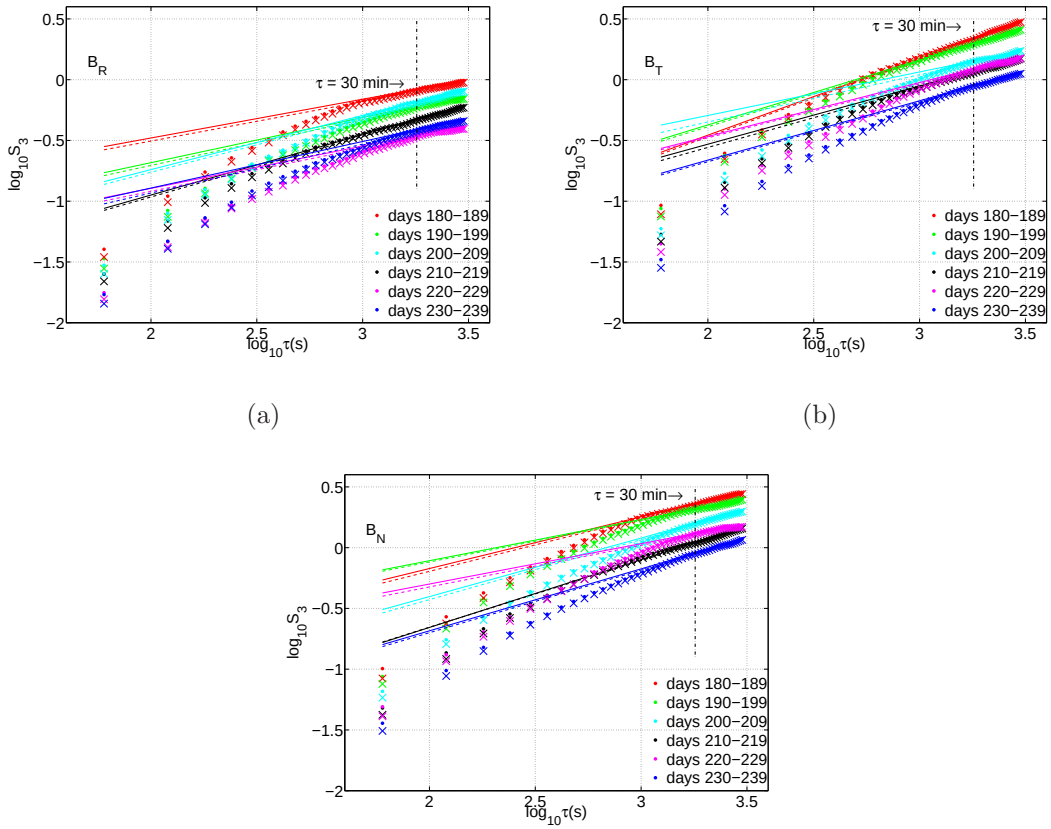

Figure 3-3: Log-log plots of third order structure function S_3 versus sampling interval τ for all three components of magnetic field fluctuations in the solar wind measured by the Ulysses spacecraft during contiguous intervals of ten days, which are plotted separately on each panel, from day 180 to day 239 of 1995. The raw data is represented by "·" and the 0.1% conditioned data by "×". Top left panel: radial field B_R. Top right panel: tangential field B_T. Bottom panel: normal field B_N. For $\tau \geq 30$ minutes, corresponding to "$1/f^{\alpha}$" power spectral density, scaling of the form $S_m \sim \tau^{\zeta(m)}$ is observed with $\zeta_{L,R}(3) = 0.399 \pm 0.011$, $\zeta_{L,T}(3) = 0.508 \pm 0.010$ and $\zeta_{L,N}(3) = 0.445 \pm 0.008$; solid lines show linear regression fits for 26 minutes $\geq \tau \geq$ 49 minutes for 0.1% conditioned data, whereas the dashed lines show the same fits for the raw data. For $\tau \leq 30$ minutes, corresponding to the inertial range, there is no scaling but the data suggest a possible common $g(\tau)$.

Figures 3-2 and 3-3 suggest that a single function $g(\tau)$ may be common to all the time intervals considered. We test this conjecture in Figure 3-4, by normalizing all the S_3 log plots to their value at $\tau = 30$min., close to the centre of the τ range. The curves overlay quite closely, and there is no secular latitudinal or radial dependence of $g(\tau)$.

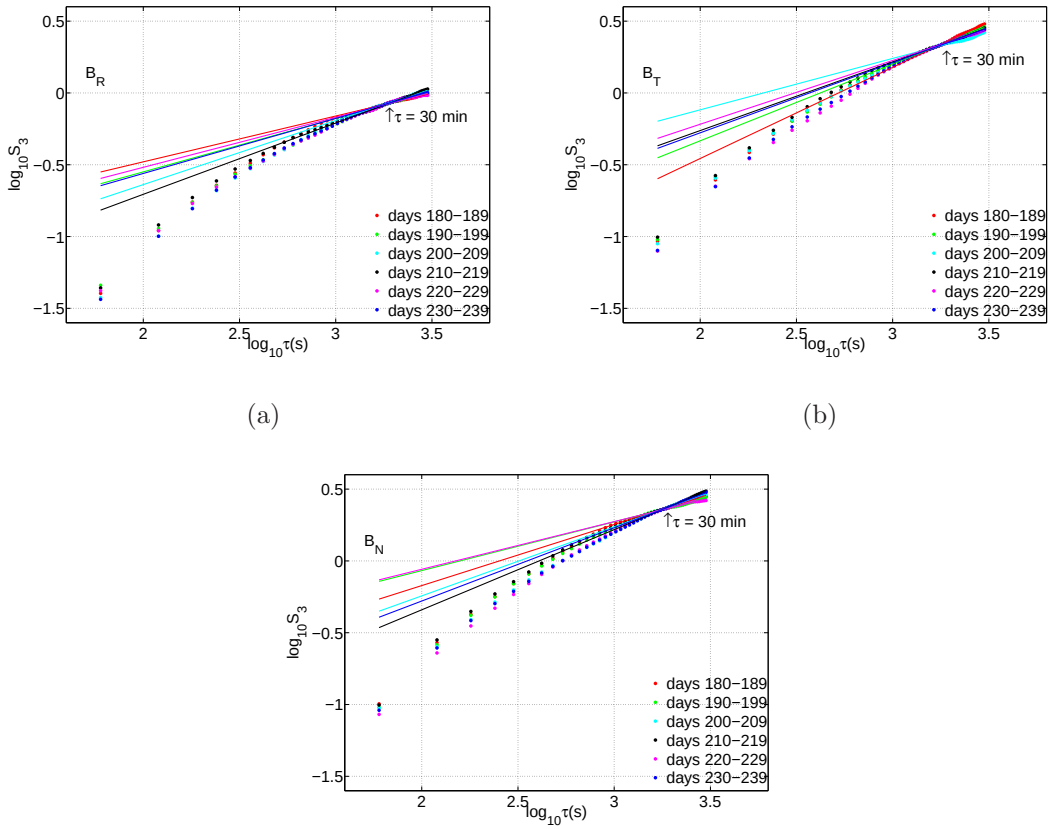

Figure 3-4: Evidence for limited variation in $\zeta(3)$ between ten-day data runs in the scaling region, and for a common $g(\tau)$ between the different time intervals. Data for B_R, B_T and B_N from Figure 3-2 are replotted after normalization such that the value of $S_3(\tau = 30$ minutes) is the same for each ten-day run within each panel. Gradients in the scaling range (solid lines) do not vary systematically with their timing with respect to the 60-day observation period, nor do they vary in the same way for different magnetic field components. Away from the scaling region, points appear to lie close to a common curve, reflecting $g(\tau)$.

The displacements of the curves in Figures 3-2 and 3-3 arise from the data: as Ulysses moves, the GSF and ESS plots shift in a relatively ordered way, consisent with different power levels in the fluctuations as a function of position. In Figure 3-5 we examine this further by showing the variations of a single point on each line, $S_3(\tau = 30)$ as a function of time and therefore function of increasing radial distance and varying heliographic latitude, for all B field components.

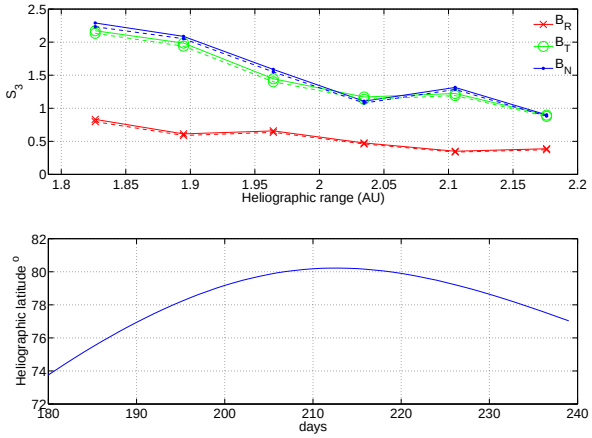

Figure 3-5: Dependence of the value of $S_3(\tau = 30$ minutes) on sampling time - a proxy for mean location of the moving Ulysses spacecraft - for B_R, B_T and B_N. Here interval one refers to days 180 to 189 of 1995, and interval six to days 230 to 239.

$S_3(\tau = 30)$ for all three components exhibits a secular trend and decreases with time as heliographic range increases. There is no significant latitudinal variation, although there is a flattening of the slope after $\sim$ day 210 (or interval 4), when Ulysses passes over the solar pole and the heliographic latitude starts to decrease again. This is more apparent in the N and T components, the R component seeming relatively unaffected. This is consistent with the work of Goldstein et al. (1995a), who also observed a stronger radial, rather than latitudinal, dependence of the turbulent properties.

3.4.3 Extended Self-Similarity

Let us now test more precisely for $S_m \sim [g(\tau)]^{\zeta(m)}$ within the inertial range by applying ESS to the data. We first apply the technique to the entire τ range of $2-49$ min., with results shown in Figures 3-6 and 3-7. We will also however consider the results from the GSFs and fit to the inertial and "$1/f$" regions separately.

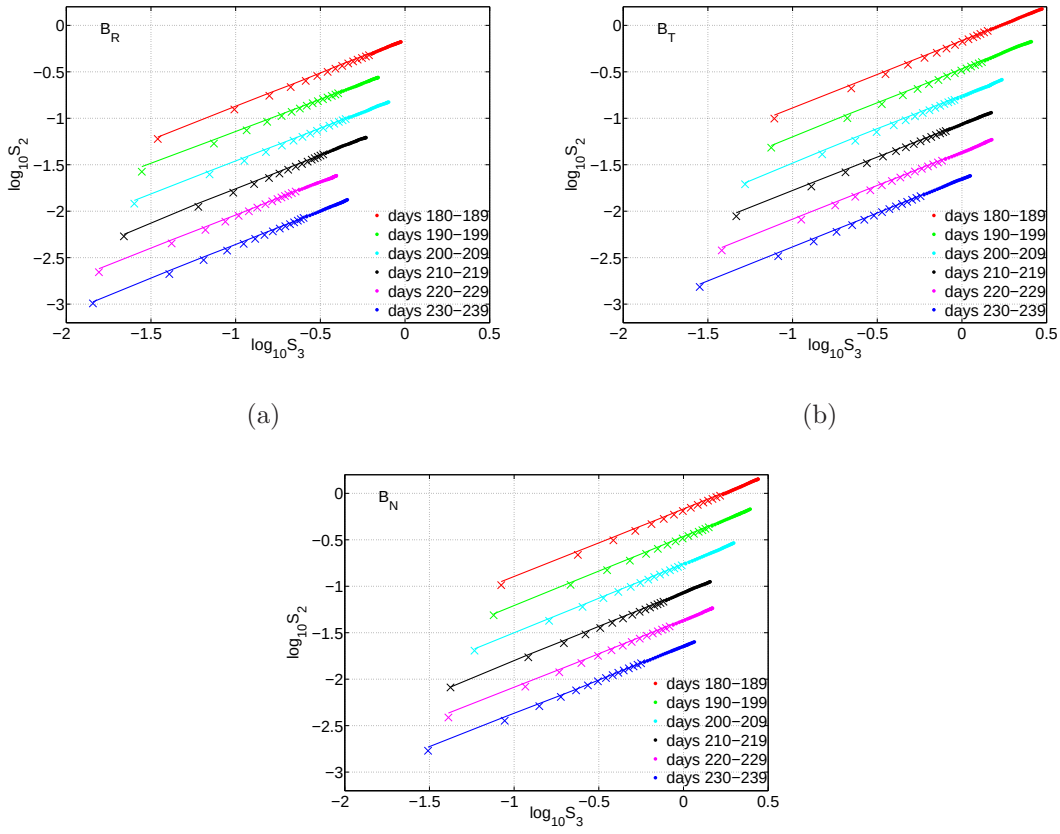

(a) (b)

(c)

Figure 3-6: Evidence for extended self-similarity (ESS) across the full τ range. Log-log plots of second order structure function S_2 versus third order structure function S_3 for all three components of magnetic field fluctuations in the solar wind measured by the Ulysses spacecraft during contiguous intervals of ten days, which are plotted separately on each panel, from day 180 to day 239 of 1995. The different intervals have been uniformly shifted in the y-direction for clarity. Top left panel: radial field B_R. Top right panel: tangential field B_T. Bottom panel: normal field B_N. Data points in the inertial range are marked by crosses, and in the "$1/f^{\alpha}$" range by open circles. The straight lines show linear regression fits across the full temporal range from $\tau = 2 - 49$min. These results imply a global average fitting across the different time intervals of $\zeta_R(2)/\zeta_R(3) = 0.749 \pm 0.004$, $\zeta_T(2)/\zeta_T(3) = 0.759 \pm 0.004$ and $\zeta_N(2)/\zeta_N(3) = 0.765 \pm 0.004$.

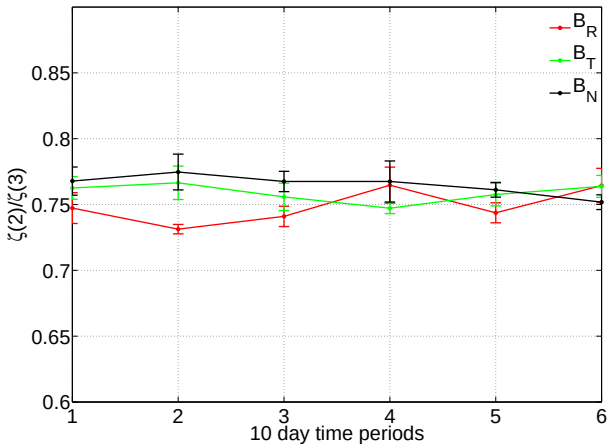

Figure 3-7: Variations of $\zeta(2)/\zeta(3)$ for fits to the full τ range ($\tau = 2 - 49$min.) for B_R, B_T and B_N. Here interval one refers to days 180 to 189 of 1995, and interval six to days 230 to 239.

Power law scaling is recovered for the entire τ range considered. ESS also seems to extend the inertial range scaling region and, apart from a few exceptional cases, it is generally difficult to distinguish clearly between the inertial range and "$1/f^{\alpha}$" ranges from these plots. Figure 3-6 shows a reasonable linear fit to the whole τ range but we see a small but systematic displacement of the data from the fitted line at higher frequencies. Figure 3-7 shows the ESS exponents $\zeta(2)/\zeta(3)$, obtained from the gradients of the linear fits in Figure 3-6, which exhibit no dependence on the time interval considered.

However the GSF analysis has given prior indication of the τ at which the transition from one regime to the other occurs. It is therefore of interest to apply ESS analysis separately to the two regions - inertial range and "$1/f^{\alpha}$" - identified above. As we discuss below, Figures 3-8 to 3-10 then demonstrate that the "$1/f^{\alpha}$" range is the dominant source of variation, in clear contrast to the inertial range. Figure 3-8 repeats the ESS analysis for the inertial range with $\tau = 2 - 14$ min., and Figure 3-9 for the "$1/f^{\alpha}$" range with $\tau = 26 - 49$ min.

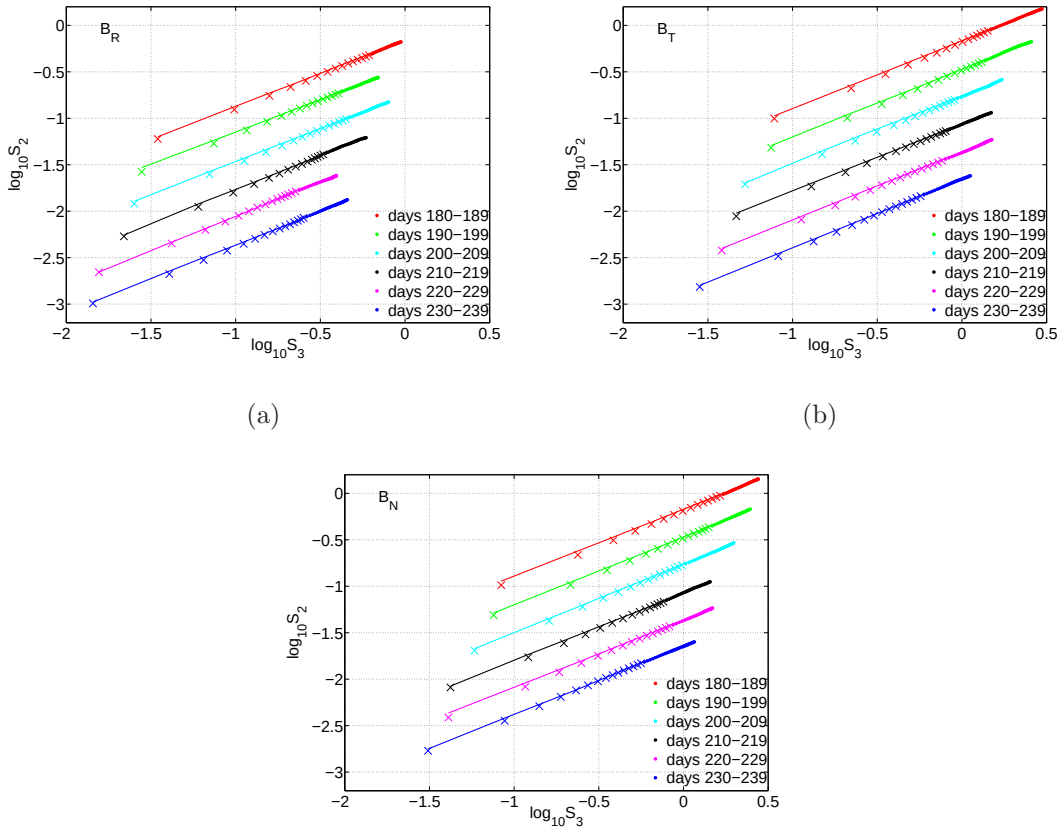

(a) (b)

(c)

Figure 3-8: As it Figure 3-6 but showing fits for the inertial range between $\tau = 2 - 14$ min. These results imply that on average across the different time intervals $\zeta_{S,R}(2)/\zeta_{S,R}(3) = 0.747 \pm 0.008$, $\zeta_{S,T}(2)/\zeta_{S,T}(3) = 0.757 \pm 0.007$ and $\zeta_{S,N}(2)/\zeta_{S,N}(3) = 0.753 \pm 0.005$ in the inertial range.

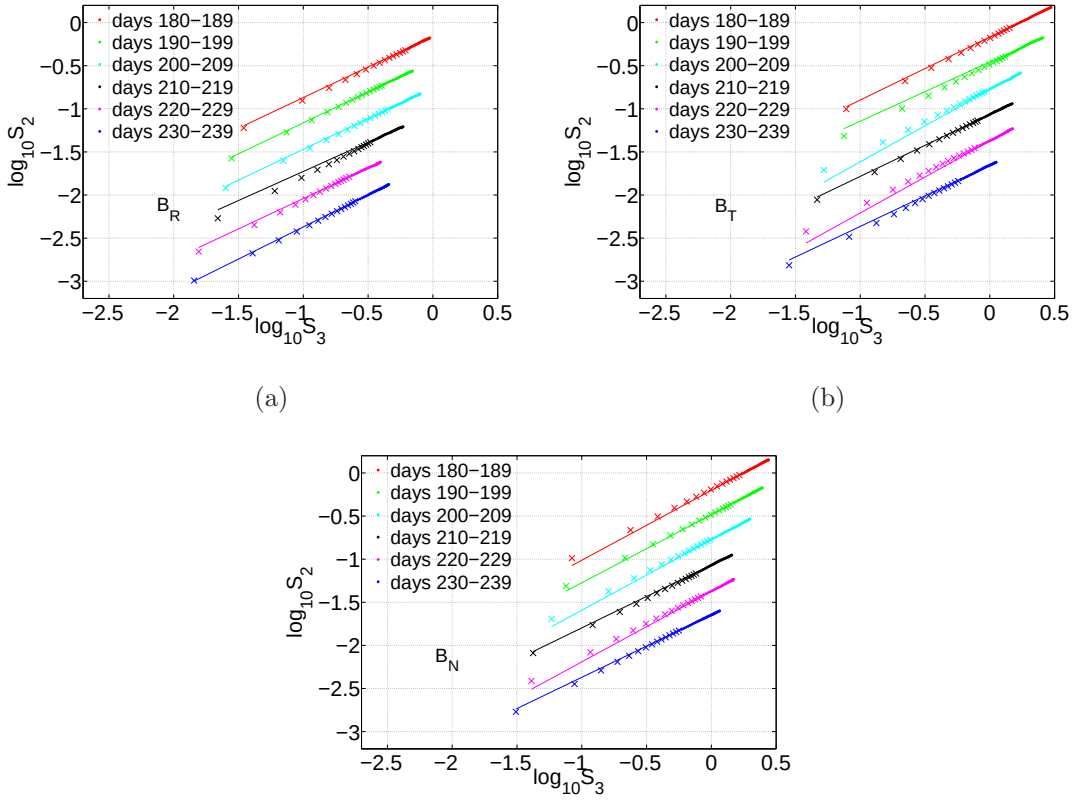

(a) (b)

(c)

Figure 3-9: As in Figure 3-6 but showing fits for the "$1/f^{\alpha}$" range between $\tau = 26-49$ min. These results imply that across the different time intervals $0.675 \pm 0.017 \leq \zeta_{L,R}(2)/\zeta_{L,R}(3) \leq 0.745 \pm 0.017$, $0.687 \pm 0.019 \leq \zeta_{L,T}(2)/\zeta_{L,T}(3) \leq 0.835 \pm 0.034$ and $0.724 \pm 0.004 \leq \zeta_{L,N}(2)/\zeta_{L,N}(3) \leq 0.817 \pm 0.012$ in the "$1/f^{\alpha}$" range.

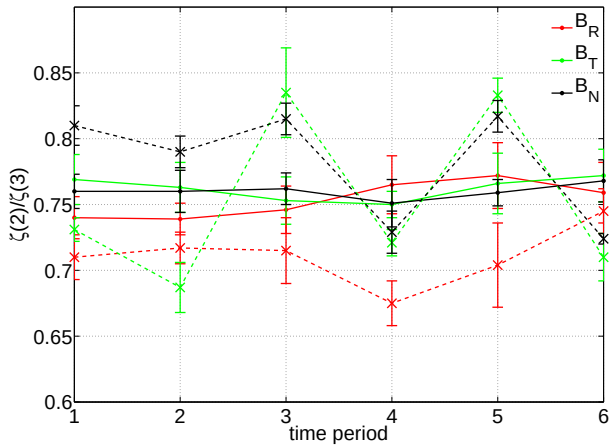

Figure 3-10: Variations of $\zeta(2)/\zeta(3)$ for fits to the inertial range (solid lines, $\tau = 2 - 14$min.) and the "$1/f^{\alpha}$" range (dashed lines, $\tau = 26 - 49$min.) for B_R, B_T and B_N. Here interval one refers to days 180 to 189 of 1995, and interval six to days 230 to 239.

The difference between the inertial range and "$1/f^{\alpha}$" fits can be seen in Figure 3-10, where the gradients of the fits are shown. Importantly, Figure 3-10 demonstrates that the dominant contribution to the scatter in the corresponding global plot, Figure 3-5, arises from the "$1/f^{\alpha}$" region at larger τ. This aligns with what was found with the GSF analysis, see Figure 3-3.

The GSF plots in Figure 3-2 can be fitted using a quadratic fit of the form

$$log_{10}S_m(\tau) \sim \alpha(m)(log_{10}\tau)^2 + \beta(m)(log_{10}\tau) + \gamma \tag{3-3}$$

where γ contains the secular variation in S_3 seen in Figure 3-5. Equation (3-3) can be rewritten in the form

$$S_m(\tau) \sim \tau^{-a(m)(log_{10}(\tau)+\lambda)} \sim [\tau^{-log_{10}(\tilde{\lambda}\tau)}]^{a(m)} \tag{3-4}$$

where $\tilde{\lambda} = 10^{\lambda} = 10^{-7.575\pm0.246}$ is found by taking an average over fits for all the different time intervals. The minus sign is necessary if we insist on positive scaling of exponents $a(m)$ as α is negative and β is positive. In Figure 3-11, we show λ for all components and time intervals.

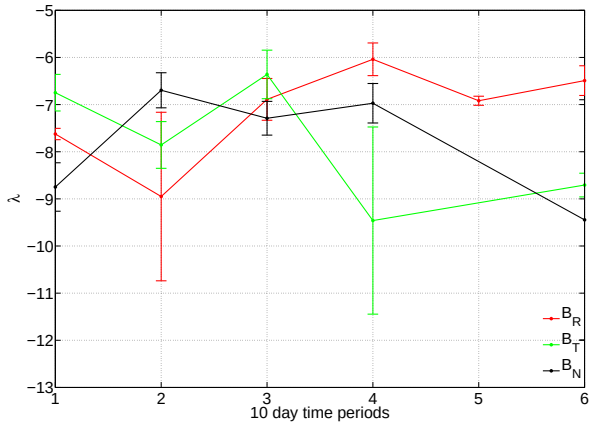

Figure 3-11: Variations of λ for α and β quadratic fits (see equations (3-3) and (3-4)) to the inertial range ($\tau = 2 - 14$min.) for B_R, B_T and B_N. Here interval one refers to days 180 to 189 of 1995, and interval six to days 230 to 239.

In Figure 3-11 we plot the GSFs versus $g(\tau)$. We can see that a good straight line is recovered.

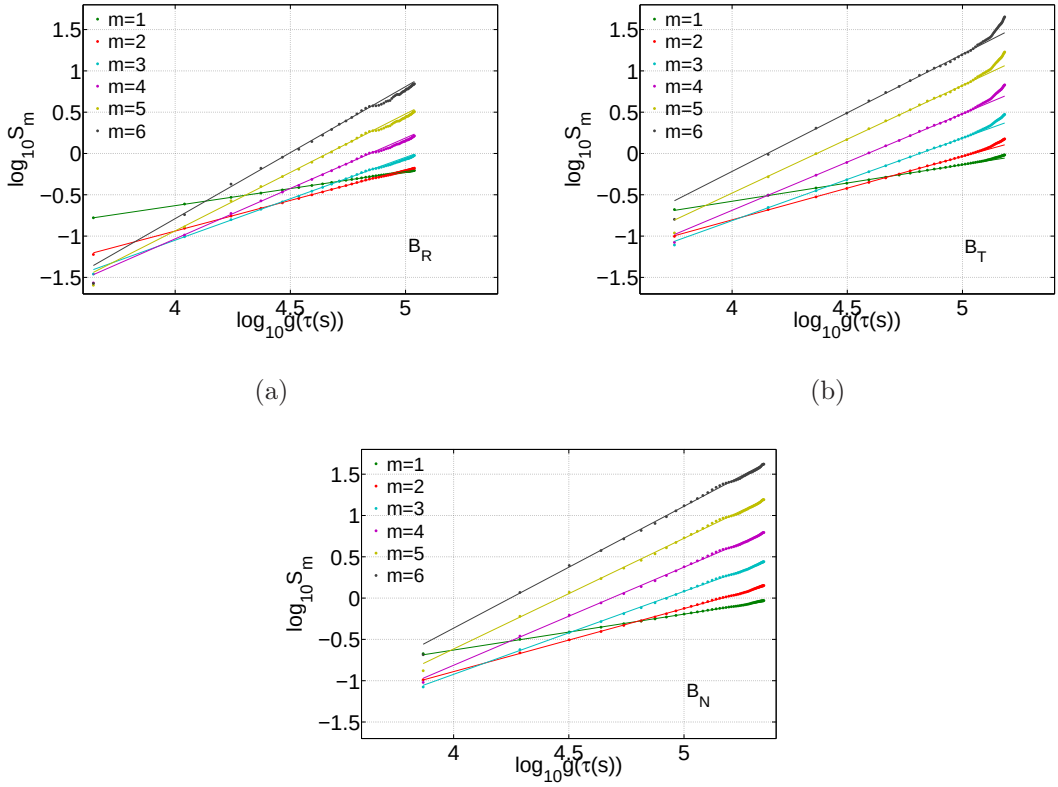

(a) (b)

(c)

Figure 3-12: Evidence for $g(\tau)$ dependence in the inertial range. Log-log plots of the GSFs for moments $m = 0 - 6$ versus $g(\tau)$ for all three components. A single time interval is shown here, days $180 - 189$; the same analysis was done for the other time intervals and similar results found. The $g(\tau)$ is normalized for each component such that $\zeta_S(3) = 1$. This is achieved by obtaining $\zeta_S(3)$ from a linear regression fit of the GSF for each component and then incorporating this into the $g(\tau)$ expression such that $g(\tau) = \tau^{-log_{10}(\tilde{\lambda}\tau)\zeta_i(3)}$ where $i = R,\ T$ or N. The break between the inertial range and "$1/f^{\alpha}$" ranges does not seem to change position from the GSF but is clearer in these plots.

Finally let us again consider the behavior of the ζ_S exponents for $m = 1-6$ for all components and time intervals. These can be fitted to the multifractal p-model. The values of $\zeta(m)$ are then given by $\zeta(m) = 1 - log_2\left(p^{m/3} + (1-p)^{m/3}\right)$. For the data considered here, p-model fits of the ζ_S exponents for the different components during the first time interval give $p_R = 0.79 \pm 0.01$, $p_T = 0.85 \pm 0.01$ and $p_N = 0.84 \pm 0.01$. These values are consistent with previous work by Horbury & Balogh (1997), who found $p \sim 0.8$, and by Pagel & Balogh (2001).

3.5 Conclusions

In this Chapter we have analysed Ulysses quiet fast polar solar wind magnetic field measurements to study the evolving turbulence. We quantify the scaling behavior of both the inertial range (i.e. power spectrum $\sim f^{-5/3}$) and the lower frequency "$1/f^{\alpha}$" range present in the solar wind. Six contiguous intervals of ten days, over which approximate stationarity can be assumed, were studied using the Taylor hypothesis to relate temporal and spatial scales. The scaling that we establish is "macroscopic" in the sense that it is obtained over these time intervals of ten days. One can also consider local (in time) scaling properties (Sorriso-Valvo et al., 2007). We use generalized structure functions (GSF) and extended self-similarity (ESS) to quantify statistical scaling, and find that:

- GSF is sufficient to reveal power law scaling in the low frequency "$1/f^{\alpha}$" range of the form $\langle |y(t+\tau)-y(t)|^m \rangle \sim \tau^{\zeta(m)}$, but ESS is necessary to reveal scaling in the inertial range. This implies a scaling of the form $\langle |y(t+\tau)-y(t)|^m \rangle \sim [g(\tau)]^{\zeta(m)}$ over the inertial range.

- The "$1/f^{\alpha}$" range scaling varies in a non secular way with spacecraft position as found previously (Horbury et al., 1995b). This is consistent with a coronal origin for the "$1/f^{\alpha}$" scaling.

- In the inertial range, comparisons of the third order structure function S_3 for the different time intervals show that the function $g(\tau)$ is independent of spacecraft position, although an ordered trend in the absolute value of S_3 with increasing radial distance is observed.

- A good fit to the inertial range is $g(\tau) \sim \tau^{-log_{10}(\tilde{\lambda}\tau)}$, where $\tilde{\lambda} = 10^{-7.575 \pm 0.246}$. However, this fit does pose several problems, particulary in the limit of $\tau \to 0$ and doesn't really present any physical meaning, we propose a different fit in Chapter 4.

- The exponents found for the inertial range, normalized such that $\zeta_S(3) = 1$, are fitted by a p-model with $p_R = 0.79 \pm 0.01$, $p_T = 0.85 \pm 0.01$ and $p_N = 0.84 \pm 0.01$. This implies a higher degree of intermittency in the normal components of the magnetic field than in the radial component.

Our results clearly differentiate between the dynamics of the fluctuations seen in the "$1/f^{\alpha}$" and in the inertial range. Intriguingly, the inertial range signature is not simply that expected from homogeneous and infininte R_E turbulence, in that there is a generalised scaling function $g(\tau)$ for the scaling. This is highly suggestive of turbulence in a confined or space-varying medium, see for example the work of Biskamp & Müller (2000). Our function $g(\tau)$ may therefore capture the evolution of the turbulence observed at Ulysses, reflecting both the heating of the fast solar wind at the corona and the subsequent expansion in the presence of the large scale solar magnetic field.

Chapter 4

Ulysses and Universality

4.1 Introduction

In Chapter 3, we probed the statistical properties of the fast quiet solar wind ar solar minimum using Ulysses vector magnetic field measurements. We found that extended self-similarity holds for the structure functions S_m in the inertial range, and that $S_m \sim g(\tau)^{\zeta(m)}$. In this Chapter we propose a different fit $g(\tau/\tau_0)$ to the one presented in Chapter 3 and further explore the universal properties of this function.

It is an open question, whether evolving turbulence has an universal nature despite the different mechanisms at its origin and evolution. It is then interesting to examine which features of solar wind turbulence are universal across an anisotropic finite-sized system with finite R_E and different levels of activity. We test the idea that this function $g(\tau/\tau_0)$ is invariant by applying GSF and ESS to Ulysses magnetic field data for fast quiet polar wind flows. Ulysses spent many months in the fast quiet solar wind emanating from the solar polar coronal holes during 2 successive solar minima in $1994-1995$ and $2007-2008$, thus providing for the first time an opportunity to study the accelerated fast solar wind in a relatively simple open radial magnetic field configuration. Of particular interest is a comparison between these two solar minima.

The most recent solar minimum has been reported to have many different properties to the previous one, such as lower magnetic field strength ($\sim -15\%$), lower power ($\sim -42\%$), lower density ($\sim -17\%$) and a more complex magnetic field structure in contrast to the simple dipolar configuration expected (McComas et al., 2006, 2008; Smith & Balogh, 2008; Issautier et al., 2008). In figure 4-1, we show the time evolution of the bulk ion velocity, $|v_{ion}|$, the magnitude of the magnetic field, $|B|$, and the normalised ion density, $\rho_{ion}R/R_0^2$ for all 60 days of each polar

pass. The ion density is normalised to 1 AU

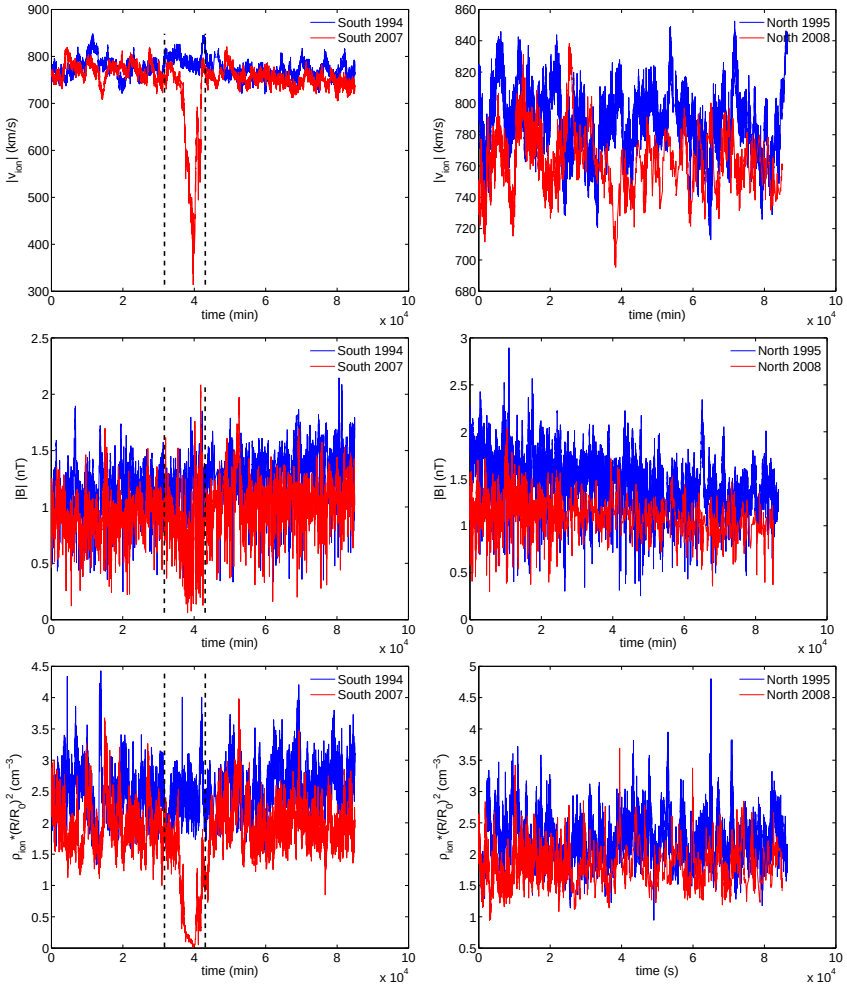

Figure 4-1: The magnetic field magnitude, bulk velocity and ion density are compared for the considered North and South 60 day intervals during the $1994-1995$ (blue) and $2007-2008$ (red) solar minimum polar passes. The density measurements are normlaized to 1 AU. The black dashed lines delimit days $30-39$ of 2007 as during this period Ulysses passed through the tail of comet McNaught for 5 days (from 3^{rd} of February, $\sim$ day 34), this data is excluded from the analysis.

The time period in February 2007, during which ULSSES passed through the tail of comet McNaught is also shown, the details of this encounter can be found in Neugebauer et al. (2007). Figure 4-2 shows the difference in power between the 2 minima North polar passes for the radial magnetic field component. A comparison of the 1994 and 2007 South passes yields a similar behaviour.

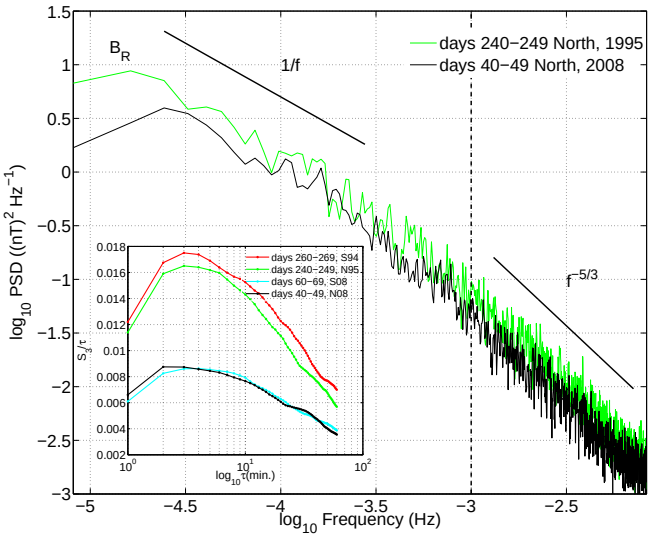

Figure 4-2: Log-log plot of the radial magnetic field component power spectra for a representative 10 day interval from each of Ulysses' minima North polar passes in 1995 and 2008. The intervals were chosen such that Ulysses was at a similar heliospheric distance in all cases. There is a noticeable decrease in power by $\sim -42\%$ between the two minima. The inset figure show S_3/τ against τ on semilog axis for all polar passes.

The inset of Figure 4-2 is a plot of the compensated third order structure functions, S_3/τ, versus $log_{10}(\tau)$ for all 4 polar passes for the radial component. If Kolmogorov's $4/5^{ths}$ law is exact, i.e. that $S_3 = -4/5\epsilon l$, where here we use the Taylor hypothesis to relate spatial scales l and temporal scales τ and the radial component is assumed to be similar to a longitudinal component, then we would expect to see a flattening of the curves over the inertial range. This relationship holds for hydrodynamic turbulence and in the limit of infinite Reynolds number, and indeed Gagne et al. (2004) show the convergence to $4/5^{ths}$ of compensated $S_{3,max}$ with increasing Reynolds number for different types of flow (grid turbulence, jet and ONERA) with known energy dissipation rates and inner and outer cascade scales. We do not know the energy dissipation rates ϵ in the solar wind here, however we do know that we are in a large Reynolds number system. Even-though, we are not in a hydrodynamic flow, we assume that the $4/5^{ths}$ law holds roughly and that ϵ is then simply proportional to the difference between S_3/τ and $4/5$. We can see in the inset to Figure 4-2, that the North and South polar passes for each minima are similar to each other yet very different between the minima.

The curves for the $2007-2008$ solar minima are a factor ~ 2 below the curves for the $1994-1995$ minima. This implies a similar difference between the energy dissipation rates, confirming the PSD results.

4.2 Generalized Similarity

The focus of this Chapter is on *in situ* observations of fast quiet polar flows from the Ulysses spacecraft, with a homogeneous flow velocity ~ 750 km/s at heliospheric distances ~ 2 AU and which are free from large transient coronal events. We compare 10 day intervals of $\sim 13,000$ points each of one minute averaged magnetic field RTN component measurements for each polar pass. This length of data is sufficent to explore the inertial range scaling and its transition to "$1/f$" at lower frequencies. We consider days $260-269$ of 1994 and days $60-69$ of 2007 (South pole passes) and days $240-249$ of 1995 and days $40-49$ of 2008 (North pole passes). These intervals were chosen such that Ulysses was at a similar heliographic range ($\sim [2.15-2.2]$ AU) and latitude ($\sim [75-79^o]$) for all passes. In order to check the results found for the North polar pass of 1995 in Chapter 3, we also examine for each pass, six 10 day contiguous intervals encompassing these days. The details of these passes are summarised in Table 4-1.

Table 4-1: Characteristics of all Ulysses polar passes analysed here during periods of solar minima. The range of the six contiguous intervals of 10 days is given as well as the heliographic and heliospheric ranges over that time. The numbers in parenthesis under the maximum heliographic latitude indicate the day(s) upon which Ulysses passed this point. All the data is obtained from the Ulysses home page (`http://ulysses-ops.jpl.esa.int/ulysses/archive/vhm_fgm.html`).

Polar Pass	days	heliographic range (°)	heliographic latitude max.	heliospheric range (AU)
South 1994	$210-269$	$-79.17°-(-79.60°)$	$-80.22°$ $(256-257)$	$2.6141-2.2041$
North 1995	$190-249$	$74.56°-77.22°$	$80.22°$ $(212-213)$	$1.8665-2.2882$
South 2007	$10-69$	$-77.72°-(-76.24°)$	$-79.7°$ (38)	$2.5632-2.1572$
North 2008	$1-59$	$78.55°-72.34°$	$79.8°$ (14)	$1.9792-2.4146$

In order to probe the statistical properties of the fluctuations, we again use extended self-similarity and we anticipate a generalised similarity of the form

$$S_m(\tau) = S_m(\tau_0)[g(\tau/\tau_0)]^{\zeta(m)} \tag{4-1}$$

Previous work (Nicol et al., 2008; Chapman et al., 2009a) has shown this to hold for both the North and South polar passes of Ulysses' first polar pass at solar minima. We now compare all the polar passes from both solar minima observed by Ulysses for fluctuations over $\tau = 1-60$ minutes. This range easily encompasses the inertial range, which is expected to have an upper scale limit of $\tau \sim 15$ minutes. For finite datasets with non-Gaussian PDFs, these statistics can be affected by the presence of large outliers in the PDF tails. To verify the robustness of our results against any bias introduced by this source of uncertainty, the method detailed in (Kiyani et al., 2006) is used.

In Figure 4-3, we show a plot of the compensated third and fourth order structure functions, S_3/τ and S_4/τ, versus $log_{10}(\tau)$ for all 4 polar passes and components.

The structure functions are normalised here to their maximum values, i.e. $S_3 = S_3/S_{3,max}$.

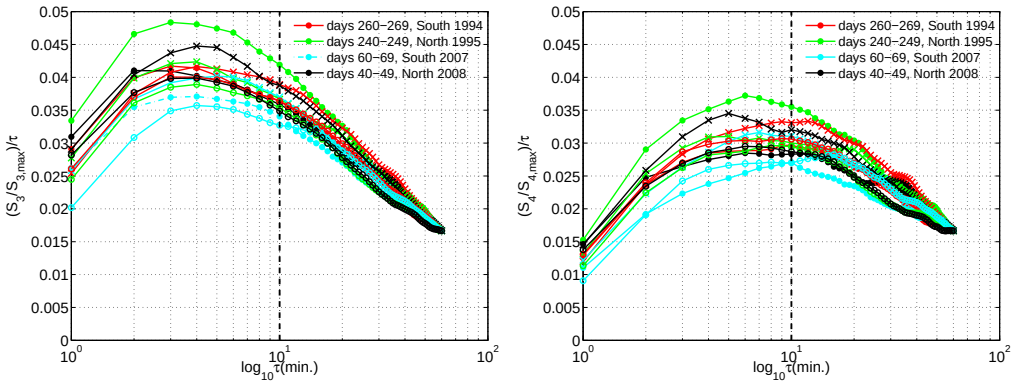

Figure 4-3: Compensated GSF S_3/τ and S_4/τ (linear scale) versus τ (logarithmic scale) for all field components for the four polar passes for intervals chosen such that Ulysses was at a similar heliospheric distance in all cases.

Generally, Figure 4-3 allows us to determine the regions where $S_3 \sim \tau$ or $S_4 \sim \tau$. In the inertial range, for $\tau \leq 10$ minutes, S_3 seems to flatten, which is evidence for $\zeta(3) = 1$. In order to further unravel this, we now examine whether the function $g(\tau/\tau_0)$ is a universal function and generic property of solar wind turbulence.

Equation 4-1 can be tested to reasonable precision for low orders $m = 1$ to 4. Structure functions become less reliable for higher order moments (e.g. Arenas & Chorin, 2006), which is why we further restrict our analysis to $m = 1 - 4$ here. In theory, to obtain $g(\tau/\tau_0)$, we simply need to invert equation 4-1. In practice, the structure function analysis shows that the IR scaling is not a good power law, we cannot therefore obtain independent measures of the $\zeta(m)$.

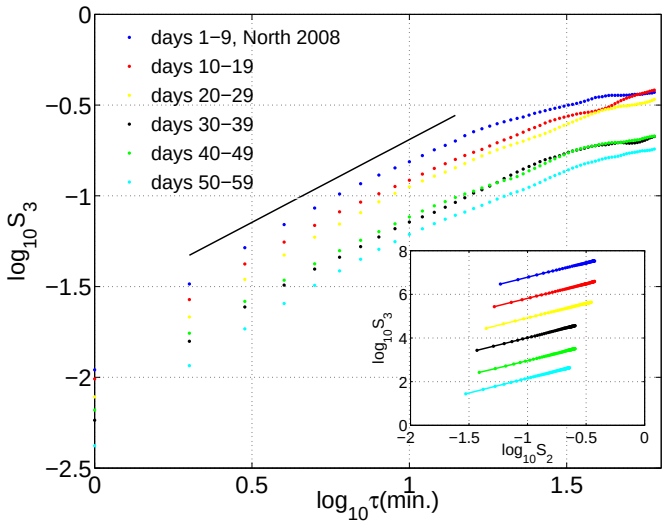

Figure 4-4: GSFs of the third order structure function S_3 against τ on loglog axis for 5 consectutive 10 intervals from the North polar pass of 2008 for $\tau = 1 - 60$ minutes. The inset figure shows ESS plots of S_3 against S_2 on loglog axis, the different intervals are shifted for clarity and the τ range shown starts at $\tau = 2$ minutes.

Figure 4-4 shows the third order structure functions for the six contiguous 10 day intervals while Ulysses was over the North solar pole in 2007. Again, we see a shift with heliospheric range, as with time, Ulysses moves further away from the Sun. However, similarly to our results for the 1995 North polar pass (Chapter 3), the functional form of the inertial range scaling remains remarkably similar between the passes. In constrast to the "$1/f$" region, which appears far more variable. The black line highlights the non-linear nature of the inertial range region. The inset to Figure 4-4 shows the corresponding ESS plots, shifted for clarity. Again, linear scaling behaviour is recovered, however it is not possible to differentiate clearly between different scaling regions using ESS, as any dependence on τ or $g(\tau)$ is now eliminated and we can only obtain ratios of scaling exponents $\zeta(3)/\zeta(m)$. In table 4-2, the exponents $\zeta(3)/\zeta(m)$, and their associated errors, obtained from linear regression fits to the ESS plots for $\tau = 2$ to $\tau = 14$ minutes are shown.

Table 4-2: $\zeta(3)/\zeta(m)$ exponents for representative 10 day intervals from the 1995 and 2007 South polar passes and the 1995 and 2008 North polar passes. During these times, the Sun was at a periods of minimum solar activity. The data show is for linear fits to ESS plots, which have been conditioned by 0.1%.

Polar Pass Date	B_i	$\frac{\zeta(3)}{\zeta(1)}$	$\pm$	$\frac{\zeta(3)}{\zeta(2)}$	$\pm$	$\frac{\zeta(3)}{\zeta(3)}$	$\pm$	$\frac{\zeta(3)}{\zeta(4)}$	$\pm$
South 1994	B_R	2.404	0.021	1.350	0.007	1	0	0.826	0.003
days $260-269$	B_T	2.262	0.026	1.303	0.006	1	0	0.849	0.003
	B_N	2.200	0.028	1.280	0.009	1	0	0.866	0.006
North 1995	B_R	2.404	0.017	1.342	0.006	1	0	0.833	0.006
days $240-249$	B_T	2.225	0.027	1.290	0.007	1	0	0.859	0.005
	B_N	2.255	0.019	1.303	0.005	1	0	0.846	0.003
South 2007	B_R	2.524	0.034	1.380	0.009	1	0	0.808	0.005
days $60-69$	B_T	2.336	0.014	1.325	0.004	1	0	0.838	0.005
	B_N	2.253	0.026	1.299	0.007	1	0	0.855	0.005
North 2008	B_R	2.299	0.028	1.314	0.008	1	0	0.840	0.006
days $40-49$	B_T	2.148	0.044	1.270	0.012	1	0	0.867	0.009
	B_N	2.260	0.037	1.308	0.010	1	0	0.842	0.003

Equation 4-1 is then manipulated to give

$$\left[\frac{S_m(\tau)}{S_m(\tau_0)}\right]^{\frac{\zeta(3)}{\zeta(m)}} = g(\tau/\tau_0)^{\zeta(3)} \tag{4-2}$$

We choose $\tau_0 = 10$ minutes as the normalization scale as this is a scale within the inertial range, yet close to the outer scale. We plot in Figure 4-5, equation 4-2 for $m = 1-4$ for all components and all minima polar passes.

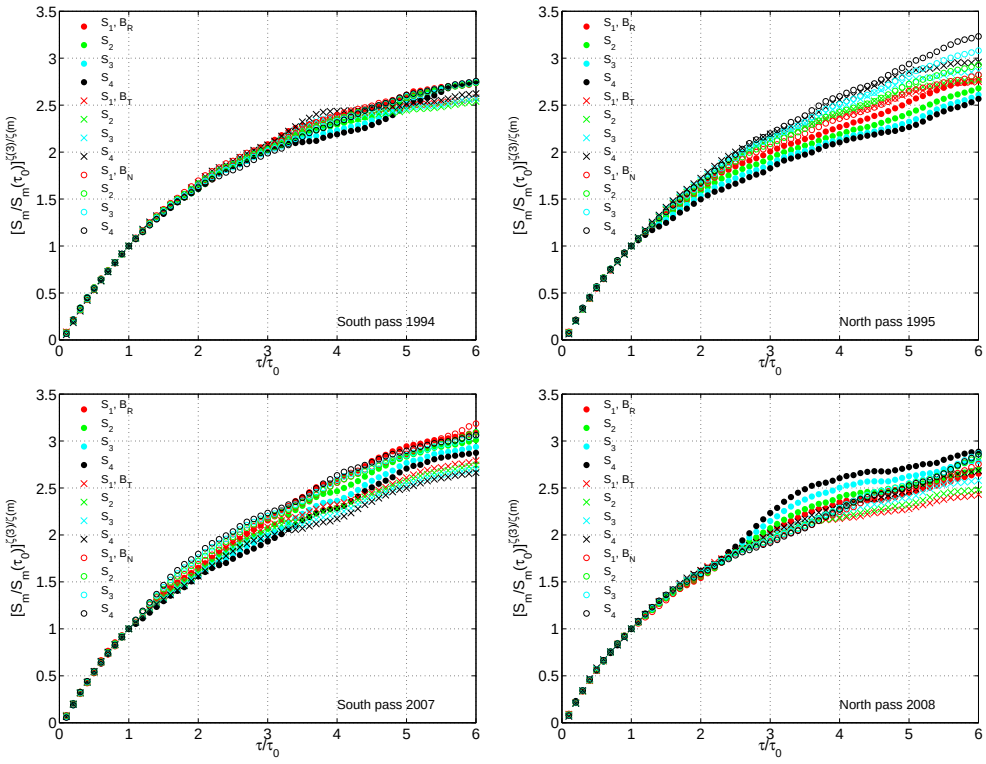

Figure 4-5: $[S_m(\tau)/S_m(\tau_0)]^{\zeta(3)/\zeta(m)}$ versus τ/τ_0 for $m = 1$ to 4 for all components are shown for representative 10 day intervals of all minima Ulysses polar passes: South 1994 (days $260 - 269$), North 1995 (days $240 - 249$), South 2007 (days $60 - 69$) and North 2008 (days $40 - 49$). $\tau_0 = 10$ minutes is chosen as this lies within the inertial range ($\sim \tau = 1 - 15$ minutes.

Figure 4-5 shows that all components and different order structure functions collapse onto the same function $g(\tau/\tau_0)^{\zeta(3)}$ within the inertial range. One can clearly see the crossover from the IR, where the curves diverge, the "$1/f^{\alpha}$" scaling has an α, which is known to vary (e.g. Nicol et al., 2008). Intriguingly, the inertial range appears more extended for the South 1994 and North 2008 polar passes, this might be linked to predominantly inwards pointing magnetic field lines, however there is no conclusive evidence as to why this should be so. We further test whether this is the same function for all polar passes by overlaying the inertial range in Figure 4-6 for the third order moment.

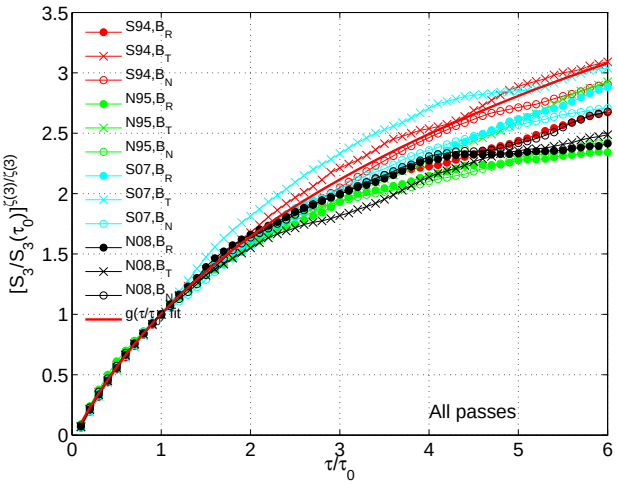

Figure 4-6: $[S_2(\tau)/S_2(\tau_0)]^{\zeta(3)/\zeta(2)}$ versus τ/τ_0 for all components are shown for a representative 10 day interval for all overlayed minima Ulysses polar passes: South 1994 (days $260-269$), North 1995 (days $240-249$), South 2007 (days $60-69$) and North 2008 (days $40-49$). Both linear (left) and loglog (right) axis are shown and the τ range shown on the the x-axis is reduced to $\tau = 1-20$ minutes.

We fit a function of the form $g(\tau/\tau_0)^{\zeta(3)} = a(\tau/\hat{\tau})^{\tau/\tau_0{}^b}$ to the curves shown in Figure 4-6 where $\tau_0 = 10$ minutes is an outer scale and $\hat{\tau} = 1$ minute is a normalisation. This functional form is suggested by finite size scaling considerations. We find a good agreement between $g(\tau/\tau_0)$ with fitting parameters $a = 0.101 \pm 0.001$ and $b = 0.10 \pm 0.01$ and the IR of the curves shown in Figure 4-6. The curves coincide to good precision for all components and polar passes, confirming the universal nature of the fluctuations, despite the different solar properties between the 2 considered solar minima.

Statistical properties of *in situ* turbulence can also be seen directly from the PDF of fluctuations (here of δB), we will now directly examine these PDFs. In Figure 4-7, we compare the functional form of the PDFs by normalizing to σ to give dimensionless axis.

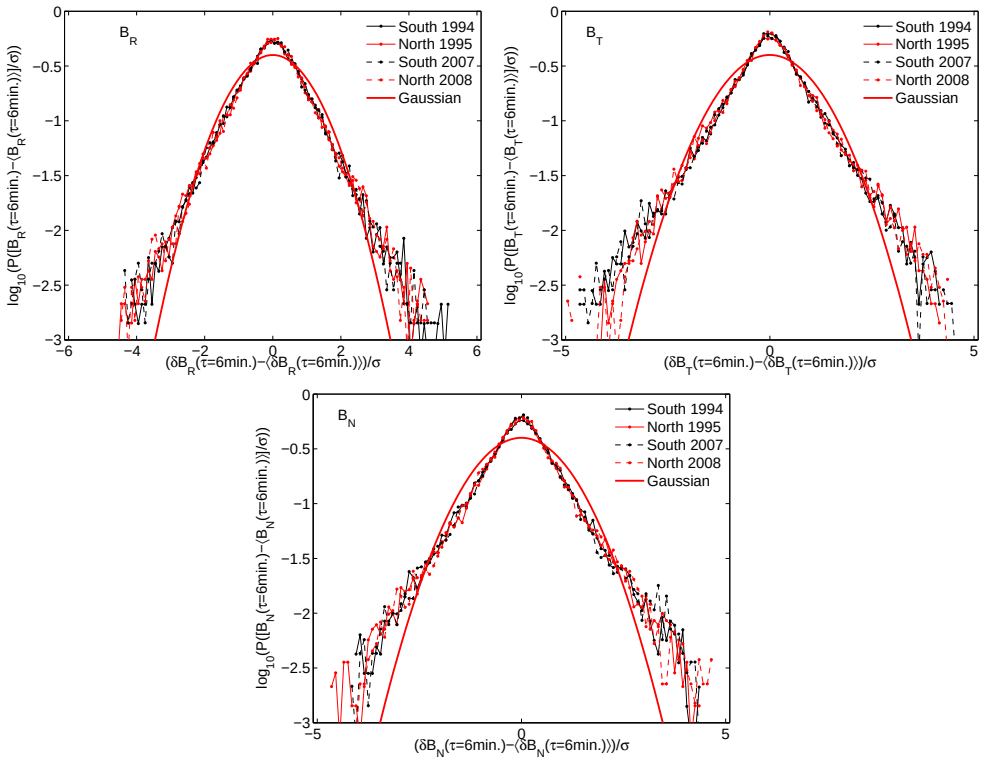

Figure 4-7: The PDFs for the RTN magnetic field component is shown for representative 10 day intervals of all minima Ulysses polar passes: South 1994 (days $260-269$), North 1995 (days $240-249$), South 2007 (days $60-69$) and North 2008 (days $40-49$). South passes are red lines, whereas North passes are black lines. Solid lines denote the solar minimum of $1994-1995$ whereas dashed lines show the minimum of $2007-2008$. Loglog axis are used and a Gaussian fit to the data is also plotted.

The normalised PDFs in Figure 4-7 overlay quite well, and do not seem to show any strong variations between the successive minima. Any deviations can be further quantified by comparing the PDFs' statistical properties such as standard deviation σ, excess kurtosis (flatness) $S_4(\tau)/S_2(\tau)^2 - 3$, and skew (asymmetry) $S_3(\tau)/S_2(\tau)^{3/2}$, signed structure functions are now used. A Gaussian distribution has an excess kurtosis of zero and a skew of zero, computing these parameters therefore allows us to estimate the deviation from Gaussian of the considered distribution. As mentioned previously, outliers in the tails of the PDFs can cause large variations in the calculation of moments. We therefore use 0.1% conditioned data for the following calculations. We find that for all quantities and passes, the skew is negligibly small, consistent with the symmetric PDFs observed in Figure 4-7. The standard deviation for the δB_R fluctuations varies from ~ 0.37

nT for both polar passes of the first solar minimum to ~ 0.3 nT for the second solar minimum passes. The δB_T and δB_N fluctuations show similar behaviour and their standard deviations vary from ~ 0.52 nT for the first minimum to ~ 0.42 nT for the second minimum. There is therefore a small, but consistent anisotropy between the radial and normal components, present for both solar passes as well as this decrease in standard deviation by about $\sim 25\%$. In contrast, the kurtosis k shows little or no variation within errors between the minima; for δB_R, $k_R \sim [1.84 - 1.97] \pm [0.38 - 0.26]$; for δB_T, $k_T \sim [1.78 - 2.40] \pm [0.14 - 0.25]$ and finally for δB_N, $k_N \sim [1.87 - 2.26] \pm [0.12 - 0.22]$. These values are also very different from 0 and clearly establish the non-Gaussian nature of the PDFs in Figure 4-7, which is a well-know feature of small scale solar wind turbulence (e.g. Marsch & Tu, 1997). Table 4-2 summarises these properties for all components and passes.

Table 4-3: Summary of standard deviation, excess kurtosis and skew for the PDFs shown in Figure 4-6 for $\tau = 6$ minutes and all polar passes and components for 0.1% conditioned data. The skew errors are negligible and are therefore not shown.

Polar Pass Date	B_i	$\sigma(nT)$	Kurtosis	$\pm$	Skew
South 1994	B_R	0.37	1.89	0.24	0.15
days $260 - 269$	B_T	0.53	2.31	0.15	-0.07
	B_N	0.53	1.87	0.12	0.04
North 1995	B_R	0.36	1.97	0.26	-0.01
days $240 - 249$	B_T	0.49	1.78	0.14	0.13
	B_N	0.53	2.32	0.15	-0.05
South 2007	B_R	0.30	1.86	0.37	0.04
days $60 - 69$	B_T	0.41	2.40	0.25	-0.11
	B_N	0.45	2.26	0.20	0.15
North 2008	B_R	0.29	1.84	0.38	0.02
days $40 - 49$	B_T	0.42	2.24	0.22	0.07
	B_N	0.39	2.14	0.25	0.18

4.3 Scaling Exponents

We can now estimate the $\zeta(m)$ scaling exponents by plotting S_m against $g(\tau/\tau_0)^{\zeta(3)}$. We consider linear regression fits to $\tau = 2-14$ minutes. The errors are again computed by fitting to $\tau = 7-9$ minutes and successively extending the fitting range by ± 1 minute until the range $\tau = 2-14$ minutes is reached. We also consider the error in the fitting parameter b by computing the ζ exponents for the different limits of b. The differences in the exponents are then considered in the error calculation. In Figure 4-8, we show the scaling exponents for a single component from a representative interval of the 1995 North polar pass.

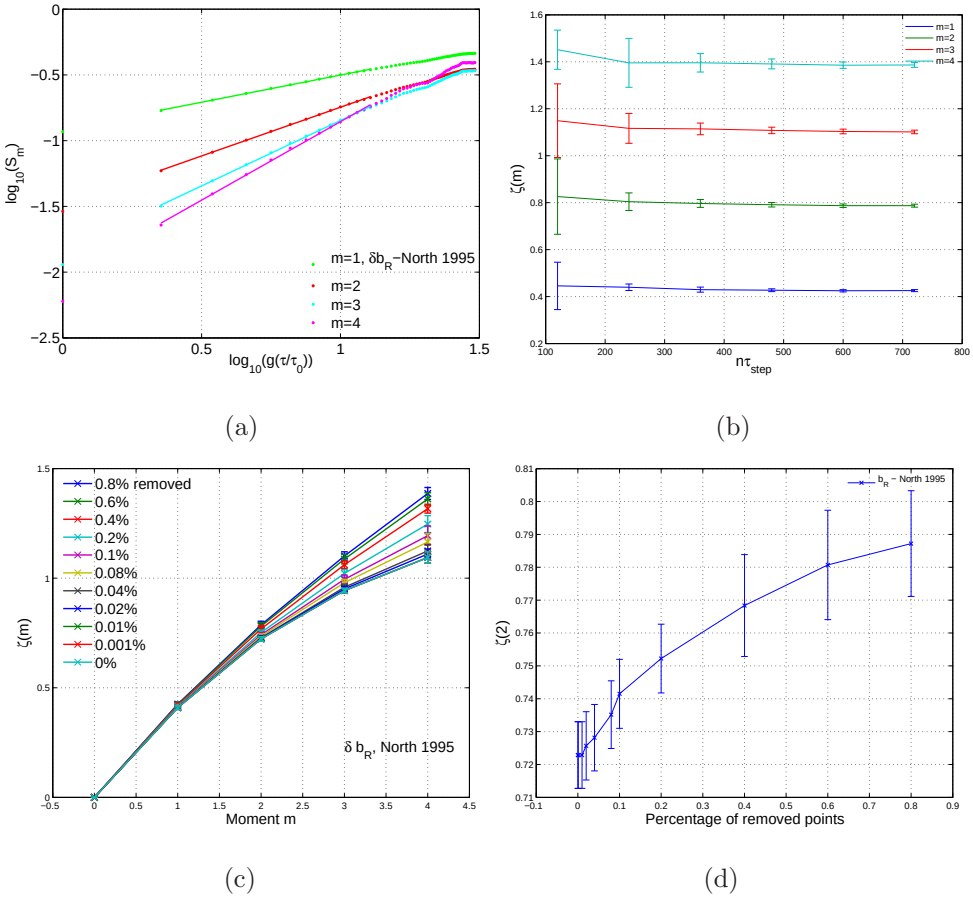

Figure 4-8: The top left panel shows S_m versus $g(\tau/\tau_0)^{\zeta(3)}$ for δb_R for days 240−249 of the 1995 North polar pass computed for $\tau = 1$ to $\tau = 60$ minutes in steps of 1 for and 0.1% conditioned data fitted to $\tau = 2$ to $\tau = 14$. The top right panel shows how the fitting range is tested by fitting between $\tau = 7$ to 9 minutes and then increasing the fitting range on either side to the next consecutive τ, up to $\tau = 2$ to $\tau = 14$ minutes. The bottom panels show the scaling exponents $\zeta(m)$ plotted as a function of moment $m = 1$ to 4 for different percentages of removed points (left panel) and $\zeta(2)$ plotted against the percentage of removed points (right panel).

The other components and other passes show similarly good linear fits to the GSFs and multifractal behaviour of the $\zeta(m)$ exponents, inferred from the non-linear beahaviour of the $\zeta(m)$ plots in Figure 4-8 and the divergence of $\zeta(2)$. We again fit a p-model to the $\zeta(m)$ curves for the 0.1% conditioned data.

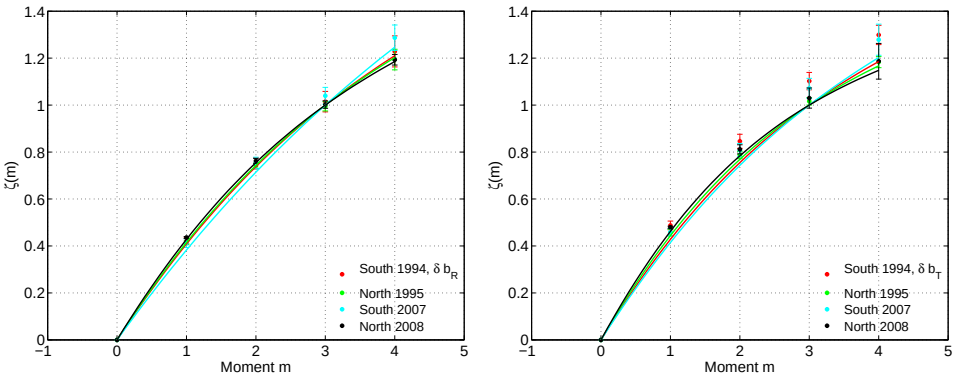

(a)

(b)

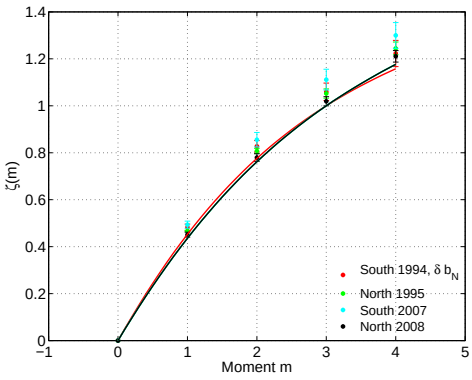

(c)

Figure 4-9: A p-model is fitted to each representative 10 day interval of all minima Ulysses polar passes: South 1994 (days $260-269$), North 1995 (days $240-249$), South 2007 (days $60-69$) and North 2008 (days $40-49$) for all three components and for 0.1% conditioned data. $\zeta(m)$ here is $\zeta(m) = \zeta(m)/\zeta(3)$

The $\zeta(m)$ curves shown in Figure 4-9 show relatively good fits to the p-model and demonstrate once again the similarity between the different passes, whose $\zeta(m)$ values are all within errors of each other. The values of p used in the p-model fit ($\zeta(m) = 1 - log_2(p^{m/3} + (1-p)^{m/3})$) are summarised in table 4-4.

Table 4-4: Summary of p-model fit parameter for the fits shown in Figure 4-9 for all components and polar passes and for 0.1% conditioned data.

Polar Pass Date	B_i	p	$\pm$
South 1994	B_R	0.81	0.04
days $260-269$	B_T	0.84	0.20
	B_N	0.87	0.09
North 1995	B_R	0.82	0.01
days $240-249$	B_T	0.86	0.03
	B_N	0.85	0.10
South 2007	B_R	0.76	0.11
days $60-69$	B_T	0.82	0.15
	B_N	0.85	0.20
North 2008	B_R	0.84	0.01
days $40-49$	B_T	0.88	0.05
	B_N	0.85	0.05

Within errors, the values reported in table 4-4 are very similar for each component. Once again, there is evidence of anisotropy as the p values for the R components are consistently lower than for the T and N components. This is similar to our observations at the end of Chapter 3, where the same variation trend between the components was noticed.

4.4 Conclusions

We have compared the statistical properties of the magnetic field components of Ulysses polar passes over 2 successive solar minima. The most recent solar minimum is found to be very different, with significantly lower power levels (decrease of $\sim -42\%$) and level of fluctuations. We use this to test for universal properties of solar wind turbulence, which is a finite size, finite R_E system. Ulysses allows us to compare quiet fast solar wind from successive polar passes at sim-

ilar heliospheric range and latitude. Furthermore, the cadence used covers the IR to "$1/f$" crossover, this is the physics of the "largest eddies" of the evolving turbulence. This physics is captured by a function $g(\tau/\tau_0)$ of the scale of the fluctuations, which is suggestive of universal behaviour however needs to be tested more widely. This is corroborated by the PDFs, which show the same functional from and by the kurtosis, which shows small or no variation between the 2 minima. In contrast, the standard deviation show a drop of $\sim 25\%$, confirming the difference in the fluctuation levels between $1994 - 1995$ and $2007 - 2008$. ESS is then a robust feature of evolving MHD turbulence. The physics of the largest coherent structures is universal.

We have also shown that the scaling exponents from this $g(\tau/\tau_0)$ fit are consistent with a multifractal p-model, which reflects the known intermittent and anisotropic nature of the solar wind.

Chapter 5

ACE results

5.1 Introduction

In the previous chapter, we used Ulysses observations to study the inertial range of turbulence in the fast solar wind emanating from the solar polar coronal holes (Nicol et al., 2008). We now focus on *in situ* solar wind velocity and magnetic field measurements in the ecliptic plane at $\sim 1AU$ and at longer timescales (lower frequencies), i.e. in the flatter "$1/f$"-like scaling range (Matthaeus & Goldstein, 1986).

The solar wind also has a background magnetic field and is therefore a highly anisotropic plasma environment (Shebalin et al., 1983; Oughton et al., 1994). The strength of this background field relative to the amplitude of the fluctuations determines whether the turbulence is "strong", i.e the amplitude of fluctuations is comparable to that of the background magnetic field (Sridhar & Goldreich, 1994; Goldreich & Sridhar, 1995) or "weak", i.e the background magnetic field is dominant (Ng & Bhattacharjee, 1997; Galtier et al., 2000). The power spectral density (PSD) of the "$1/f$" range in the interplanetary magnetic field has been extensively studied by Matthaeus & Goldstein (e.g. 1986) and at 1 AU in the magnitude of the solar wind bulk velocity $\boldsymbol{v}$ and magnetic field $\boldsymbol{B}$ by for example Burlaga & Forman (2002). There is also an extensive body of work on the Gaussian and non-Gaussian properties of PDFs of fluctuations in solar wind parameters at these very large scales (e.g. Marsch & Tu, 1997; Burlaga & Forman, 2002; Sorriso-Valvo et al., 2004; Bavassano et al., 2005) and over a wide range of heliospheric radii. Burlaga & Forman (2002) used large scale velocity fluctuations at 1 AU on timescales of one hour to a year to quantify the standard deviation, kurtosis and skewness of PDFs over these scales. Studies of the "$1/f$" range in the solar wind thus provide a unique perspective on the physics of coronal processes

over the solar cycle. For the first time we consider components of $\boldsymbol{v}$ and $\boldsymbol{B}$ defined relative to the local magnetic field, and we systematically distinguish between intervals of fast and slow solar wind at solar maximum and minimum. Here we will focus on the anisotropy of the fluctuations by using a novel decomposition technique, and will take advantage of the long timeseries available from the Advanced Composition Explorer (ACE) spacecraft to compare not only fast and slow solar wind streams but also periods of minimum and maximum solar activity.

In the inertial range, vector quantities such as *in situ* velocity and magnetic field can be resolved for components both parallel and perpendicular with respect to the background magnetic field $\boldsymbol{B}$. The duration of the timescale over which the background field is computed is important and both large scale $\boldsymbol{B}$ (Matthaeus et al., 1990) and average local $\boldsymbol{B}$ as a function of the scale of the fluctuations (Chapman & Hnat, 2007; Horbury et al., 2008) have been considered in the context of inertial range turbulence. These approaches to quantifying scaling are generic, and the focus of the present paper is to incorporate these ideas in statistical studies of the "$1/f$" range, since we anticipate that coronal processes and the transport or propagation of coronal structures will depend on orientation with respect to the background magnetic field. We will also examine $\boldsymbol{v}$ orientated coordinates in Chapter 6. The observed scaling would also be anticipated to depend quantitatively on solar cycle and to differ between fast ($\sim$ 750 km/s) or slow ($\sim$ 350km/s) solar wind streams. We will perform generalised structure function analysis (GSF) on datasets spanning these intervals in order to quantify the scaling properties of the magnetic and velocity field fluctuations both parallel and perpendicular to the background magnetic field $\boldsymbol{B}$.

The location of the spectral breakpoint between the inertial and "$1/f$" ranges differs in fast and slow streams (Horbury et al., 2005; Bruno & Carbone, 2005), presumably because at a given heliocentric distance the turbulence in the slow solar wind has had more time to develop than in the fast solar wind. Furthermore, the crossover between IR and "$1/f$" is much clearer in fast than in slow solar wind. Here, we will see that projecting velocity and magnetic field parallel and perpendicular to $\boldsymbol{B}$ provides a clear indicator of where this crossover occurs. We compare the position of this breakpoint in fast and slow solar wind streams and

at periods of maximum and minimum solar activity. We first see that the PSDs of the vector components of the velocity $\boldsymbol{v}$ and magnetic field $\boldsymbol{B}$ suggest anisotropy in the "$1/f$" range. We then decompose $\boldsymbol{v}$ and $\boldsymbol{B}$ into parallel and perpendicular fluctuations with respect to the local background magnetic field $\boldsymbol{B}$. For the simple case of quiet fast solar wind, we compare the PDFs of the fluctuations to see which components may or may not share the same underlying generating process. For completeness, we also consider the PDF for the density fluctuations $\delta\rho$. We compare the GSFs for fast and slow solar wind at solar maximum and minimum. Finally, using the GSFs, we obtain values for the scaling exponents in the "$1/f$" range and find that these are clearly distinct for $\delta v_{\parallel,\perp}$ and $\delta b_{\parallel,\perp}$.

5.2 The Datasets

The advanced composition explorer (ACE) spacecraft (Stone et al., 1998) orbits the Lagrangian point sunwards of the earth ($\sim$ 1AU). For the present analysis we study plasma parameters (magnetic field $\boldsymbol{B}$ and velocity $\boldsymbol{v}$) averaged over 64 seconds from the MAG/SWEPAM teams (Smith et al., 1998; McComas et al., 1998a): for the year 2007, representative of a period of minimum solar activity; and for the year 2000, which was a period of maximum solar activity. This provides datasets of $\sim 4.8 \times 10^5$ samples per year. In order to separate fast and slow solar wind behaviour yet still preserve a dataset with sufficient points to perform GSF to explore the "$1/f$" dynamic frequency range, we divide the datasets into intervals ($\geq$ 6000 points or 4.5 days) of fast and slow streams, where the cut-off between fast and slow is taken at 450 km/s (e.g. Horbury et al., 2005). These intervals then form one long fast solar wind dataset of $\sim 7.4 \times 10^4$ points, and one long slow solar wind dataset of $\sim 1.4 \times 10^5$ points for the year 2007 and a fast dataset of $\sim 4.1 \times 10^4$ points and a slow dataset of $\sim 1.1 \times 10^5$ points for the year 2000. To evaluate spectral properties, we apply Fourier techniques to the original continuous intervals of fast and slow solar wind. When we perform statistical analysis using the probability density functions (PDFs) of fluctuations in section 3, each dataset is treated as a single ensemble. As we preserve the

time indicators for the data, the pairs of datapoints are always drawn from within continuous intervals of fast or slow streams.

We first provide an overview of the "$1/f$" range of these data intervals by plotting the power spectral density $F(f)$ of the components of $\boldsymbol{v}$ and $\boldsymbol{B}$ in the RTN coordinate system. Generally, for a signal $x(t)$ of length N, the power spectrum $F(f)$ from the fast Fourier transform (FFT) to frequency space is given by

$$F(f) = \frac{1}{N} \mid \sum_{t=1}^{N} x(t) e^{-2i\pi(t-1)(f-1)/N} \mid^2 \tag{5-1}$$

for a range of frequencies $f = \frac{n}{Nf_s}$ where $n = [0 : N/2]$ and f_s is the sampling frequency. We take our original intervals of fast and slow solar wind and truncate (or cut) them such that they all have the same length of 6000 datapoints. Each interval is then split up into windows of $2^{12} = 4096$ points with a 50% overlap on the previous window. A Hamming window is applied to each of these sub-intervals and the FFT is computed. An average is then taken of these sub-interval FFTs to obtain the power spectrum for each interval. The power spectra for all intervals are then averaged to obtain the PSDs for fast and slow solar wind at both solar maximum and minimum. At lower frequencies, the magnetic field power spectrum $F(f) \sim f^{\alpha}$ shows a spectral slope $\alpha \sim -1$. Plotting $F(f)/f^{\alpha},\ \alpha = -1$ should therefore give a horizontal line (on average) if $\alpha \sim -1$. These plots are known as compensated power spectra and are shown for the various solar wind conditions in Figure 5-1.

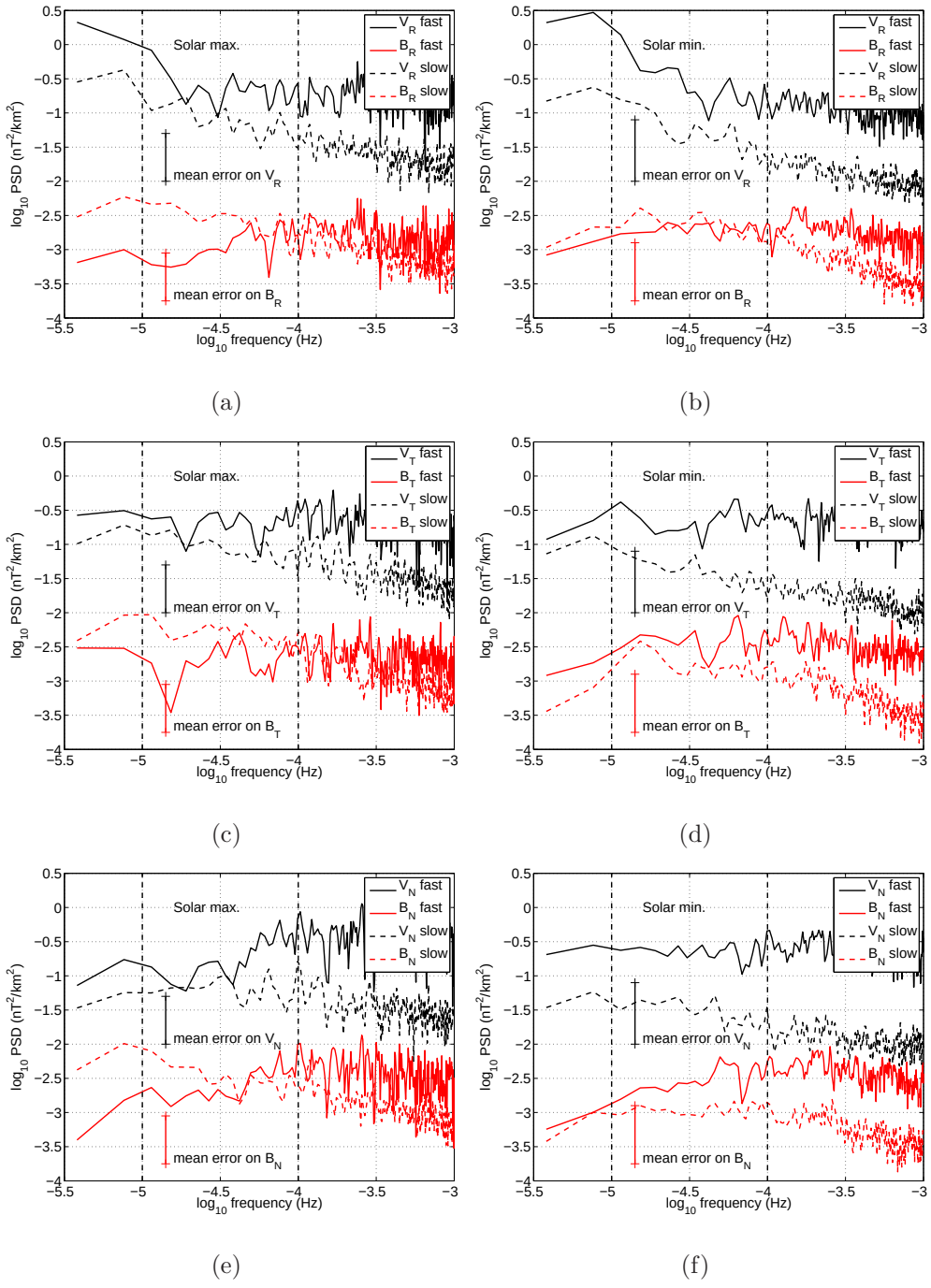

Figure 5-1: Compensated power spectral density $F(f)/f^{\alpha}$, $\alpha = -1$ for velocity and magnetic field fluctuation components in the RTN coordinate system for the frequency range $10^{-5.5} - 10^{-3}$Hz. Results for the fast (continous line) and slow (dashed line) are displayed separately. The dotted vertical lines delimit the frequency range $10^{-5} - 10^{-4}$Hz; this is expected to lie within the "$1/f$" range, with the breakpoint between the inertial and "$1/f$" ranges $\sim 10^{-4}$Hz (Marsch & Tu, 1990; Horbury et al., 1996a). The three panels on the left-hand side are for solar maximum, while the right-hand side is solar minimum. The errors are found by considering one standard deviation of the datasets over which the averages are taken.

Figure 5-1 covers the expected region of transition in the spectral index of $\boldsymbol{v}$ and $\boldsymbol{B}$ between the IR and "$1/f$" frequency ranges. However it is difficult to tell precisely whether, for example, the PSD behaviour between 10^{-5}Hz and 10^{-4}Hz really is "$1/f^{\alpha}$, $\alpha = 1$", particularly in the slow solar wind. It also evident from Figure 5-1 that in some cases in the "$1/f^{\alpha}$" range α varies with the solar cycle and with solar wind speed, and that for both $\boldsymbol{v}$ and $\boldsymbol{B}$ the α can vary from one component to another, and between $\boldsymbol{v}$ and $\boldsymbol{B}$. This implies anisotropy in the fluctuations and distinct scaling between $\boldsymbol{v}$ and $\boldsymbol{B}$.

From a statistical point of view, let us now characterize this anisotropy by decomposing the velocity (or magnetic) field fluctuations into parallel and perpendicular components relative to the background magnetic field. We adopt the Taylor hypothesis (Taylor, 1938) to relate spatial and temporal scales and fluctuations over a time lag τ in the velocity (or magnetic field) vector components, defined as $\delta\boldsymbol{v}(t,\tau) = \boldsymbol{v}(t+\tau) - \boldsymbol{v}(t)$. A vector average for the magnetic field direction $\hat{\boldsymbol{b}}(t,\tau) = \overline{\boldsymbol{B}}/|\overline{\boldsymbol{B}}|$ is formed from a vector sum $\overline{\boldsymbol{B}}(t)$ of all the observed vector $\boldsymbol{B}$ values between $t-\tau/2$ and $t+3\tau/2$. It follows that in computing fluctuations over τ, the background field is averaged over $\tau' = 2\tau$, which then defines the minimum (Nyquist) interval necessary to capture wavelike fluctuations (Chapman & Hnat, 2007). Using this definition of $\hat{\boldsymbol{b}}$, the inner product

$$\delta v_{\parallel} = \delta\boldsymbol{v}\cdot\hat{\boldsymbol{b}} = \delta v_R\hat{b}_R + \delta v_T\hat{b}_T + \delta v_N\hat{b}_N \tag{5-2}$$

vanishes for fluctuations which generate a velocity displacement that is purely perpendicular to the background magnetic field $\overline{\boldsymbol{B}}$ as defined. The perpendicular fluctuation amplitude is then obtained from

$$\delta v_{\perp} = \sqrt{\delta\boldsymbol{v}\cdot\delta\boldsymbol{v} - \left(\delta\boldsymbol{v}\cdot\hat{\boldsymbol{b}}\right)^2} \tag{5-3}$$

We use these definitions to construct differenced timeseries $\delta v_{\perp}(t,\tau)$, $\delta b_{\perp}(t,\tau)$, $\delta v_{\parallel}(t,\tau)$ and $\delta b_{\parallel}(t,\tau)$ over a range of τ intervals within the "$1/f$" range, that is τ from a few hours up to a day.

We note that our definition of the perpendicular component is a scalar unsigned quantity, this can be thought of as an angle averaged component in the plane perpendicular to the background field $\boldsymbol{B_0}$. This relies on the assumption of isotropy in this plane. In order to test this we decompose the perpendicular fluctuations

into two signed orthogonal components and compare their PDFs. We first define two orthogonal unit vectors in the perpendicular plane as

$$\hat{\boldsymbol{e}}_{\perp\mathbf{1}} = \frac{\hat{\boldsymbol{b}} \times \langle \boldsymbol{u} \rangle}{|\hat{\boldsymbol{b}} \times \langle \boldsymbol{u} \rangle|} \tag{5-4}$$

and

$$\hat{\boldsymbol{e}}_{\perp\mathbf{2}} = \frac{\hat{\boldsymbol{b}} \times \hat{\boldsymbol{e}}_{\perp\mathbf{1}}}{|\hat{\boldsymbol{b}} \times \hat{\boldsymbol{e}}_{\perp\mathbf{1}}|} = \frac{\hat{\boldsymbol{b}} \times (\hat{\boldsymbol{b}} \times \langle \boldsymbol{u} \rangle)}{|\hat{\boldsymbol{b}} \times (\hat{\boldsymbol{b}} \times \langle \boldsymbol{u} \rangle)|} \tag{5-5}$$

where $\langle \boldsymbol{u} \rangle$ is the mean velocity over the total considered time period and $\hat{\boldsymbol{b}}$ is a unit vector in the direction of the local background magnetic field as defined previously. Velocity fluctuations along these axis are then formed by the following inner products

$$\delta v_{\perp 1} = \delta \boldsymbol{v} \cdot \hat{\boldsymbol{e}}_{\perp\mathbf{1}} \tag{5-6}$$

and

$$\delta v_{\perp 2} = \delta \boldsymbol{v} \cdot \hat{\boldsymbol{e}}_{\perp\mathbf{2}} \tag{5-7}$$

These quantities are computed for the entire τ range examined and normalised by their mean and standard deviation in order to be compared. Figure 5-2 shows the corresponding PDF on semilog axis.

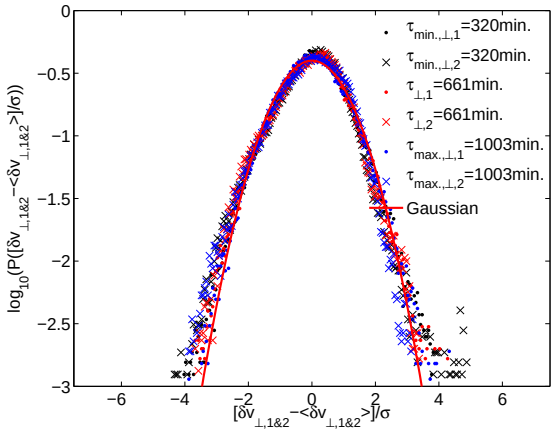

Figure 5-2: Perpendicular velocity fluctuations $\delta v_{\perp 1}$ ("$\cdot$") and $\delta v_{\perp 2}$ ("$\times$") in the fast solar wind at solar minimum for the "$1/f$" range. For clarity, plots for only three representative values of τ are shown for each component, whereas the fitted curve is computed using all the τ intervals between 320 and 1003 minutes. A Gaussian fit to the normalised PDF curves for both $\delta v_{\perp 1}$ and δv_{perp2} is shown using semilog y axes.

Figure 5-2 shows that any anisotropy present in the PDFs of the components in the perpendicular plane is weak. The PDFs have the same functional form,

justifying our use of a scalar, unsigned perpendicular fluctuation as defined by equation 5-3. The fluctuations can also be seen to be non-Gaussian, this is particularly obvious when we consider the behaviour of the PDF tails, which are asymmetric and show considerable scatter.

5.3 PDF Analysis

We first examine the PDFs of these fluctuations and explore their possible functional forms. In order to compare the different fluctuations, we recall that the PDFs can be renormalised using (e.g. Greenhough et al., 2002a)

$$P[(y- < y >)] = \sigma^{-1} P[\sigma^{-1}(y- < y >)] \tag{5-8}$$

where $< \cdots >$ denotes the ensemble mean and σ is the standard deviation of the distribution. From a statistical point of view, where fluctuations arise from a single physical process, rescaling of PDFs using equation 5-8 leads to the "collapse" of the PDFs for the different τ onto a single function that characterizes the underlying process (e.g. Greenhough et al., 2002b; Dudson et al., 2005; Dendy & Chapman, 2006; Dewhurst et al., 2008; Hnat et al., 2008). Let us apply this technique to parallel and perpendicular velocity and magnetic field fluctuations in the fast solar wind at solar minimum. Figure 5-3 shows that the PDFs for the $\delta v_{\parallel}$ and $\delta v_{\perp}$ components each collapse onto single curves that are distinct from each other. The PDF for $\delta v_{\parallel}$ is asymmetric about $\delta v_{\parallel} = 0$, and we have investigated this asymmetry by sorting the fluctuations with respect to the sign of δv_R into $\delta v_{\parallel}^{+}$ and $\delta v_{\parallel}^{-}$. The resulting GSFs and scaling exponents display the same fractal characteristics as $\delta v_{\parallel}$, implying that $\delta v_{\parallel}^{+}$ and $\delta v_{\parallel}^{-}$ arise from the same physical process.

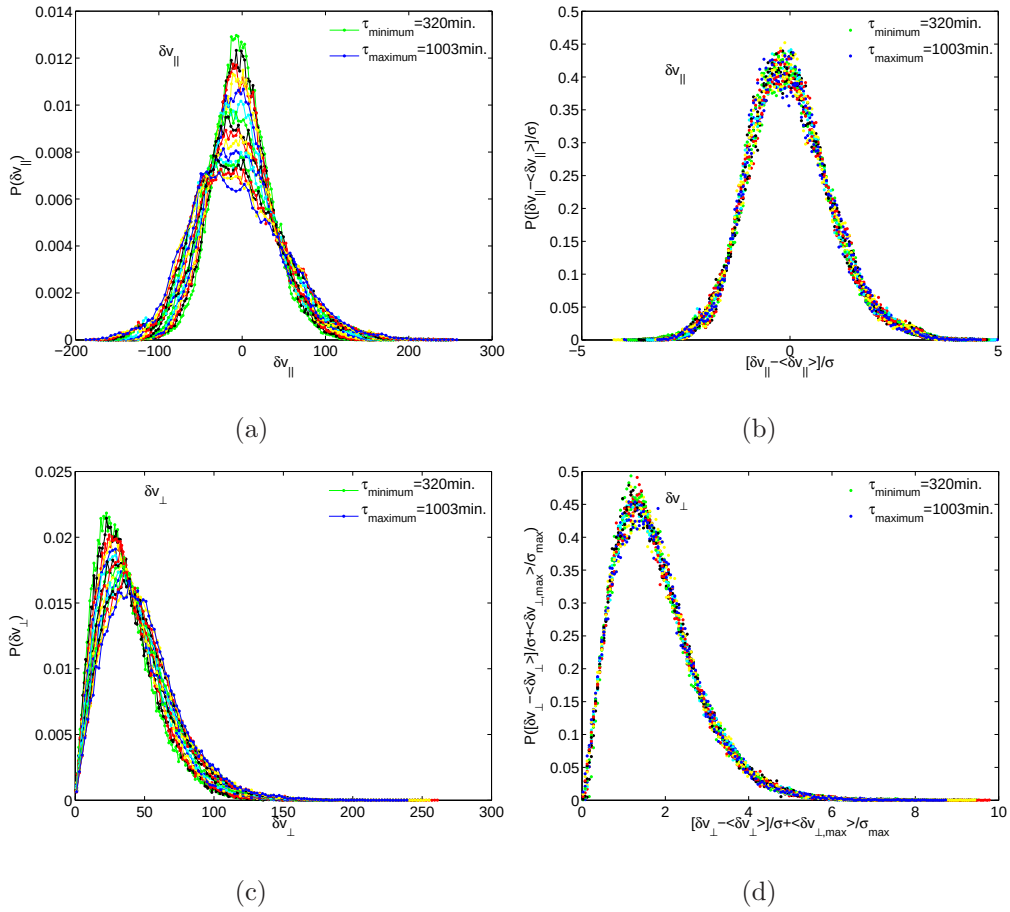

Figure 5-3: Parallel (upper) and perpendicular (lower) velocity fluctuations $\delta v_{\parallel,\perp}$ in the fast solar wind at solar minimum for the "$1/f$" range. The left panels show the PDFs of raw fluctuations sampled across intervals τ between 320 and 1003 minutes. The right panels show the same curves normalised using equation 5-8.

Figure 5-4 shows that the PDFs for $\delta b_{\parallel}$ and $\delta b_{\perp}$ each collapse approximately onto single curves that are distinct from each other. The curve for $\delta b_{\parallel}$ is distinct from that for $\delta v_{\parallel}$ and the PDF has stretched exponential tails, which implies that these fluctuations may originate in multiplicative or fractionating process (Frisch & Sornette, 1997). The curves for $\delta b_{\perp}$ and $\delta v_{\perp}$ look remarkably similar and we will explore this later.

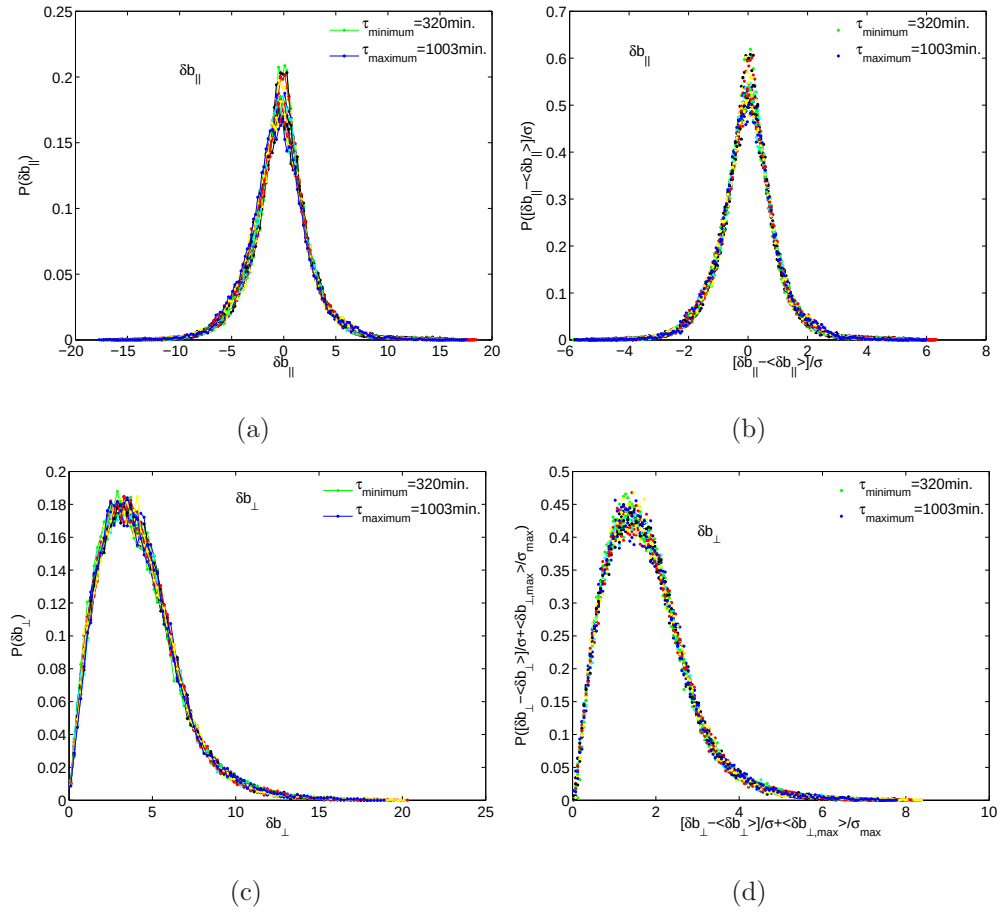

Figure 5-4: Parallel (upper) and perpendicular (lower) magnetic field fluctuations $\delta b_{\parallel,\perp}$ in the fast solar wind at solar minimum for the "$1/f$" range. The left panels show the PDFs of raw fluctuations sampled across intervals τ between 320 and 1003 minutes. The right panels show the same curves normalised using equation 5-8.

The functional forms of these distributions are investigated in Figure 5-5. A Gaussian distribution (Wadsworth, 1998)

$$\frac{1}{\sigma\sqrt{2\pi}} e^{\frac{-(x-\mu)^2}{2\sigma^2}} \tag{5-9}$$

approximately fits the normalised PDFs of the $\delta v_{\parallel}$ fluctuations in the "$1/f$" range shown in Figure 5-3 with the following fitting parameters and 95% confidence bounds: $\mu = 0 \pm 0.003$ (mean) and $\sigma = 1 \pm 0.002$ (standard deviation). Note that since we normalised the curves to μ and σ, an exact fit would have been $\mu = 0$ and $\sigma = 1$ here. In contrast, the normalised PDFs of the $\delta v_{\perp}$ fluctuations in the "$1/f$" range also shown in Figure 5-3 are clearly not Gaussian. Here they are fitted with

three different heavy-tailed distributions: gamma (Wadsworth, 1998) defined by

$$f(x|a,b) = \frac{1}{b^a \gamma(a)} x^{a-1} e^{-x/b} \tag{5-10}$$

with fitting parameters from maximum likelihood estimates $a = 3.083 \pm 0.008$ and $b = 0.580 \pm 0.002$ where the errors are from 95% confidence bounds; the generalised extreme value PDF (Wadsworth, 1998) defined by

$$f(x|k,\mu,\sigma) = \frac{1}{\sigma} exp\left(-\left(1 + k\frac{(x-\mu)}{\sigma}\right)^{\frac{1}{k}}\right)\left(1 + k\frac{(x-\mu)}{\sigma}\right)^{-1-\frac{1}{k}} \tag{5-11}$$

with fitting parameters $k = 0.027 \pm 0.001$ (shape), $\mu = 1.324 \pm 0.002$ (location) and $\sigma = 0.764 \pm 0.001$ (scale). The generalised extreme value (gev) distribution combines three simple extreme value distributions, types I, II and III, in a single form. The value of the shape parameter k determines the type of the distribution. In the case $k \to 0$, the distribution is type I, or inverse Gumbel and equation 5-11 simplifies to

$$f(x|k,\mu,\sigma) = \frac{1}{\sigma} exp\left(-exp\left(-\frac{(x-\mu)}{\sigma}\right) - \frac{(x-\mu)}{\sigma}\right) \tag{5-12}$$

This distribution corresponds to a maximum extreme value distribution or the limiting distribution of samples obtained be repeatedly selecting the maximum from an ensemble of events, which in turn, have a distribution with finite variance, e.g. Gaussian or exponential (Sornette, 2004). Types II ($k > 0$) and III ($k < 0$) of the generalised extreme value distribution correspond respectively to Fréchet and inverse Weibull distributions. Finally a lognormal distribution (Wadsworth, 1998) defined by

$$f(x|\mu,\sigma) = \frac{1}{x\sigma\sqrt{2\pi}} e^{\frac{-(lnx-\mu)^2}{2\sigma^2}} \tag{5-13}$$

is fitted with parameters $\mu = 0.410 \pm 0.001$ and $\sigma = 0.625 \pm 0.001$. It can be seen from Figure 5-5 that either the gamma distribution or the inverse Gumbel give good fits to the PDF of the $\delta v_\perp$ fluctuations. Physically, the gamma distribution is related to the PDF of waiting times of events generated by a Poisson process (Wadsworth, 1998), as noted for the analysis of plasma turbulence by Graves et al. (2002).

Turning to the magnetic field, Figure 5-5 shows that, unlike $\delta v_\parallel$, for $\delta b_\parallel$ there is a strong departure from the Gaussian distribution in the tails of the PDF, which

are closer to stretched exponential, reminiscent of turbulence. The PDFs of the $\delta b_\perp$ fluctuations in the "$1/f$" range are fitted with the same three heavy-tailed distributions as $\delta v_\perp$: gamma with fitting parameters from maximum likelihood estimates $a = 3.047 \pm 0.008$ and $b = 0.585 \pm 0.002$ where the errors are from 95% confidence bounds; generalised extreme value with fitting parameters $k = 0.017 \pm 0.002$, $\mu = 1.325 \pm 0.002$ and $\sigma = 0.770 \pm 0.001$; and lognormal with fitting parameters $\mu = 0.406 \pm 0.001$ and $\sigma = 0.633 \pm 0.001$. There is little difference between the raw and collapsed PDFs, as $\delta v = b_{\parallel,\perp}$ is closer to "$1/f$" scaling.

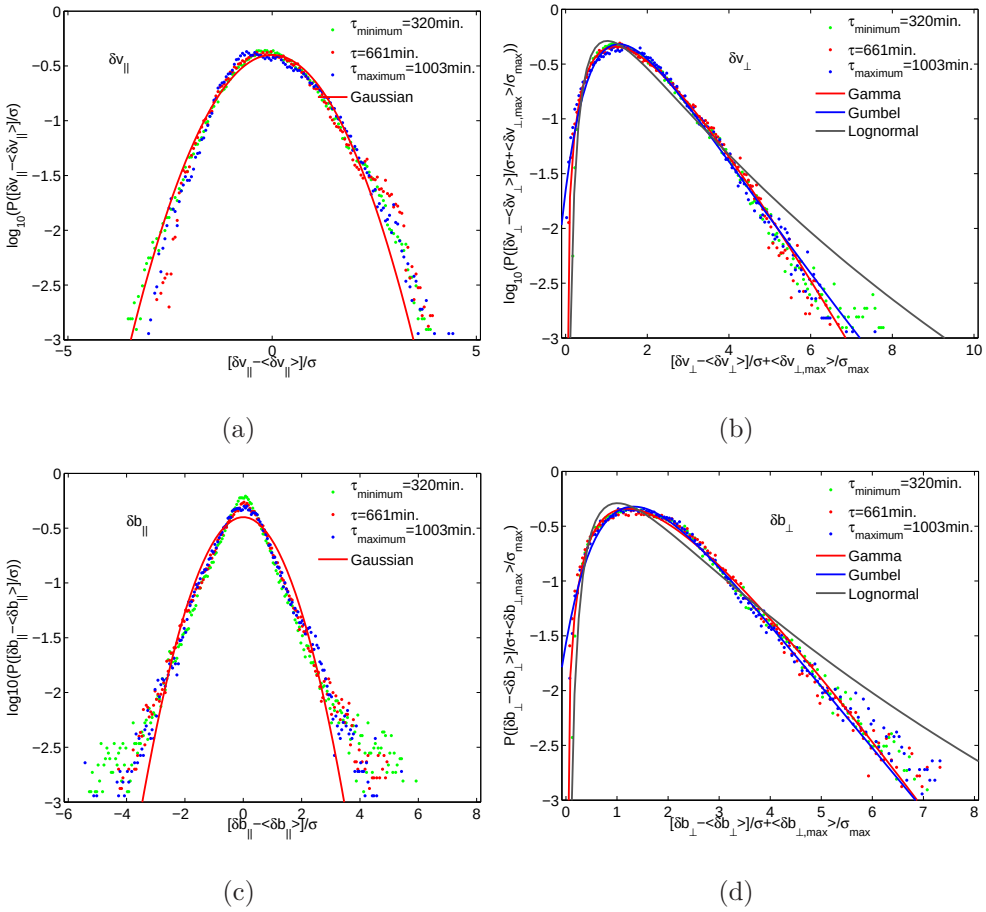

Figure 5-5: Parallel and perpendicular velocity and magnetic field fluctuations $\delta v_{\parallel,\perp}$ and $\delta b_{\parallel,\perp}$ in the fast solar wind at solar minimum for the "$1/f$" range. For clarity, plots for only three representative values of τ are shown for each component, whereas the fitted curves are computed using all the τ intervals between 320 and 1003 minutes. The left panels show a Gaussian fit to the normalised PDF curves for both $\delta v_{\parallel}$ (upper) and $\delta b_{\parallel}$ (lower) using semilog y axes. The right panels show the normalised curves $\delta v_{\perp}$ (upper) and $\delta b_{\perp}$ (lower) fitted with three different distributions gamma (red); Gumbel (blue); and lognormal (grey) on semilog y axis. For the perpendicular components, the renormalisation with μ means that the PDFs are shifted so that they are centered on zero, however the gamma distribution can only have positive arguments. It is therefore necessary to shift the PDFs by $< \delta v_{\perp,max} > /\sigma_{max}$.

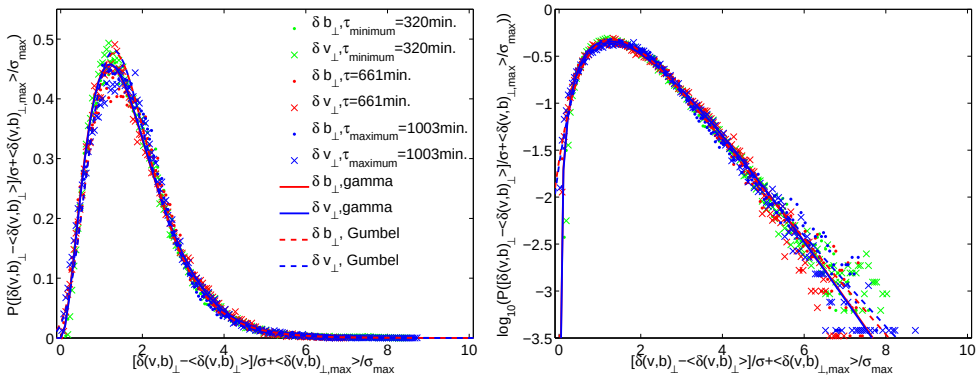

(a) (b)

Figure 5-6: Perpendicular magnetic field fluctuations $\delta b_\perp$ ("$\cdot$") and $\delta v_\perp$ ("$\times$") in the fast solar wind at solar minimum for the "$1/f$" range. The gamma and Gumbel distributions are used to fit the normalised curves for $\delta b_\perp$ (red) and $\delta v_\perp$ (blue). Only three representative values of τ are shown for each component, whereas the fitted curves are computed using all the τ intervals. The left panel shows the PDFs on linear axis, whereas the right panel shows the normalised curves on a semilog y axis.

As we have seen, $\delta b_\perp$ and $\delta v_\perp$ appear to be strongly similar in their statistics and Figure 5-6 overlays the normalised PDFs for $\delta b_\perp$ and $\delta v_\perp$ in the fast quiet solar wind. We see that they are almost identical and also not simply Maxwellian (i.e. Gaussian process). A possible interpretation is that both sets of fluctuations have the same physical process at their origin.

For completeness, we also examine the ion density fluctuations $\delta\rho$ in the fast quiet solar wind. From Matthaeus et al. (2007), one might expect these to show similar scaling behaviour to the $\delta b_{\parallel,\perp}$ fluctuations, however in Figure 5-7 we see that this is not the case. The density PDFs have very sharp peaks with extended tails and are asymmetric. The rescaling collapse works well at the centre of the PDFs, but not towards the tails. This is suggestive of some scaling process in the small-scale density fluctuations. Indeed (Carbone et al., 2009) use density-weighted Elsässer variables from Ulysses measurements of fast solar wind to show the effect of compressibility and low amplitude density flucutations on solar wind scaling laws for temporal ranges of a few minutes to a day.

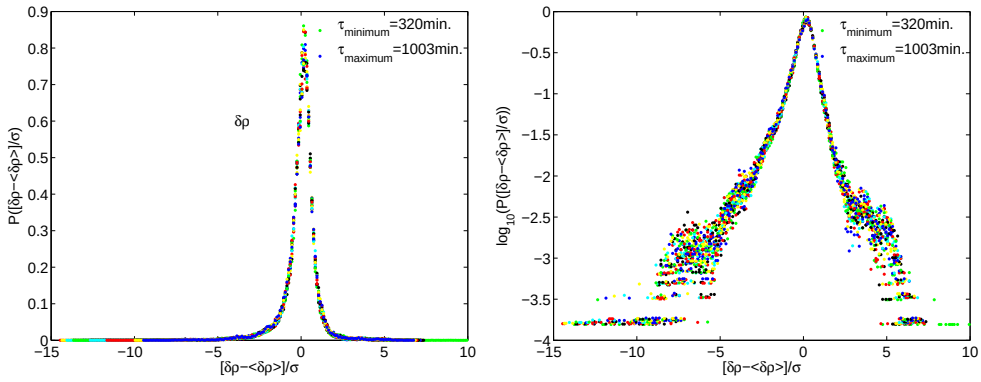

(a) (b)

Figure 5-7: Ion density fluctuations $\delta\rho$ in the fast solar wind at solar minimum for the "$1/f$" range. The left panel shows the PDFs of raw fluctuations sampled across intervals τ between 320 to 1003 minutes normalised using equation 5-8. The right panel shows the normalised curves on a semilog y axis.

To conclude this section, let us summarise our analysis of the PDFs of fluctuations in the fast quiet solar wind. Figures 5-3 and 5-4 (right-hand sides) show scaling collapse for $\delta v_{\parallel,\perp}$ and $\delta b_{\parallel,\perp}$. Figure 5-5 (left-hand side) shows that $\delta v_{\parallel}$ and $\delta b_{\parallel}$ are distinct. This is manifest in both a different functional form of the rescaled PDFs and different scaling of the moments, which we discuss next. In particular, $\delta b_{\parallel}$ is nearly symmetric and has stretched exponential tails, consistent with a multiplicative process, whereas $\delta v_{\parallel}$ is more asymmetric and is close to Gaussian. Figure 5-6 shows that $\delta v_{\perp}$ and $\delta b_{\perp}$ have the same PDF functional form and are reasonably well fitted by the gamma and Gumbel distributions with similar fitting parameters, suggesting a common source for the fluctuations.

5.4 GSF Analysis for Comparison of Quiet Fast and Slow Streams

Scaling is again quantified by computing the generalised structure functions (GSFs) of the fluctuations. We anticipate scaling for the datasets considered here, given the indication of a "$1/f$" range in the PSDs in Figure 5-1, however power spectra alone cannot distinguish between fractal and multifractal behaviour (Chapman et al.,

2005a).

We now apply these methods to the observations. Figure 5-8 shows the GSFs up to $m = 4$ for $\delta v_{\parallel}$, $\delta v_{\perp}$, $\delta b_{\parallel}$ and $\delta b_{\perp}$ for fast and slow solar wind at solar minimum. The series is differenced over $\tau = n \times 640$ s for $n = 1$ to 160, that is for a range covering ten to 1706 minutes ($\sim$ 28 hours). The finite length of the datasets considered means that the statistics calculated for any given single ensemble can in principle be affected by the presence of large outliers, which are insufficiently numerous to be fully sampled. We check that this does not bias our results via the method of Kiyani et al. (2007), which by subtracting outliers verifies whether calculated exponents are robust against statistical fluctuations in the outliers. The raw and 0.4% conditioned GSFs are shown for comparison in Figure 5-8. For the low-order moments that we consider here, we see that the difference is small, so that the finite length of our datasets does not significantly affect our conclusions. The raw data is used for the plots of the probability densities of the fluctuations in section 3.

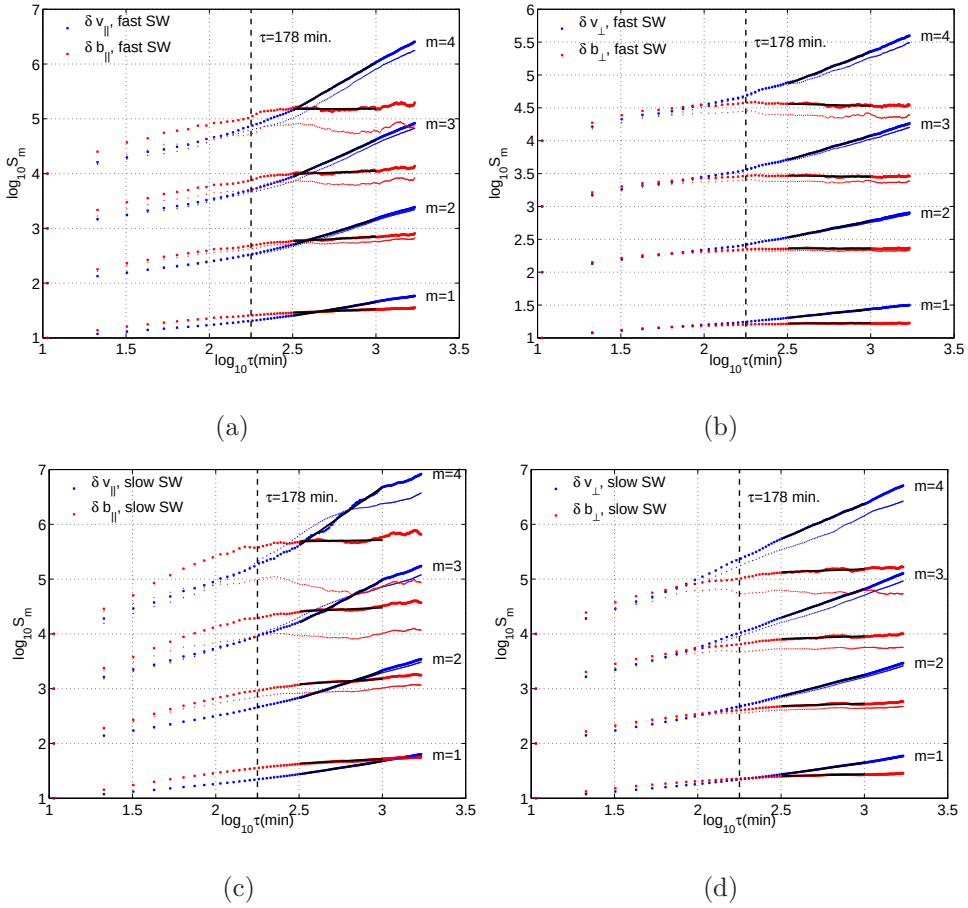

Figure 5-8: Comparison of scaling properties of fluctuations in the fast solar wind (upper) and in the slow solar wind (lower) at solar minimum in 2007. Generalised structure functions S_m are plotted on log-log axes versus sampling interval τ for $\tau = 10$ to 1706 minutes and $m = 1$ to 4. Left panels show parallel components of fluctuations in velocity (blue) and magnetic field (red); right panels show corresponding perpendicular components. The raw data is shown by "·", whereas "•" denote data which has been conditioned by 0.4% (the difference in these curves quantifies finite size effects). Linear regression fits to the "$1/f$" range over $\tau = 320$ to 1002 minutes are shown. The transition from the IR to the "$1/f$" range occurs at ~ 178 minutes and is shown by the dashed line.

Figure 5-8 is consistent with the results shown previously, namely that $\boldsymbol{v}$ and $\boldsymbol{B}$ fluctuations exhibit very different behaviour in the "$1/f$" range, which corresponds to large τ intervals. A simple self-affine noise process with PSD$\sim 1/f^{\alpha}$, $\alpha \sim 1$ would on such a plot have $\zeta(2) \to 0$ since $\alpha = 1+\zeta(2)$. If the process is fractal then $\zeta(m) = \alpha m \to 0$ for all m. Thus we see that at $\tau > 178$ min., the GSFs for $\delta b_{\parallel,\perp}$ "flatten" in the $\sim 1/f$ range, consistent with previously reported results based on the PSD (Matthaeus & Goldstein, 1986; Matthaeus et al., 2007). The

$\delta v_{\parallel,\perp}$ GSFs on the contrary steepen at $\tau > 178$ minutes, showing a scaling process and exponents distinct from those of $\delta b_{\parallel,\perp}$. These are closer to a value of $\zeta(2) \sim 1$, which, again for a simple noise process, is consistent with PSD$\sim 1/f^2$. This is what we have seen in the PDF curve renormalization of the previous section: the $\delta b_{\parallel,\perp}$ raw PDFs were close to the renormalised PDFs, since the normalization is with respect to the first two moments S_1 and S_2, which for $\delta b_{\parallel,\perp}$ vary weakly as a function of scale τ. The scaling behaviour of the process is contained in the $\zeta(m)$ exponents, given by the slopes of the GSFs. We obtain these values by linear fits to the log-log GSF plots.

Whilst these results confirm the "$1/f$" scaling of fluctuations in $\boldsymbol{B}$ on long timescales, reported previously by for example Matthaeus & Goldstein (1986), they also highlight the distinct scaling of $\boldsymbol{v}$, which we will investigate next. These GSF plots of fluctuations oriented with respect to the background field also clearly show the crossover between the IR and "$1/f$" for fast and slow solar wind. The "$1/f$" range is much shorter in the slow streams, consistent with previous observations (e.g. Bruno & Carbone, 2005; Horbury et al., 2005). The minimum value of τ that we will use for the following analysis can be seen to be greater than the breakpoint τ for both velocity and magnetic field fluctuations. For $\delta v_{\parallel}$ and $\delta b_{\parallel}$ in both fast and slow wind, the timescale τ at which the GSFs diverge is $\gtrsim \tau = 128$ minutes, the spectrally inferred breakpoint between IR and "$1/f$". In contrast, the divergence between the GSFs of $\delta v_{\perp}$ and $\delta b_{\perp}$ begins at a significantly shorter timescale $\tau \sim 100$ minutes. This is particularly apparent when one considers the higher order moments such as $m = 3,\ 4$ in Figure 5-8. It is also interesting to note that although the PDFs of $\delta v_{\perp}$ and $\delta b_{\perp}$ in the fast quiet solar wind show the same functional form (Figure 5-6), their GSF scalings are very different. This may suggest that the fluctuations $\delta v_{\perp}$ and $\delta b_{\perp}$ originate in a common coronal source, but their subsequent development differs in the evolving and expanding solar wind.

Figures 5-9 and 5-10 compare the GSFs for fast and slow solar wind streams at solar maximum (2000) and minimum (2007); for clarity only the 0.4% conditioned results are shown.

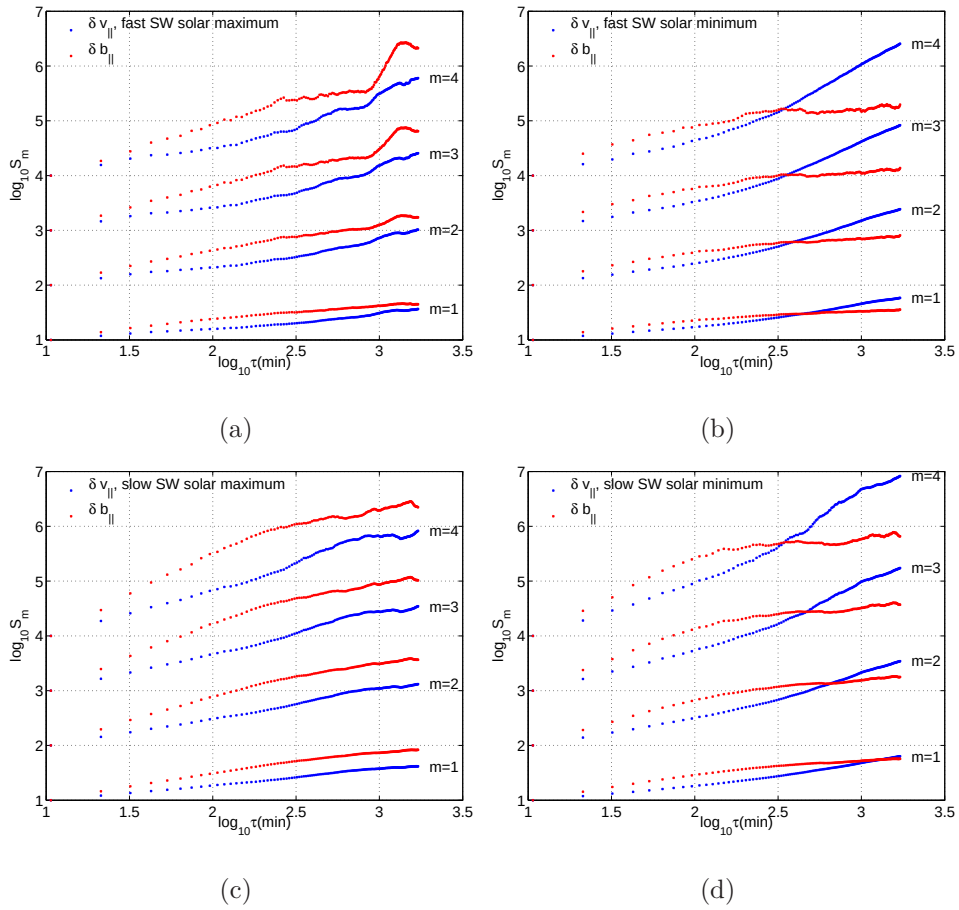

Figure 5-9: Comparison of scaling properties of parallel fluctuations between fast (upper) and slow (lower) solar wind at solar maximum (left) in 2000 and solar minimum (right) in 2007. Generalised structure functions S_m are plotted on log-log axes versus sampling interval τ for $\tau = 10$ to 1706 minutes and $m = 1$ to 4. Parallel components of fluctuations in velocity (blue) and magnetic field (red) are shown.

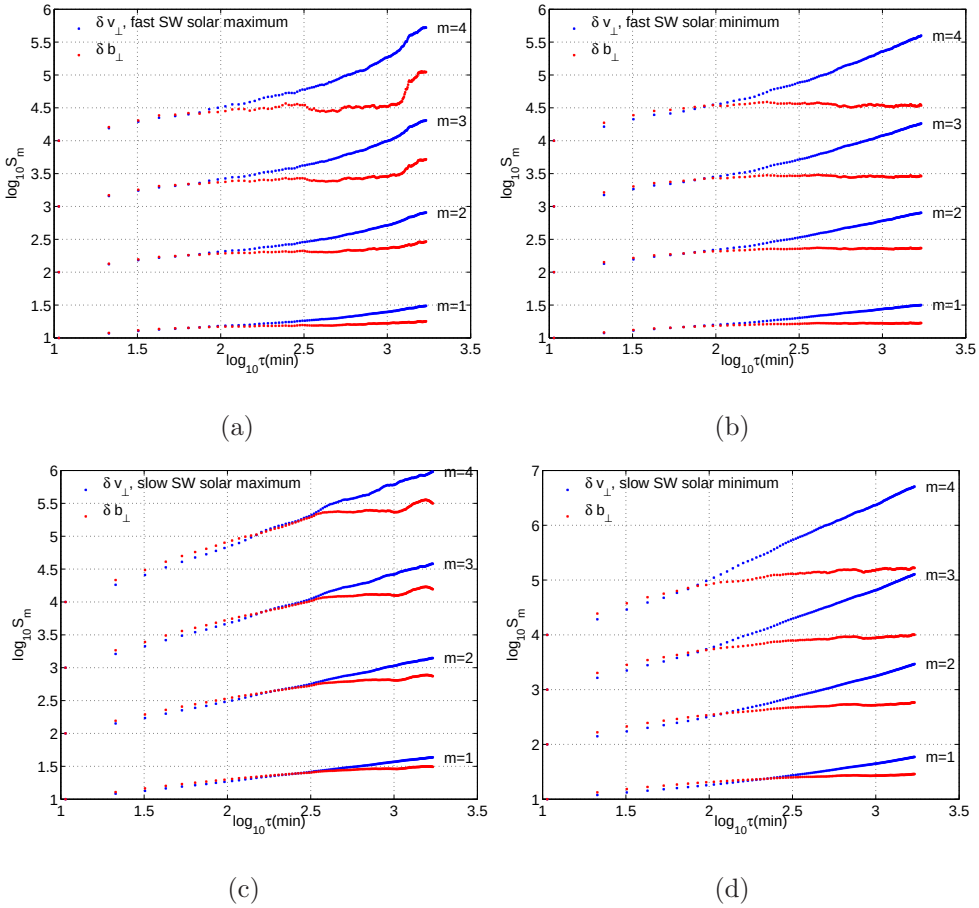

Figure 5-10: Comparison of scaling properties of perpendicular fluctuations between fast (upper) and slow (lower) solar wind at solar maximum (left) in 2000 and solar minimum (right) in 2007. Generalised structure functions S_m are plotted on log-log axes versus sampling interval τ for $\tau = 10$ to 1706 minutes and $m = 1$ to 4. Perpendicular components of fluctuations in velocity (blue) and magnetic field (red) are shown.

Figures 5-9 and 5-10 suggest that the scaling properties of $\delta v_\perp$ and $\delta b_\perp$ do not change with solar cycle in fast solar wind. However $\delta v_\parallel$ does, while the solar cycle dependence of $\delta b_\parallel$ is indeterminate. The divergences at $\tau \gtrsim 10^3$ in the fast solar wind at solar maximum may be due to finite size effects: the dataset for solar maximum is shorter than for solar minimum, because there are fewer long continuous time periods of fast solar wind. Figures 5-9 and 5-10 also show that the scaling properties of all four fluctuating quantities in the slow solar wind differ between solar maximum and minimum, due to different scaling exponents or a different breakpoint location.

Let us summarise our conclusions from the GSF analysis. First, the breakpoints

between the scaling properties measured by GSF analysis are different between fast and slow solar wind streams, and between periods of maximum and minimum solar activity. These breakpoints do not necessarily coincide with the breakpoint between IR and "$1/f$" ranges inferred from spectral analysis, however as mentioned earlier, it is difficult to extract precise quantitative information from the power spectra plots. The IR extends to longer timescales in slow solar wind streams and at periods of maximum solar activity (e.g. Horbury et al., 2005). These trends are particularly clear in the GSFs of the perpendicular components in Figure 5-10. The inertial range remains relatively robust for both slow and fast solar wind streams and is independent of solar cycle. This is to be expected if the IR is established by a turbulent cascade within the evolving expanding solar wind, rather than by initial conditions in the corona. Intriguingly, $\delta v_\perp$ and $\delta b_\perp$ have the same behaviour in the "$1/f$" range for fast solar wind at both solar maximum and minimum. Their scaling looks similar for the slow solar wind, but the breakpoint moves to longer timescales at solar maximum. All four quantities vary between fast and slow solar wind and solar minimum and maximum.

5.5 Quantifying the Scaling Exponents

Let us now quantify the observed scaling by measuring the slopes of the GSFs to obtain estimates of the values of the scaling exponents, $\zeta(m)$; the robustness of the scaling will also be tested. In principle, values for $\zeta(m)$ are obtained from the gradients of the log-log plots of S_m versus τ. In practice, these are affected by the fact that both the length of the dataset, and the range of τ over which we see scaling, are finite. The data conditioning method developped by Kiyani et al. (2006) is again used on the ACE data, in an identical fashion to the Ulysses data in chapter 3.

5.5.1 Fast Quiet Solar Wind Scaling

We now quantify the scaling exponents of $\delta v_\parallel$ and $\delta v_\perp$ fluctuations in the fast solar wind at solar minimum. The corresponding GSFs are plotted in the top right panels of Figures 5-9 and 5-10. We plot the exponents $\zeta(m)$, which are the

gradients of the fitted power laws, from $\tau = 320$ to 1002 minutes in Figure 5-11. In the lower panels we show how the value of $\zeta(2)$ changes as outliers are successively removed. Comparing with the results for fractal/multifractal processes presented in chapter 2, we infer that $\delta v_{\parallel}$ is fractal within errors and $\delta v_{\perp}$ is only very weakly multifractal (almost monofractal). For the exponents, we obtain $\zeta_{\parallel}(2)$ close to 1, suggestive of near Gaussian behaviour and (if the relation $\alpha = 1 + \zeta(2)$ holds) a PSD$\sim 1/f^2$. In contrast, the exponent for perpendicular fluctuations $\zeta_{\perp}(2)$ is close to 0.5, implying a PSD$\sim 1/f^{3/2}$.

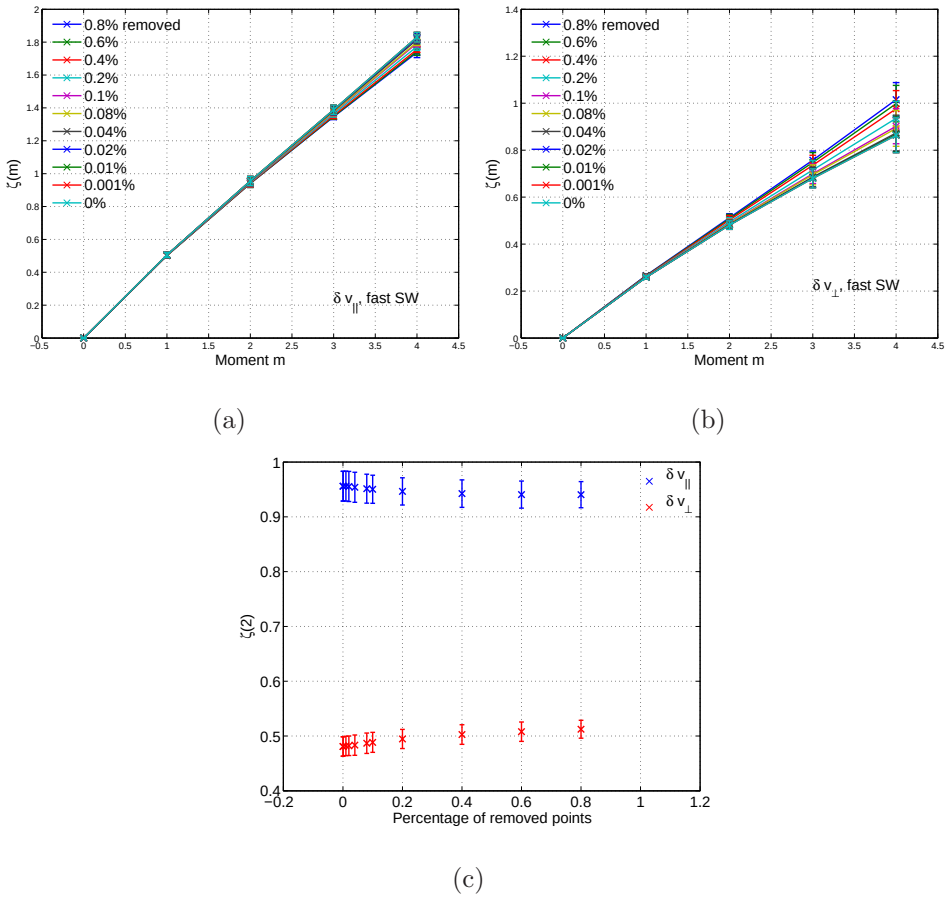

Figure 5-11: Scaling properties of fluctuations $\delta v_{\parallel}$ and $\delta v_{\perp}$ in the "$1/f$" range, $\tau = 320$ to 1002 minutes, in the fast solar wind at solar minimum. The upper panels show the $\zeta(m)$ exponents plotted as a function of moment $m = 1$ to 4 for different percentages of removed points for $\delta v_{\parallel}$ (left) and $\delta v_{\perp}$ (right). The bottom panel shows $\zeta(2)$ plotted against the percentage of removed points for $\delta v_{\parallel}$ (blue, upper) and $\delta v_{\perp}$ (red, lower).

Figure 5-12 compares the scaling exponents $\zeta(2)$ for $\delta v_{\parallel}$ and $\delta v_{\perp}$ in fast and slow solar wind streams at solar minimum. The corresponding GSFs are plotted

in the right-hand pairs of panels in Figures 5-9 and 5-10. Fluctuations of $\delta v_{\parallel}$ in the slow solar wind appear more strongly multifractal than in the fast wind. For $\delta v_{\perp}$ the slow solar wind displays a much higher exponent value for slow ($\zeta(2) \sim 0.8$) than for fast ($\zeta(2) \sim 0.5$) streams, reflecting the intrinsic differences between the fast and slow solar wind, and the coronal plasma conditions and magnetic field configuration at their origin.

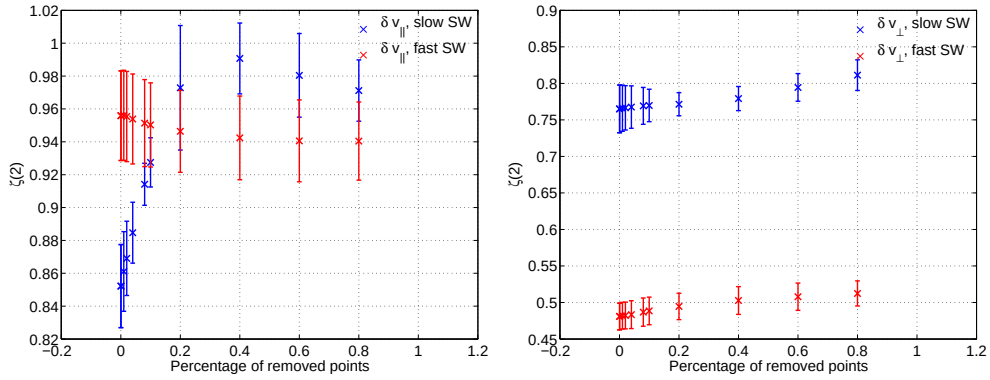

(a) (b)

Figure 5-12: Comparisons of $\zeta(2)$ at solar minimum in the "$1/f$" range as a function of the percentage of removed points for fast (red) and slow (blue) solar wind streams for $\delta v_{\parallel}$ (left) and $\delta v_{\perp}$ (right). The slow solar wind scaling appears to be more strongly multifractal.

To summarize the observed results: Analysis of the scaling exponents reveals fractal or weakly multi-fractal (very close to monofractal) scaling in the fluctuations of velocity components in the fast solar wind, with very different values for $\delta v_{\parallel}$ ($\zeta(2) \sim 0.95$) and $\delta v_{\perp}$ ($\zeta(2) \sim 0.5$) at solar minimum. In the slow solar wind at solar minimum, the scaling exponent $\zeta(2)$ of $\delta v_{\perp}$ nearly doubles from ~ 0.5 to ~ 0.8. In contrast, the scaling of $\delta v_{\parallel}$ remains quantitatively similar to its value in the fast wind (Figure 5-12), i. e. $\zeta(2) \sim 0.95$ but has a less well-defined monofractal character. Finally, if we assume a regime in which the PSD $f^{-\alpha}$ scaling exponent α is related to $\zeta(2)$ by $\alpha = 1 + \zeta(2)$, then we obtain for the fast quiet solar wind: $\alpha \sim 1$ for $\delta b_{\parallel,\perp}$ (as expected from Figure 5-1), $\alpha \sim 2$ for $\delta v_{\parallel}$ and $\alpha \sim 1.5$ for $\delta v_{\perp}$.

5.6 Conclusions

We have examined the scaling of the parallel and perpendicular velocity and magnetic field fluctuations measured in the solar wind at ~ 1 AU by ACE, which we have decomposed with respect to a locally averaged background magnetic field. Power spectra, GSFs and PDF collapse have been used to qualify and quantify the nature of the observed scaling in the low frequency "$1/f$" range. Slow and fast solar wind streams have been compared at both solar maximum in 2000 and solar minimum in 2007. The slow solar wind is found to be more multifractal and complex than the fast solar wind.

The magnetic field fluctuations display a flattening of the GSFs for $\tau \geq 178$ minutes and a spectral index ~ 1, consistent with $\sim 1/f$ behaviour found previously (Matthaeus & Goldstein, 1986; Matthaeus et al., 2007). In contrast, the velocity fluctuations show strong anisotropy, with scaling behaviour distinct from that of the **B** field and characterized by steepening of the GSFs in the "$1/f$" range (Figure 5-8) consistent with $\sim 1/f^{\alpha},\ \alpha \neq 1$.

For the fast quiet solar wind, $\delta v_{\parallel}$ and $\delta v_{\perp}$ have different scaling exponents: $\delta v_{\parallel}$ exhibits fractal scaling with $\zeta(2) \sim 0.95 \pm 0.02$ whereas $\delta v_{\perp}$ is weakly multifractal with $\zeta(2) \sim 0.49 \pm 0.03$ (Figure 5-11). The PDFs for these quantities also rescale relatively well. Also in the fast quiet solar wind, the PDF of $\delta v_{\parallel}$ is close to Gaussian, whereas $\delta b_{\parallel}$ is nearly symmetric and has stretched exponential tails, consistent with a multiplicative process. The rescaled PDFs for $\delta v_{\perp}$ and $\delta b_{\perp}$ in the fast solar wind can be fitted with the same distribution function, which is close to gamma or inverse Gumbel (see Figure 5-6). However their scaling exponents revealed by GSFs differ substantially (see Figure 5-10). We can speculate that this is consistent with a common coronal source for the fluctuations but a different spatiotemporal evolution out to 1 AU. The functional form of the PDF then constrains the mechanism that generates the fluctuations at the corona, gamma having points of contact with turbulence in confined plasmas (see for example Graves et al., 2005; Labit et al., 2007, and references therein) and Gumbel, as an extremal process.

The breakpoint between the inertial range and "$1/f$" ranges differs between fast and slow solar wind streams and between periods of maximum and minimum solar

activity. The inertial range extends to longer timescales in slow solar wind streams and at periods of maximum solar activity. The values of the inertial range scaling exponents remain unaffected by changes in the solar cycle (Figure 5-9 and Figure 5-10), consistent with locally generated turbulence.

Our results clearly show very different behaviour between the magnetic and velocity fluctuations in the "$1/f$" range. The fractal nature of $\delta v_{\parallel}$ points to distinct physical processes in the corona, and to their mapping out into the solar wind. Further work would involve relating the fractal scaling observed at $\sim$ 1AU with fractal stirring of magnetic footpoints in the corona. The different scaling observed in $\delta v_{\perp}$ points to different dynamics perpendicular to the background field (possibly field line interactions) with a possible common coronal origin of the $\delta v_{\perp}$ and $\delta b_{\perp}$ fluctuations in fast quiet solar wind.

Chapter 6

ACE RTN results

6.1 Introduction

At the large temporal/spatial scales considered in the "$1/f$" region, we are not directly concerned simply with *in situ* turbulence, rather then some other scaling signal which is a consequence of a combination of remote processes at the corona and transport convection as well as active mixing. The "natural" coordinate set is therefore far from clear. In Chapter 5, we explored the idea that the background magnetic field orders these processes (both MHD turbulent mixing and convection) and is the relevant coordinate system to quantify the anisotropy of the fluctuations. However there are other preferred directions of interest in the solar wind, such as the bulk velocity flow direction. Indeed, if one has in mind *in situ* hydrodynamic turbulence then this is the natural coordinate system. At 1 AU, the Parker spiral geometry of the interplanetary magnetic field, means that the magnetic field and the mainly radial bulk flow velocity direction are at an angle of $\sim 45^o$. As we are looking at fast solar wind flow in the solar ecliptic plane, we expect the bulk velocity flow direction to be similar to the heliospheric radial direction.

We therefore consider here the scaling behaviour of the velocity and magnetic field fluctuations in the RTN coordinate system. The PDF, GSFs and corresponding scaling exponents are computed for the fast solar wind at solar minimum (2007). The same ACE data ananlysed in Chapter 5 is used for the present work, in order to compare the 2 coordinate systems.

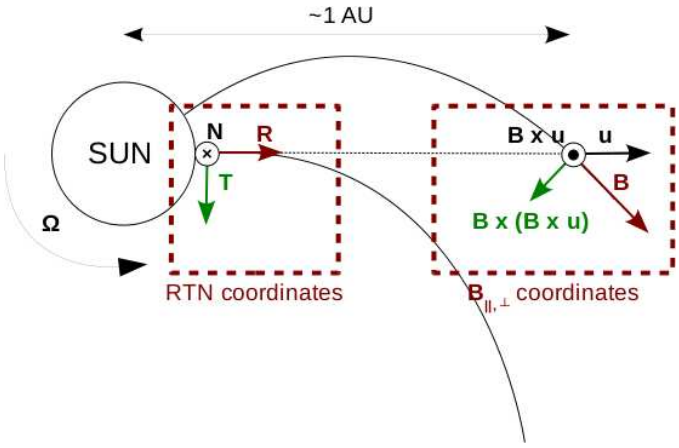

Figure 6-1: The frozen-in field lines result in the Parker spiral interplanetary magnetic field lines geometry. The R (red), T (green) and N (black) components are compared to components parallel and perpendicular to the background magnetic field with directions given by $\hat{\boldsymbol{e}}_{\parallel} = \boldsymbol{B}/|\boldsymbol{B}|$, $\hat{\boldsymbol{e}}_{\perp\mathbf{1}} = (\boldsymbol{B} \times \langle \boldsymbol{u} \rangle)/(|\boldsymbol{B} \times \langle \boldsymbol{u} \rangle|)$ and $\hat{\boldsymbol{e}}_{\perp\mathbf{2}} = (\boldsymbol{B} \times (\boldsymbol{B} \times \langle \boldsymbol{u} \rangle))/(|\boldsymbol{B} \times (\boldsymbol{B} \times \langle \boldsymbol{u} \rangle)|)$. "$\times$" indicate vectors pointing towards the page and "$\bullet$" indicate vectors pointing out of the page. Both coordinate systems are orthogonal and different colours (red, green and black) show the different components.

Figure 6-1 shows the two coordinate systems looking down on the ecliptic plane. Same colours indicate the components, which are to be compared, i.e. the radial component (red) is compared to the component parallel to the background magnetic field $\boldsymbol{B}$ (red) as these are the components in the flow direction.

6.2 PDF Analysis

Fluctuations in the velocity, $\delta v_i = v_i(t+\tau) - v_i(t)$, and magnetic field, $\delta b_i = B_i(t+\tau) - B_i(t)$, are computed for $i = R, T\&N$ in the RTN coordinate system over a range of $\tau = 320 - 1003$ minutes ($\sim 5 - 17$ hours). These are then compared to the background magnetic field aligned coordinate system of Chapter 5, we compare R to $\hat{\boldsymbol{e}}_{\parallel}$, T to $\hat{\boldsymbol{e}}_{\perp\mathbf{2}}$ and N to $\hat{\boldsymbol{e}}_{\perp\mathbf{1}}$. This comparison is chosen as following Figure 6-1, R, $\hat{\boldsymbol{e}}_{\parallel}$, T and $\hat{\boldsymbol{e}}_{\perp\mathbf{2}}$ all lie in the ecliptic plane, whereas N and $\hat{\boldsymbol{e}}_{\perp\mathbf{1}}$ lie in a plane perpendicular to the ecliptic. The PDFs are renormalised using e.g. 5-8, again if the fluctuations are from a single physical process, we expect a collapse of the PDFs onto a single characteristic function. Figure 6-2 shows the raw and normalised PDFs for $\delta v_{R,T,N}$.

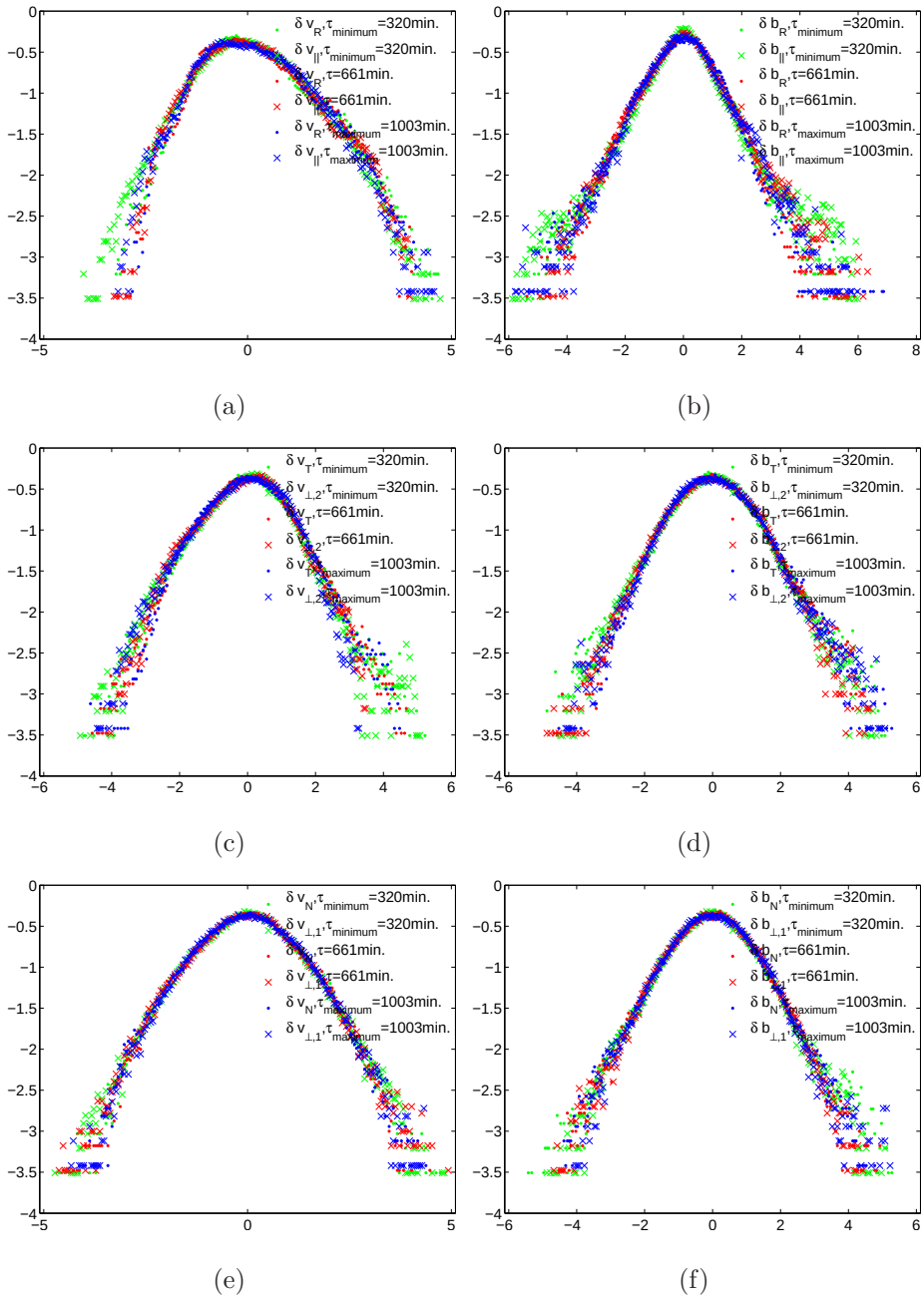

Figure 6-2: Radial (upper), tangential (middle) and normal (lower) velocity and magnetic field components' fluctuations $\delta v_{R,T,N}$ and $\delta b_{R,T,N}$ in the fast solar wind at solar minimum are compared to $\delta v_{\parallel,\perp 2,\perp 1}$ and $\delta b_{\parallel,\perp 2,\perp 1}$ for the "$1/f$" range. The fluctuations are sampled across intervals τ between 320 and 1003 minutes and the PDF curves are also normalised using equation 5-8.

Most of the renormalised PDFs collapse relatively well, however there is a large scatter in the tails and some variation between the different coordinate systems. δv_R displays a strong asymmetry and shows far more variation between the PDFs for the different τ than either δv_T or δv_N. The asymmetry is possibly indicative

of a bimodal structure, arising from the presence of distinct physical processes. It is interesting to note that this is only present in the radial component, supporting the idea that we are seeing the signature of different coronal structures carried out radially into the solar wind. δv_T and δv_N collapse well onto single curves and do not exhibit the variability seen in δv_R. The right panels of Figure 6-2 show the same analysis for $\delta b_{R,T,N}$. All the magnetic field components appear similar and collapse onto single curves. The renormalisation of the PDFs makes if difficult to distinguish between the coordinate systems as at these large scales the velocity distributions are all tending towards Gaussian shapes around their peaks. We now then consider these PDFs fitted with a Gaussian distribution, given by equation 5-9. The corresponding curves on semilog axis are shown in Figure 6-4.

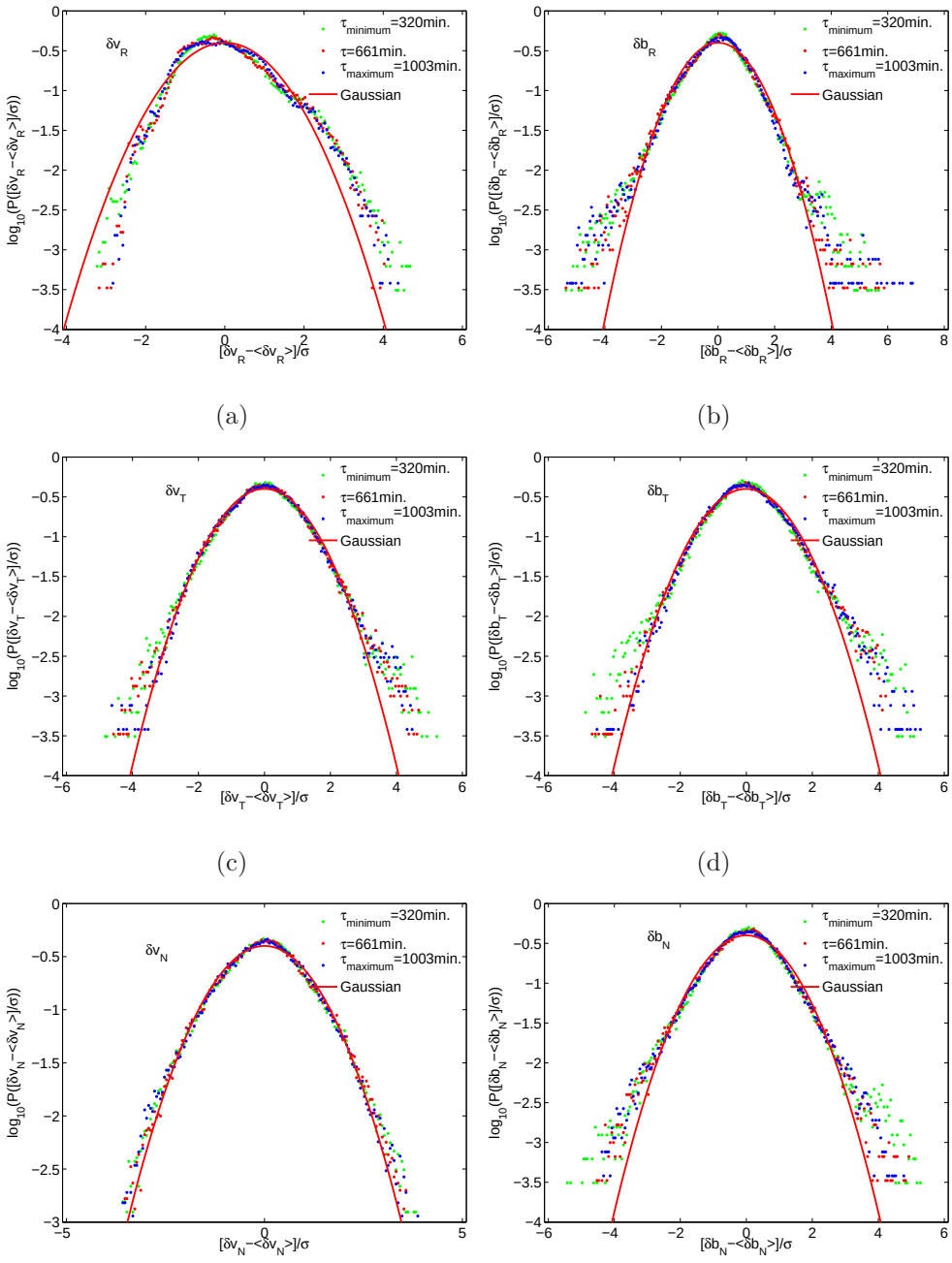

Figure 6-3: Radial, tangential and normal velocity and magnetic field components' fluctuations $\delta v_{R,T,N}$ and $\delta b_{R,T,N}$ in the fast solar wind at solar minimum for the "$1/f$" range. For clarity, plots for only three representative values of τ are shown for each component. Gaussian fits to the normalised PDF curves for both $\delta v_{R,T,N}$ (left) and $\delta b_{R,T,N}$ (right) are shown using semilog y axes.

The magnetic field fluctuations δb_R are not Gaussian and still display quite heavy tails, with a lot of scatter. This is consistent with previous results such as (Padhye et al., 2001) for example, who found slight departures from Gaussianity

for magnetic field fluctuations decomposed with respect to the background field and (Burlaga & F.-Viñas, 2004), who use ACE magnetic field magnitude flucutations over scales from 1 hour to 171 days to demonstrate their non-Gaussian nature. The magnetic field fluctuations $\delta b_{T,N}$ and the velocity field fluctuations δv_T are similar to Gaussian in their peak regions, however the PDF tails still display heavy tails. Again Burlaga & F.-Viñas (2004) observed that the velocity magnitude tended to a Gaussian distribution at larger τ scales ($> 2^4$ hours or 960 minutes).

In summary, we see that δv_R and δb_R are distinct as their PDFs rescale differently. This is similar to our result from Chapter 5, where we showed that $\delta v_\parallel$ and $\delta b_\parallel$ were distinct. We also note that $\delta v_\parallel$ and δv_R are different, with $\delta v_\parallel$ showing a reduced asymmetry and a closer fit to Gaussian than δv_R. In contrast, $\delta b_\parallel$ and δb_R both exhibit non-Gaussian PDFs with stretched exponential tails. The behaviour normal to the ecliptic plane is the same. However, the plane containing $\boldsymbol{B}$ and $\boldsymbol{v}$ is less clear, with mixing components remaining an open question. In order to further investigate any scaling differences, we turn to GSF analysis.

6.3 GSF Comparison

As in the previous Chapters, we perform GSF analysis on the two different coordinate systems for both velocity and magnetic field and compare the corresponding curves.

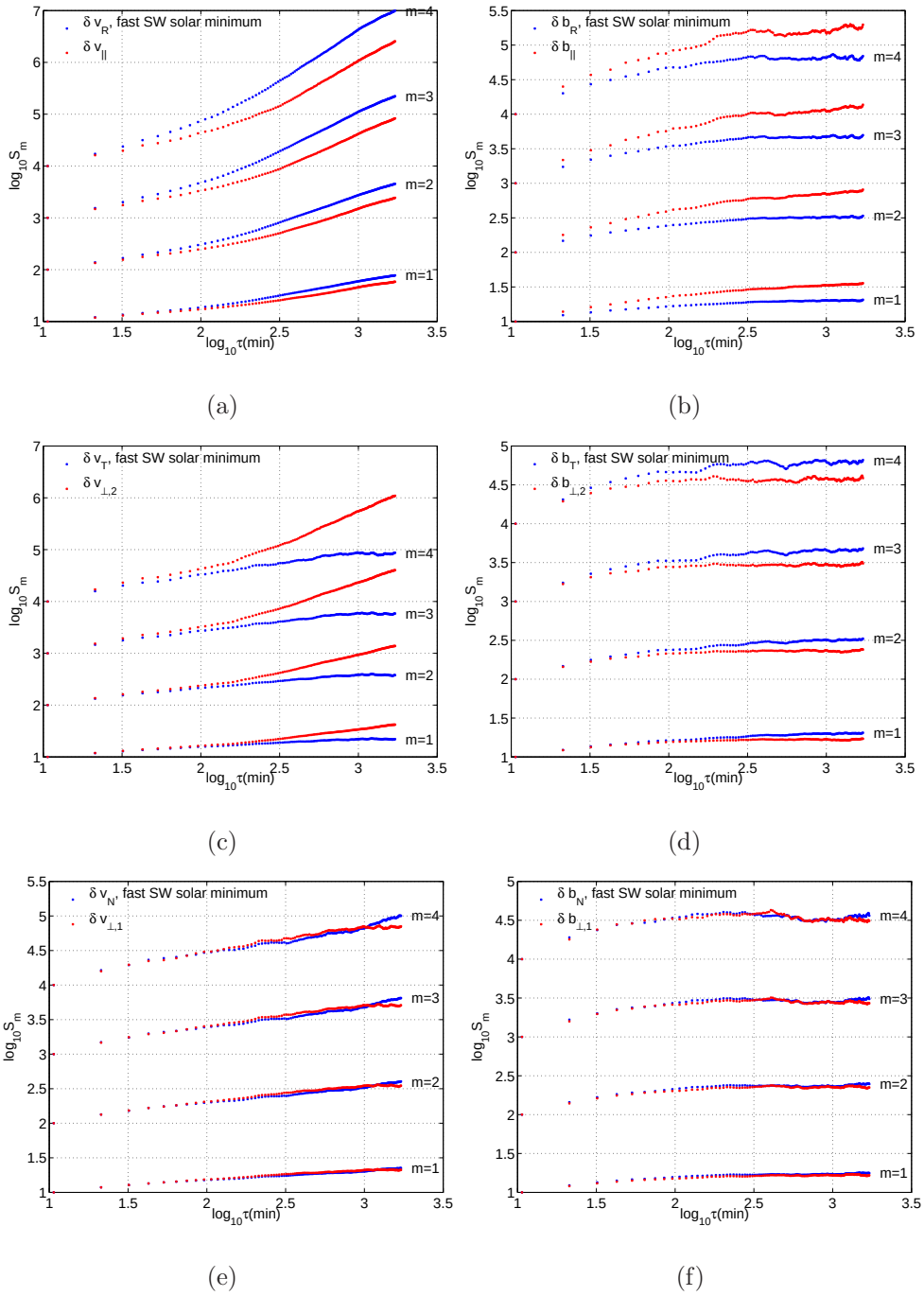

Figure 6-4: Comparison of scaling properties of fluctuations in RTN coordinates (blue) and $\boldsymbol{B}$ aligned coordinates (red) in the fast solar wind at solar minimum in 2007 for velocity (left) and magnetic field (right) fluctuations. The generalised structure functions S_m are plotted on log-log axes versus sampling interval τ for $\tau = 10$ to 1706 minutes and $m = 1$ to 4. Only the 0.4% conditioned data is shown for clarity.

Figure 6-4 shows that the inertial range scaling is different between the two coordinate systems and components except for N and $\hat{\boldsymbol{e}}_{\perp\mathbf{2}}$, consistent with the

anisotropic nature of the inertial range. The large scale magnetic field still shows a characteristic flattening in both reference frames. We can also note the N and $\hat{\boldsymbol{e}}_{\perp\mathbf{2}}$ fluctuations overlay in a near identical way, consistent with our picture in Figure 6-1 that these components both lie normal to the ecliptic plane. T has a behaviour similar to the magnetic field at large scales and $\hat{\boldsymbol{e}}_{\perp\mathbf{1}}$ has a behaviour closer to the radial velocity field scaling. this is consistent with the fact that T is approximately normal to the bulk velocity flow but therefore there is some mixing with the parallel and perpendicular components and similarly $\hat{\boldsymbol{e}}_{\perp\mathbf{1}}$ is normal to the magnetic field but there is some mixing with the radial and tangential components. Indeed it is between the velocity fluctuations in T and $\hat{\boldsymbol{e}}_{\perp\mathbf{1}}$ that the strongest difference is observed. Also $\hat{\boldsymbol{e}}_{\perp\mathbf{1}}$ and $\hat{\boldsymbol{e}}_{\perp\mathbf{2}}$ velocity fluctuations have a different scaling, in Chapter 5 the scaling we observe is then a mix of perpendicular fluctuations. However we argue that the difference between parallel and perpendicular fluctuations is still real and the averaging over the perpendicular components does not affect this result or the PDF analysis of Chapter 5. Rather, it tells us that these fluctuations have a common source but evolved differently depending on whether they were in the ecliptic plane or normal to it. To quantify the scaling in the "$1/f$" range, we use linear regression fits over $\tau = 320$ to 1002 minutes to extract the $\zeta(m)$ scaling exponents. In Figure 6-5, we plot $\zeta(2)$ as a function of the percentage of removed points.

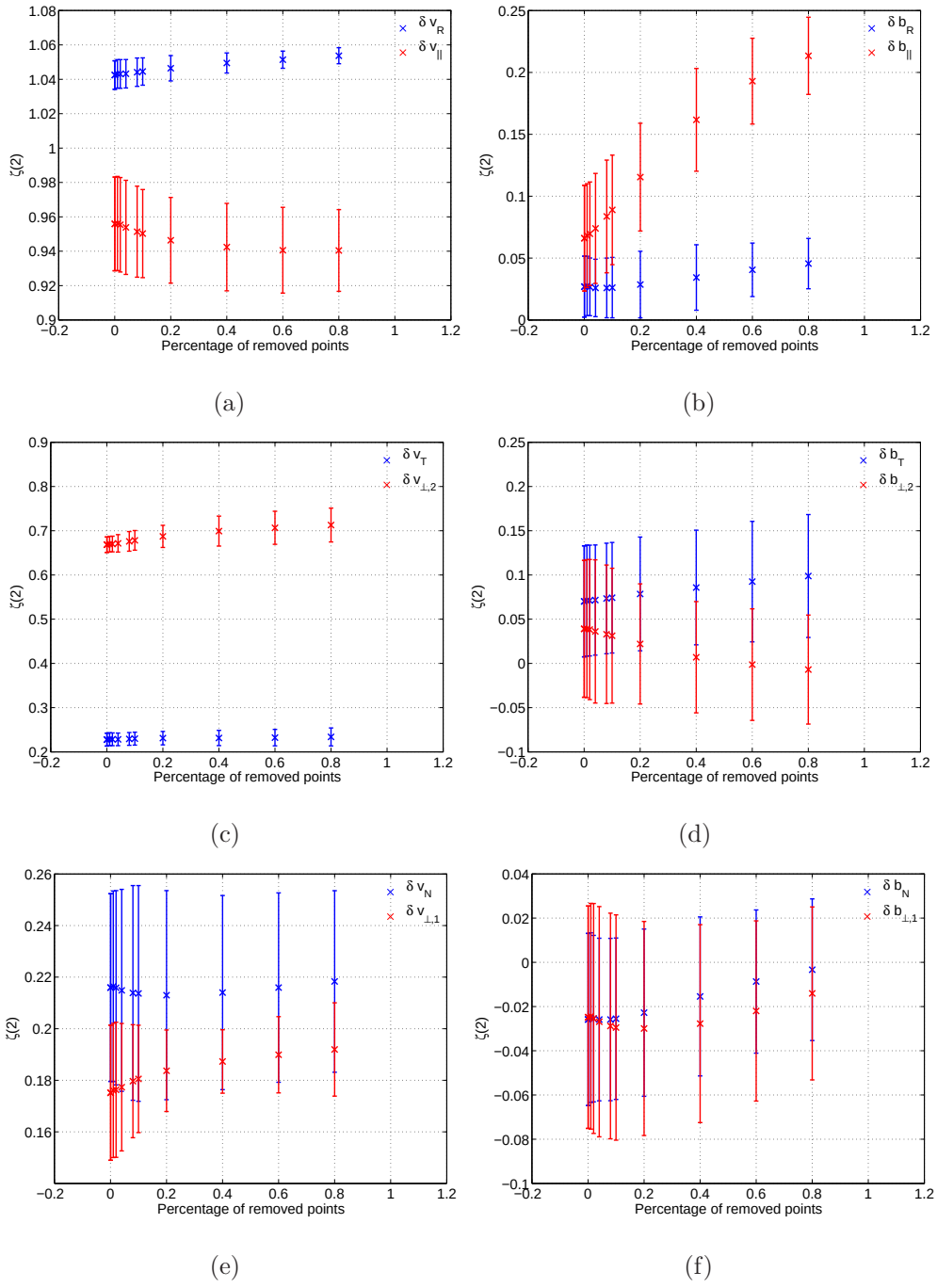

Figure 6-5: The $\zeta(2)$ exponents extracted from the linear fits to $\tau = 320$ to 1002 minutes for different percentages of removed points are shown for the RTN coordinates (blue) and the $\hat{\boldsymbol{e}}_{\parallel,\perp\mathbf{2},\perp\mathbf{1}}$ coordinates (red) for the fast solar wind at solar minimum (2007).

Figure 6-5 confirms that that the N and $\hat{\boldsymbol{e}}_{\perp\mathbf{1}}$ components are the same within errors with $\zeta(2) \sim 0.20 \pm 0.05$ for the velocity fluctations and ~ 0 for the the magnetic field fluctuations, these results are consistent with the observed flattening

of the GSFs. Generally, the $\zeta(2)$ exponents for the magnetic field show little variation between the two coordinate sets and have consistently small values with $\zeta(2) \sim [0 - 0.2] \pm 0.05$. In contrast for the velocity fluctuations. R and $\hat{\boldsymbol{e}}_{\parallel}$ are distinct with $\zeta(2)_R \sim 1.05 \pm 0.01$ and $\zeta(2)_{\parallel} \sim 0.95 \pm 0.02$. However, as observed previously, the strongest variation is between the velocity T and $\hat{\boldsymbol{e}}_{\perp \mathbf{2}}$ components, where $\zeta(2)_T \sim 0.23 \pm 0.02$ (similar to the magnetic field scaling) and $\zeta(2)_{\perp 2} \sim 0.7 \pm 0.04$ (closer to the radial velocity scaling).

Finally, we show in Figure 6-6 the compensated third order structure function S_3/τ against τ on a semilog axis, the plots are in no way shifted for comparison as in Figure 6-5. This is the same process as used in Figure 4-1 and although we are no longer just considering the inertial range here, this plot nevertheless provides a useful comparison of the power levels between the different components.

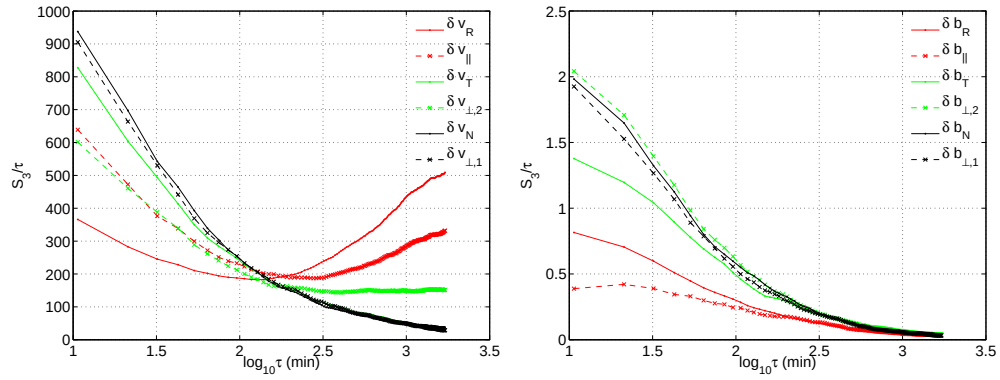

(a) (b)

Figure 6-6: S_3/τ against τ on semilog axis for $\tau = 10$ to 1706 minutes for the velocity (left panel) and magnetic field (right panel) for the fast solar wind at solar minimum (2007). The breakpoint between the inertial range and the "$1/f$" region is clearly visible in the velocity plot at $\tau \sim 10^{2.25}$ minutes or about 3 hours.

Again this plot is another clear indicator of the spectral breakpoint between the inertial range and the "$1/f$" region, which occurs at $\tau \sim 10^{2.25}$ minutes or about 3 hours. After the breakpoint, the velocity field fluctuations seem to diverge, in contrast to the magnetic field fluctuations. We still observe the near-identical behaviour of the N and $\hat{\boldsymbol{e}}_{\perp \mathbf{1}}$ components for both velocity and magnetic field. We also observe that the velocity components in both coordinate systems still preserve a strong anisotropy between the parallel and perpendicular components

and the radial and the tangential and normal components. This is consistent with our observations in Chapter 5, where we found $\delta v_{\parallel}$ and $\delta v_{\perp}$ to have very different scaling.

6.4 Conclusions

We have compared the scaling of velocity and magnetic field fluctuations in the fast ecliptic solar wind in two different frames of reference: the RTN coordinate system, where R is radial from the Sun and assumed to be approximately aligned with the bulk velocity flow direction and a coordinate system decomposed into parallel and perpendicular components with respect to the local background magnetic field.

The PDF analysis revealed the radial velocity fluctuations to be more strongly asymmetric than the parallel velocity fluctuations. The T and N fluctuations are close to Gaussian, however the magnetic field T and N components and the velocity T component still have quite strong scatter in the PDF tails. In order to quantify any differences, we need to use GSFs.

We find that the magnetic field and velocity field flucutations are distinct from each other in the "$1/f$" region. This is most apparent in the radial/parallel components shown in the top panels of 6-4.

In the "$1/f^{\alpha}$" region, the characteristic flattening of the GSFs (consistent with a power spectral exponent α close to 1) is again observed for all magnetic field components and both coordinate sets. The scaling exponents are similar for $\delta b_{\perp 1,\perp 2}$ and $\delta b_{T,N}$ (Figure 6-5), the strongest difference is between the radial and parallel components.

Both coordinate systems have a component in the plane normal to the ecliptic, N and $\hat{\boldsymbol{e}}_{\perp \mathbf{2}}$, and these also scale in an identical way for velocity and magnetic field. The other components all lie in the ecliptic plane and are affected by the different preferred directions present of the background magnetic field curved in the Parker spiral, and the heliocentric radial expansion. The radial and parallel velocity fluctuations' components are distinct but nevertheless have relatively close values, consistent with scaling dominated by the outwards expansion of the solar wind.

The tangential component, also in the ecliptic plane, shows scaling similar to the magnetic field, whereas the $\hat{\boldsymbol{e}}_{\perp\mathbf{2}}$ component (normal to the background field) has scaling closer to the radial velocity fluctuations.

The anisotropy between the parallel and perpendicular velocity field components (Figure 6-6) is also observable between the radial and the normal and tangential components. Whether the radial velocity component fluctuations are a result of parallel and perpendicular flucutations mixing or vice-versa is still an open question. It is then difficult to say which coordinate system is preferable, as both carry signatures of the preferred directions present. The S_3/τ plots also clearly show the differences between velocity and magnetic field scaling, in particular in the "$1/f^{\alpha}$" region.

Chapter 7

Conclusions

7.1 Thesis summary

7.1.1 Ulysses

We have examined a range of temporal scales in polar and ecliptic solar wind for different solar conditions such as fast/slow solar wind and periods of different solar activity.

We first considered Ulysses polar magnetic field measurements in the RTN coordinate system as we were looking at small scale fluctuations (temporal scales of 1 to 15 minutes) on open field lines emanating from the polar coronal holes. We analysed ten day intervals over which time the timeseries could be considered stationary and the variation in Ulysses radial and heliographic position is small. First the north polar pass of 1995 is examined using power spectra (Figure 3-1), generalised structure functions (Figures 3-2, 3-3 and 3-4) and extended self-similarity (Figures 3-6, 3-8 and 3-9). These methods were previously tested in Chapter 2 on model timeseries (Brownian walk, Lévy Flight and multifractal p-model).

We conclude that the inertial range (energy cascade) of fast quiet polar solar wind does not show straight-forward power law behaviour, rather it can be fitted by the same function $g(\tau)$ (Figure 3-12) for all components. The $g(\tau)$ function was observed not to have any radial or latitudinal dependence over the ranges considered. An initial fit of quadratic form was estimated for $g(\tau)$, however this had little physical significance and proved problematic in the limit of small τ.

The analysis was further extended to include all Ulysses solar minima magnetic field measurements for the South passes of 1994 and 2007 and the North pass of 2008. The most recent solar minima is particularly interesting, as the Sun was observed to be much quieter, with much lower density and magnetic field strength

measurements. We find a decrease in the power output between the two successive minima by almost a factor of two (Figure 4-2). Our analysis however showed that the statistical properties of the magnetic field fluctuations in the inertial range were identical for all passes.

We further refined our $g(\tau)$ function by fitting a simpler function $g(\tau/\tau_0)^{\zeta(3)} = a(\tau/\hat{\tau})^{\tau/\tau_0{}^b}$, $\zeta(3) \sim 1$, which now incorporates a normalisation scale of $\hat{\tau} = 1$ minute and the approximate outer scale of the inertial range $\tau_0 = 10$ minutes. The fitting parameters $a = 0.101 \pm 0.001$ and $b = 0.10 \pm 0.01$ show good agreement with the experimental data (Figure 4-6). We now extend this fitting to find the scaling exponents $\zeta(m)$. The $\zeta(m)$ are found to be well fitted by a p-model with $\zeta(3) = 1$ (Figure 4-9).

We have demonstrated the importance of finite-size effects on the scaling in the inertial range of solar wind turbulence. We have then shown that although the solar wind is a spatially extended system, the finite Reynolds number and large scale structures can affect the scaling, especially for higher order moments. To our knowledge, this is the first observation of this effect in the solar wind. Further work would involve investigating the presence of $g(\tau/\tau_0)$ in other turbulent systems. This would give more insight into the possible universal nature of this function in inertial range turbulence.

7.1.2 ACE

ACE measurements provide an unique opportunity to study solar wind fluctuations at 1 AU in the solar ecliptic plane. We analysed magnetic field and velocity fluctuations in a frame orientated with respect to the background magnetic field. At 1 AU the Parker spiral means that magnetic field lines are twisted due to the solar rotation and can not be thought of as radial. We choose a magnetic field aligned coordinate system, however there are also other preferred directions present in the solar wind, such the bulk flow direction, and we also consider this in Chapter 6.

Chapter 5 focuses on the large scale fluctuations in the so called "$1/f$" temporal range of the solar wind. This region is characterised by the a "$1/f^{\alpha}$" magnetic field power spectra with $\alpha \sim 1$ (Figure 5-1).

We consider periods of high and low solar activity and fast and slow solar wind streams separately. Our observations show $\alpha \sim 1$ in our magnetic field aligned coordinate system for the magnetic field fluctuations however a very different behaviour is observed in the velocity field. The velocity field GSFs show a strong steepening (Figure 5-8), also reflected in the power spectra. The velocity parallel and perpendicular components are also different, with different scaling exponents, $\zeta(2)_{\parallel} \sim 0.95 \pm 0.02$ whereas $\zeta(2)_{\perp} \sim 0.49 \pm 0.03$ (Figure 5-11). This is evidence of strong anisotropy at these scales.

In the fast solar wind at solar minimum, PDF analysis reveals the parallel velocity fluctuations to be close to Gaussian (Figure 5-5, top panels), whereas $\delta b_{\parallel}$ is closer to a multiplicative process, with stretched exponential tails (Figure 5-5, bottom panels). The rescaled PDFs for $\delta v_{\perp}$ and $\delta b_{\perp}$ in the fast solar wind can be fitted with the same inverse Gumbel (or gamma) distribution function (Figure 5-6, which is an extremal process. GSF analysis however shows that their scaling exponents differ substantially. We hypothesis that this is evidence of a common coronal source for the fluctuations but a different spatiotemporal evolution out to 1 AU.

Our analysis also unexpectedly reveals an extremely sensitive indicator of the breakpoint between the inertial range of turbulence and the "$1/f$" energy containing scales. Upon comparing the GSFs of the magnetic field and velocity fluctuations, a clear divergence in behaviour beyond the spectral breakpoint is observed (Figures 5-8, 5-9 and 5-10).

The inertial range scaling remains similar between the $\delta b_{\parallel,\perp}$ and $\delta v_{\parallel,\perp}$ fluctuations and has no dependence on solar cycle, which is what we would expect for *in situ* generated turbulence. The value of the scaling exponents in the inertial range do vary between fast and slow streams by approximately a factor of 2 higher in the slow solar wind. This is again due to the different level of turbulent evolution between the fast and slow solar wind. We would expect the slow solar wind to be more evolved than the fast streams. The longest inertial range observed extended to $\tau \sim 300$ minutes (Figure 5-10), in the slow solar wind during solar maximum and the shortest inertial range was ~ 100 minutes for the fast solar wind at solar minimum. Again this is consistent with the more highly evolved state of the slow

solar wind.

Finally in Figure 7-1, we summarise the behaviour of $\zeta(2)$ scaling exponent for the fast and slow velocity solar wind streams at periods of maximum (2000) and minimum (2007) solar activity.

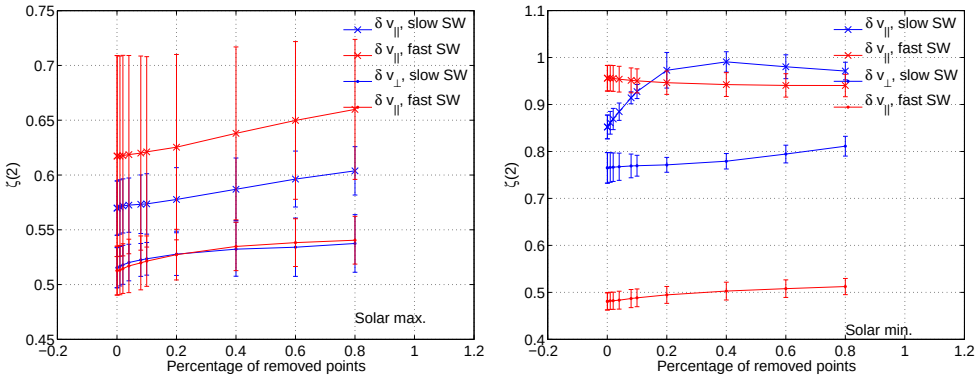

(a) (b)

Figure 7-1: Comparisons of $\zeta(2)$ at solar maximum (left panel) minimum (right panel) in the "$1/f$" range as a function of the percentage of removed points for fast (red) and slow (blue) solar wind streams for $\delta v_{\parallel}$ ("$\times$") and $\delta v_{\perp}$ ("$\cdot$").

Firstly, Figure 7-1 shows that at solar maximum all the components are similiar (within errors) between fast and slow and there is only a very weak anisotropy between the parallel and perpendicular components. If we think of a simple idealised picture of the solar wind, with a highly complex topological magnetic field at solar maximum, with reconnection events, flares, and highly twisted magnetic field lines then this similarity between all the components is consistent with all the components being "mixed in", or almost isotropic. In both slow and fast streams, these are the dominant processes, which govern the scaling. We are therefore seeing a mixture of transport and source, which we cannot untangle.

At solar minimum, the first thing to note is that the scaling is different between parallel and perpendicular components and also is very different in the parallel direction from the solar maximum. Our simple picture here of the solar wind is that there are no complicated structures affecting the flow or large transient coronal structures. We are therefore seeing the direct signature of the coronal organisation carried out into the expanding solar wind and which has not been lost by interaction with other structures. The different scaling behaviour between fast

and slow, both in the fractal/multifractal nature of $\delta v_{\parallel}$ and the different values of $\zeta(2)$ for $\delta v_{\perp}$ point to the different mechanisms at the origin of the two different types of wind.

The fractal nature of $\delta v_{\parallel}$ points to distinct physical processes in the corona, and to their mapping out into the solar wind. This scaling could then be mapped back to the fractal scaling of the "magnetic carpet" known to exist in the solar corona. In Chapter 6, we compare the RTN coordinate system with a system decomposed into parallel and perpendicular fluctuations with respect to the background magnetic field. We find that our assumption of isotropy in the perpendicular plane for the velocity fluctuations does not hold for the GSF scaling exponents (Figures 6-5 and 6-6), eventhough we showed in Chapter 5 that the fluctuations in $\hat{\boldsymbol{e}}_{\perp\mathbf{2},\perp\mathbf{1}}$ have the same functional form. Again this points to a common origin but different evolution. However the result from Chapter 5, namely that there is a distinct anisotropy in the fast solar wind between parallel and perpendicular velocity fluctuations still holds. This is also apparent between the R and the T and N components (Figures 6-5 and 6-6). It is then possible to argue that the RTN coordinate sytem is a better system in which to study velocity fluctuations, whereas the background magnetic field aligned coordinates are more suited to a study of the magnetic field fluctuations. However, if we wish to compare the scaling of these fluctuations we need the same coordinate system for both.

All of these results show that generic timeseries analysis tools such as structure functions and PDFs can be used to extract information over a wide range of scales and conditions in the solar wind. We have shown the effect of finite Reynolds number on inertial range scaling and we have probed the solar cycle and solar wind speed dependence of velocity and magnetic field fluctuations. The results point to different mechanisms behind the origin of these streams and the topological solar differences between periods of maximum and minimum solar activity.

References

Acheson, D. J. 1990, Elementary Fluid Dynamics (Oxford University Press)

Arenas, A. & Chorin, A. J. 2006, Proceedings of the National Academy of Science, 103, 4352

Aschwanden, M. J., Stern, R. A., & Güdel, M. 2008, ApJ, 672, 659

Babcock, H. W. 1961, ApJ, 133, 572

Bak, P., Tang, C., & Wiesenfeld, K. 1987, Physical Review Letters, 59, 381

Balogh, A., Beek, T. J., Forsyth, R. J., Hedgecock, P. C., Marquedant, R. J., Smith, E. J., Southwood, D. J., & Tsurutani, B. T. 1992, Astron. Astrophys. Suppl. Ser., 92, 221

Barnes, A. 1992, Reviews of Geophysics, 30, 43

Baumjohann, W. & Treumann, R. A. 1996, Basic space plasma physics, ed. R. A. Baumjohann, W. Treumann

Bavassano, B., Bruno, R., & D'Amicis, R. 2005, Annales Geophysicae, 23, 1025

Belcher, J. W. 1971, ApJ, 168, 509

Benz, A., ed. 2002, Astrophysics and Space Science Library, Vol. 279, Plasma Astrophysics, second edition

Benzi, R., Ciliberto, S., Tripiccione, R., Baudet, C., Massaioli, F., & Succi, S. 1993, Phys. Rev. E, 48, 29

Biskamp, D. 1993, Nonlinear magnetohydrodynamics, ed. D. Biskamp

Biskamp, D. & Müller, W.-C. 2000, Physics of Plasmas, 7, 4889

Bohr, T., Jensen, M. H., Paladin, G., & Vulpiani, A. 1998, Dynamical Systems Approach to Turbulence, ed. T. Bohr, M. H. Jensen, G. Paladin, & A. Vulpiani

Boldyrev, S. 2005, ApJ Lett., 626, L37

—. 2006, Physical Review Letters, 96, 115002

Borgani, S., Murante, G., Provenzale, A., & Valdarnini, R. 1993, Phys. Rev. E, 47, 3879

Borgas, M. S. 1992, Physics of Fluids, 4, 2055

Bruno, R. & Carbone, V. 2005, Living Reviews in Solar Physics, 2, 4

Bruno, R., Carbone, V., Chapman, S., Hnat, B., Noullez, A., & Sorriso-Valvo, L. 2007, Physics of Plasmas, 14, 032901

Bruno, R., Carbone, V., Sorriso-Valvo, L., & Bavassano, B. 2003, Journal of Geophysical Research (Space Physics), 108, 1130

Budaev, V. P., Takamura, S., Ohno, N., & Masuzaki, S. 2006, Nuclear Fusion, 46, 181

Burlaga, L. F. 1991, J. Geophys. Res., 96, 5847

Burlaga, L. F. & F.-Viñas, A. 2004, Journal of Geophysical Research (Space Physics), 109, 12107

Burlaga, L. F. & Forman, M. A. 2002, J. Geophys. Res., 107, 1403

Burlaga, L. F. & Klein, L. W. 1986, J. Geophys. Res., 91, 347

Burlaga, L. F., Mish, W. H., & Roberts, D. A. 1989, J. Geophys. Res., 94, 177

Carbone, V., Marino, R., Sorriso-Valvo, L., Noullez, A., & Bruno, R. 2009, Phys. Rev. Lett., 103, 061102

Carrington, R. C. 1858, Monthly Notices of the Royal Astronomical Society, 19, 1

—. 1859, Monthly Notices of the Royal Astronomical Society, 20, 13

Chapman, S. C. & Hnat, B. 2007, Geophys. Res. Lett., 34, 17103

Chapman, S. C., Hnat, B., Rowlands, G., & Watkins, N. W. 2005a, Nonlinear Processes

in Geophysics, 12, 767

Chapman, S. C., Nicol, R. M., Leonardis, E., Kiyani, K., & Carbone, V. 2009a, ApJ Lett., 695, L185

Chapman, S. C., Rowlands, G., & Watkins, N. W. 2005b, Journal of Physics A Mathematical General, 38, 2289

—. 2009b, Physics of Plasmas, 16, 012303

Charbonneau, P. 2005, Living Reviews in Solar Physics, 2, 2

Cox, A. N. 2000, Allen's astrophysical quantities, ed. A. N. Cox

Cravens, T. E., ed. 1997, Physics of solar system plasmas /Thomas E. Cravens. Cambridge : Cambridge

Dendy, R. O. & Chapman, S. C. 2006, Plasma Physics and Controlled Fusion, 48, B313

Dewhurst, J. M., Hnat, B., Ohno, N., Dendy, R. O., Masuzaki, S., Morisaki, T., & Komori, A. 2008, Plasma Physics and Controlled Fusion, 50, 095013

Dudson, B. D., Dendy, R. O., Kirk, A., Meyer, H., & Counsell, G. F. 2005, Plasma Physics and Controlled Fusion, 47, 885

Einstein, A. 1905, Annalen der Physik, vol. 322, Issue 8, pp.549-560, 322, 549

Feynman, J., Ruzmaikin, A., & Smith, E. J. 1995, in Solar Wind Conference, 80–+

Forsyth, R. J., Balogh, A., Horbury, T. S., Erdoes, G., Smith, E. J., & Burton, M. E. 1996, Astron. Astrophys, 316, 287

Frisch, U. 1991, Royal Society of London Proceedings Series A, 434, 89

—. 1995, Turbulence. The legacy of A.N. Kolmogorov, ed. U. Frisch

Frisch, U. & Sornette, D. 1997, Journal de Physique I, 7, 1155

Gagne, Y., Castaing, B., Baudet, C., & Malécot, Y. 2004, Physics of Fluids, 16, 482

Galtier, S. 2008, Phys. Rev. E, 77, 015302

—. 2009, ApJ, 704, 1371

Galtier, S., Nazarenko, S. V., Newell, A. C., & Pouquet, A. 2000, Journal of Plasma Physics, 63, 447

Goldreich, P. & Sridhar, S. 1995, ApJ, 438, 763

Goldstein, B. E., Smith, E. J., Balogh, A., Horbury, T. S., Goldstein, M. L., & Roberts, D. A. 1995a, Geophys. Res. Lett., 22, 3393

Goldstein, M. L. 2001, Astrophysics and Space Science, 277, 349

Goldstein, M. L., Roberts, D. A., & Matthaeus, W. H. 1995b, ARA&A, 33, 283

Gosling, J. T., Asbridge, J. R., Bame, S. J., Feldman, W. C., Borrini, G., & Hansen, R. T. 1981, J. Geophys. Res., 86, 5438

Graves, J. P., Dendy, R. O., Hopcraft, K. I., & Jakeman, E. 2002, Physics of Plasmas, 9, 1596

Graves, J. P., Horacek, J., Pitts, R. A., & Hopcraft, K. I. 2005, Plasma Physics and Controlled Fusion, 47, L1

Greenhough, J., Birch, P. C., Chapman, S. C., & Rowlands, G. 2002a, Physica A Statistical Mechanics and its Applications, 316, 615

Greenhough, J., Chapman, S. C., Chaty, S., Dendy, R. O., & Rowlands, G. 2002b, A&A, 385, 693

Grossmann, S., Lohse, D., L'vov, V., & Procaccia, I. 1994, Phys. Rev. Lett., 73, 432

Grossmann, S., Lohse, D., & Reeh, A. 1997, Phys. Rev. E, 56, 5473

Habbal, S. R., Woo, R., Fineschi, S., O'Neal, R., Kohl, J., Noci, G., & Korendyke, C. 1997, ApJ Lett., 489, L103+

Hale, G. E. 1908, ApJ, 28, 315

Hale, G. E., Ellerman, F., Nicholson, S. B., & Joy, A. H. 1919, ApJ, 49, 153

Hapgood, M. A. 1992, P&SS, 40, 711

Hnat, B., Chapman, S. C., & Rowlands, G. 2005, Journal of Geophysical Research (Space Physics), 110, 8206

Hnat, B., Chapman, S. C., Rowlands, G., Watkins, N. W., & Freeman, M. P. 2003, Geophys. Res. lett, 30, 220000

Hnat, B., Dudson, B. D., Dendy, R. O., Counsell, G. F., Kirk, A., & the MAST team. 2008, Nuclear Fusion, 48, 085009

Hoeksema, J. T. 1995, Space Science Reviews, 72, 137

Horbury, T., Balogh, A., Forsyth, R. J., & Smith, E. J. 1995a, Annales Geophysicae, 13, 105

Horbury, T. S. & Balogh, A. 1997, Nonlinear Processes in Geophysics, 4, 185

—. 2001, J. Geophys. Res., 106, 15929

Horbury, T. S., Balogh, A., Forsyth, R. J., & Smith, E. J. 1995b, Geophys. Res. Lett., 22, 3401

—. 1996a, J. Geophys. Res., 101, 405

—. 1996b, Astron. Astrophys., 316, 333

Horbury, T. S., Forman, M., & Oughton, S. 2008, Physical Review Letters, 101, 175005

Horbury, T. S., Forman, M. A., & Oughton, S. 2005, Plasma Physics and Controlled Fusion, 47, B703

Howard, R. A., Sheeley, Jr., N. R., Michels, D. J., & Koomen, M. J. 1985, J. Geophys. Res., 90, 8173

Hurst, H. E., Black, R. P., & Simaika, Y. M. 1965, Long-term storage: an experimental study (Constable, London)

Iroshnikov, P. S. 1964, Soviet Astronomy, 7, 566

Issautier, K., Le Chat, G., Meyer-Vernet, N., Moncuquet, M., Hoang, S., MacDowall, R. J., & McComas, D. J. 2008, Geophys. Res. Lett., 35, 19101

Kiyani, K., Chapman, S. C., & Hnat, B. 2006, Phys. Rev. E, 74, 051122

Kiyani, K., Chapman, S. C., Hnat, B., & Nicol, R. M. 2007, Physical Review Letters, 98, 211101

Kolmogorov, A. N. 1991a, Royal Society of London Proceedings Series A, 434, 15

—. 1991b, Royal Society of London Proceedings Series A, 434, 9

Kraichnan, R. H. 1965, Physics of Fluids, 8, 1385

Krieger, A. S., Timothy, A. F., & Roelof, E. C. 1973, Solar Physics, 29, 505

Labit, B., Furno, I., Fasoli, A., Diallo, A., Müller, S. H., Plyushchev, G., Podestà, M., & Poli, F. M. 2007, Physical Review Letters, 98, 255002

Landau, L. D. & Lifshitz, E. M. 1987, Fluid mechanics, 2nd edn. (Permagon)

Lang, K. R. 1999, Astrophysical formulae, ed. K. R. Lang

Lang, K. R., ed. 2000, The sun from space

Longair, M. S. 2003, Theoretical Concepts in Physics, ed. M. S. Longair

Lynch, S. 2007, Dynamical systems with applications using mathematica, ed. B. Boston

MacQueen, R. M., Eddy, J. A., Gosling, J. T., Hildner, E., Munro, R. H., Newkirk, Jr., G. A., Poland, A. I., & Ross, C. L. 1974, ApJ Lett., 187, L85+

Mandelbrot, B. B. 1982, The Fractal Geometry of Nature, ed. B. B. Mandelbrot

Marsch, E. & Tu, C.-Y. 1990, J. Geophys. Res., 95, 11945

—. 1996, J. Geophys. Res., 101, 11149

—. 1997, Nonlinear Processes in Geophysics, 4, 101

Marsden, R. G., Smith, E. J., Cooper, J. F., & Tranquille, C. 1996, Astron. Astrophys., 316, 279

Mason, J., Cattaneo, F., & Boldyrev, S. 2008, Phys. Rev. E, 77, 036403

Matthaeus, W. H., Breech, B., Dmitruk, P., Bemporad, A., Poletto, G., Velli, M., &

Romoli, M. 2007, ApJ Lett., 657, L121

Matthaeus, W. H., Dasso, S., Weygand, J. M., Milano, L. J., Smith, C. W., & Kivelson, M. G. 2005, Physical Review Letters, 95, 231101

Matthaeus, W. H. & Goldstein, M. L. 1982, J. Geophys. Res., 87, 10347

—. 1986, Physical Review Letters, 57, 495

Matthaeus, W. H., Goldstein, M. L., & Roberts, D. A. 1990, J. Geophys. Res., 95, 20673

McComas, D. J., Bame, S. J., Barker, P., Feldman, W. C., Phillips, J. L., Riley, P., & Griffee, J. W. 1998a, Space Science Reviews, 86, 563

McComas, D. J., Bame, S. J., Barraclough, B. L., Feldman, W. C., Funsten, H. O., Gosling, J. T., Riley, P., Skoug, R., Balogh, A., Forsyth, R., Goldstein, B. E., & Neugebauer, M. 1998b, Geophys. Res. Lett., 25, 1

McComas, D. J., Barraclough, B. L., Funsten, H. O., Gosling, J. T., Santiago-Muñoz, E., Skoug, R. M., Goldstein, B. E., Neugebauer, M., Riley, P., & Balogh, A. 2000, J. Geophys. Res., 105, 10419

McComas, D. J., Ebert, R. W., Elliott, H. A., Goldstein, B. E., Gosling, J. T., Schwadron, N. A., & Skoug, R. M. 2008, Geophys. Res. Lett., 35, 18103

McComas, D. J., Elliott, H. A., Gosling, J. T., & Skoug, R. M. 2006, Geophys. Res. Lett., 33, 9102

Meadows, A. J. 1970, Early solar physics, ed. A. J. Meadows

Meneveau, C. & Sreenivasan, K. R. 1987, Physical Review Letters, 59, 1424

Mercadier, N., Guerin, W., Chevrollier, M., & Kaiser, R. 2009, Nature Physics, 5, 602

Merrifield, J. A., Arber, T. D., Chapman, S. C., & Dendy, R. O. 2006, Physics of Plasmas, 13, 012305

Merrifield, J. A., Chapman, S. C., & Dendy, R. O. 2007, Physics of Plasmas, 14, 2301

Merrifield, J. A., Müller, W.-C., Chapman, S. C., & Dendy, R. O. 2005, Physics of Plasmas, 12, 022301

Monin, A. S. & Yaglom, A. M. 1971, Statistical Fluid Mechanics, ed. J. L. Lumley (The MIT Press), oringinally published in 1965 by Nauka Press, Moscow, under the title *Statisicheskaya gidromekhanika - Mekhanika Turbulentnosti*. Translated from the Russian by Scripta Technica, Inc.

Mullan, D. J. & Smith, C. W. 2006, Solar Physics, 234, 325

NASA. 2009, `http://solarscience.msfc.nasa.gov/images/bfly.gif`

Neugebauer, M., Gloeckler, G., Gosling, J. T., Rees, A., Skoug, R., Goldstein, B. E., Armstrong, T. P., Combi, M. R., Mäkinen, T., McComas, D. J., von Steiger, R., Zurbuchen, T. H., Smith, E. J., Geiss, J., & Lanzerotti, L. J. 2007, ApJ, 667, 1262

Neugebauer, M. & Snyder, C. W. 1962, Science, 138, 1095

Ng, C. S. & Bhattacharjee, A. 1997, Physics of Plasmas, 4, 605

Nicol, R. M., Chapman, S. C., & Dendy, R. O. 2008, ApJ, 679, 862

—. 2009, ApJ, 703, 2138

Ofman, L. 2005, Space Science Reviews, 120, 67

Osman, K. T. & Horbury, T. S. 2009, Journal of Geophysical Research (Space Physics), 114, 6103

Oughton, S., Priest, E. R., & Matthaeus, W. H. 1994, Journal of Fluid Mechanics, 280, 95

Padhye, N. S., Smith, C. W., & Matthaeus, W. H. 2001, J. Geophys. Res., 106, 18635

Pagel, C. & Balogh, A. 2001, Nonlinear Processes in Geophysics, 8, 313

Paladin, G. & Vulpiani, A. 1987, Phys. Reports, 156, 147

Parker, E. N. 1958, ApJ, 128, 664

Percival, D. B. & Walden, A. T. 1993, Spectral Analysis for Physical Applications:

Multitaper and Conventional Univariate Techniques

Phillips, J. L., Balogh, A., Bame, S. J., Goldstein, B. E., Gosling, J. T., Hoeksema, J. T., McComas, D. J., Neugebauer, M., Sheeley, Jr., N. R., & Wang, Y.-M. 1994, Geophys. Res. Lett., 21, 1105

Phillips, J. L., Bame, S. J., Feldman, W. C., Goldstein, B. E., Gosling, J. T., Hammond, C. M., McComas, D. J., Neugebauer, M., Scime, E. E., & Suess, S. T. 1995, Science, 268, 1030

Politano, H. & Pouquet, A. 1995, Phys. Rev. E, 52, 636

—. 1998a, Geophys. Res. Lett., 25, 273

—. 1998b, Phys. Rev. E, 57, 21

Politano, H., Pouquet, A., & Carbone, V. 1998, Europhysics Letters, 43, 516

Priest, E. R. 1985, Solar system magnetic fields. Based on lectures presented at the Summer School on Solar System Plasmas, held at Imperial College, London, September 1984., ed. E. R. Priest

Priest, E. R., Foley, C. R., Heyvaerts, J., Arber, T. D., Mackay, D., Culhane, J. L., & Acton, L. W. 2000, ApJ, 539, 1002

Reidy, W. P., Vaiana, G. S., Zehnpfennig, T., & Giacconi, R. 1968, ApJ, 151, 333

Ruzmaikin, A., Goldstein, B. E., Smith, E. J., & Balogh, A. 1995a, in Solar Wind Eight, 38–+

Ruzmaikin, A., Lyannaya, I. P., Styashkin, V. A., & Eroshenko, E. 1993, J. Geophys. Res., 98, 13303

Ruzmaikin, A. A., Feynman, J., Goldstein, B. E., Smith, E. J., & Balogh, A. 1995b, J. Geophys. Res., 100, 3395

Sahraoui, F., Goldstein, M. L., Robert, P., & Khotyaintsev, Y. V. 2009, Physical Review Letters, 102, 231102

Sánchez Granero, M. A., Trinidad Segovia, J. E., & García Pérez, J. 2008, Physica A: Statistical Mechanics and its Applications, 287, 5543

Schrijver, C. J., Zwaan, C., Balke, A. C., Tarbell, T. D., & Lawrence, J. K. 1992, A&A, 253, L1

Seuront, L., Schmitt, F., Lagadeuc, Y., Schertzer, D., & Lovejoy, S. 1999, Journal of Plankton Research, 21, 877

She, Z.-S. & Leveque, E. 1994, Physical Review Letters, 72, 336

Shebalin, J. V., Matthaeus, W. H., & Montgomery, D. 1983, Journal of Plasma Physics, 29, 525

Siegert, S. & Friedrich, R. 2001, Phys. Rev. E, 64, 041107

Smith, C. W., L'Heureux, J., Ness, N. F., Acuña, M. H., Burlaga, L. F., & Scheifele, J. 1998, Space Science Reviews, 86, 613

Smith, E. J. & Balogh, A. 1995, Geophys. Res. Lett., 22, 3317

—. 2008, Geophys. Res. Lett., 35, 22103

Smith, E. J., Balogh, A., Neugebauer, M., & McComas, D. 1995, Geophys. Res. Lett., 22, 3381

Sornette, D. 2004, Critical phenomena in natural sciences : chaos, fractals selforganization and disorder : concepts and tools, ed. D. Sornette

Sorriso-Valvo, L., Carbone, V., & Bruno, R. 2004, Europhysics Letters, 67, 504

Sorriso-Valvo, L., Marino, R., Carbone, V., Lepreti, F., Veltri, P., Noullez, A., Bruno, R., Bavassano, B., & Pietropaolo, E. 2007, ArXiv Astrophysics e-prints, 99, 115001

Sreenivasan, K. R. & Bershadskii, A. 2006, Journal of Fluid Mechanics, 554, 477

Sridhar, S. & Goldreich, P. 1994, ApJ, 432, 612

Stephenson, F. R. 1990, Royal Society of London Philosophical Transactions Series A,

330, 499

Stern, D. P. 1989, Reviews of Geophysics, 27, 103

Stone, E. C., Frandsen, A. M., Mewaldt, R. A., Christian, E. R., Margolies, D., Ormes, J. F., & Snow, F. 1998, Space Science Reviews, 86, 1

Tarbell, T., Ferguson, S., Frank, Z., Shine, R., Title, A., Topka, K., & Scharmer, G. 1990, in IAU Symposium, Vol. 138, Solar Photosphere: Structure, Convection, and Magnetic Fields, ed. J. O. Stenflo, 147–+

Taylor, G. I. 1938, Royal Society of London Proceedings Series A, 164, 476

Tu, A.-Y., Marsch, E., & Rosenbauer, H. 1996, Annales Geophysicae, 14, 270

Vaiana, G. S., Krieger, A. S., & Timothy, A. F. 1973, Solar Physics, 32, 81

Wadsworth, H. M. 1998, Handbook of statistical methods for engineers and scientists, ed. J. Wadsworth, H. M. (McGraw-Hill)

Wolfgang, P. & Baschnagel, J. 1999, Stochastic processes from physics to finance, ed. S.-V. B. Heidelberg